博士論文

Numerical Modeling of Combustion Instability in Hybrid Rocket Motors

（ハイブリッドロケットモーターの燃焼不安定性の数値モデリング）

カルティィケヤン　ゴウタム

(Karthikeyan Goutham)

Abstract

Hybrid rocket propulsion is hailed as one of the candidates for the next generation chemical propulsion system that can cater to the increasing necessity for reliable, regular, safe and cost-effective access to space. However, one of the long-chronicled problems in hybrid rockets is the presence of intrinsic low frequency combustion instability. These combustion instabilities can cause unplanned thrust fluctuations that can result in a launch failure of the rocket. Before this problem can be eliminated, it needs to be studied carefully with an understanding of the underlying physical processes that result in the unstable behaviour of the motor. Existing models to study this phenomenon are restricted in their capabilities to only prediction of linear characteristics such as frequency of oscillations. They cannot predict the non-linear effects such as the limit cycle amplitude which are seen in all experimental results. They also cannot predict if or not whether a motor would be susceptible to instability. Therefore, the aim of this thesis is to model this phenomenon using a numerical model. The numerical model is designed not only to study this phenomenon of combustion instability, but also to be able to be used by a potential hybrid rocket motor designer to design engines that are not susceptible to this phenomenon.

In this thesis, it is shown the steady state heat-feedback from the flame to the burning fuel surface can be modelled as a function of the boundary layer properties by using the Reynold's analogy. A power law function form for the determination of ratio of skin coefficient frictions with and without blowing is assumed during this derivation. A novel method to model the unsteady heat-feedback from flame is proposed by the consideration of finite time delay for the wall heat flux to adapt to changes to the regression rate through the blowing effect. Using an analogous analytical modelling, it has been shown that the presence of such a delayed feedback can result in an unstable system due to the occurrence of negative damping. It has also been shown that depending on the magnitude of this boundary layer delay, which is the finite delay experienced by the convective heat flux to the changes in the mass flux and the regression rate in the boundary layer, different non-linear behaviour can be extracted. An attempt is also made in this regard to model the oscillatory regression rate equation in hybrids and the limitations of such an approach have been elucidated.

The computational model that has been developed for the simulation of the transient internal ballistics in the rocket motor consists of the following four sub models: 1) a quasi-one-dimensional gas dynamics model using Euler equations for flowfield simulation, 2) a chemical model using CEA, 3) an analytical heat-feedback model for transfer of heat from the flame to the burning solid fuel surface, 4) a one-dimensional thermal conduction model inside the solid fuel. All these sub-models have been individually constructed, verified and coupled together. The numerical model has been validated against experimental data for the prediction of steady state regression rates.

In the unsteady time-dependent simulation, it is seen that upon the consideration of the proposed unsteady heat-feedback, at first an oscillating periodic increase in the regression rate and chamber pressure is observed, which then proceeds into a non-linear limit cycle. A positive DC shift in the chamber pressure is also observed. It is seen that all the natural modes of the system are excited. The FFT of the pressure oscillations show that frequencies of different natural modes (including the intrinsic hybrid oscillation mode) predicted by the model are found to be in good agreement with theoretical prediction. The frequencies of the regression rate oscillations also show the same peaks as that of the pressure oscillations showing that there is a coupling between the acoustics and the unsteady burning in the combustion chamber of the motor.

Parametric analyses have been carried out by varying the boundary layer delay values. It is seen that both the RMS amplitude and the magnitude of the DC shift of the limit cycle region asymptotically increases with increasing boundary layer delay in a logarithmic fashion. However, there exists a minimum delay value for the system below which, the system is always stable. This observation is important because it suggests that any mechanism that can alter the boundary layer delay values can alter the intrinsic stability characteristics of the system. As a natural corollary, it is seen that with increasing port diameter, the unsteady characteristics increases, which in turn may be attributed to the average boundary layer delay increase.

The limitation of using a power law functional form for the ratio of skin coefficient frictions in the derivation of the unsteady convective heat flux is explained using a sensitivity analysis. As an improvement, an analytical model utilizing a logarithmic functional form is adopted in the derivation of the unsteady heat-feedback from the flame. Using this model, experimental comparisons for the prediction of limit cycle pressure amplitude were performed against two sets of experimental data. It is seen that the numerical results match well with the experiments.

The novelty of this numerical modelling approach is that by using the proposed unsteady convective heat flux, the normal unsteady characteristics of the combustion as seen in experiments such as limit cycle amplitudes can be obtained. Also, the details about all the natural modes of the system can be extracted without the necessity of any external forcing. Therefore, the numerical model serves as a powerful tool to model and study the unsteady combustion in hybrid rocket motors. Within its limitations of Q1D flow field, the model additionally serves as an excellent engineering tool for a motor designer to parametrically study the effect of different motor configurations on the motor stability characteristics.

Acknowledgements

Completion of this thesis and my doctoral degree would have been impossible if not for the collective support and guidance of many individuals. Here, I would try to acknowledge a few of them.

First and foremost, I would like to express my deepest of gratitude to my advisor, Prof. Toru Shimada who accepted me under his tutelage and guided me with his great knowledge, experience and patience for 5 years. It has truly been a pleasure and as well as a privilege to be a member of his research group.

I would also like to express my indebtedness to all the members of the laboratory both current and past, not only for guiding me in my research, but also for making my life as a research student more enjoyable. I would also like to thank fellow hybrid rocket research members, both in Japan and abroad for all the discussions and constructive criticisms towards my research.

This acknowledgement would not be complete if I do not thank my friend, Ms. Ankita Jain, without whom my life in Japan would be incomplete. I would also like to thank the numerous other friends and acquaintances who have enriched my life these past years in various ways. Last, but certainly not the least, I would like to express my gratitude to my beloved parents, and my lovely sister, for they continue to be the support behind all my accomplishments.

I would also like to express my gratitude to the Global Leader Program for Social Design and Management of The University of Tokyo and the Japan Society for the Promotion of Science for the provision of research grants during the doctoral program.

Table of Contents

Abstract ………………………………………………………………… i

Acknowledgements …………………………………………………….... iii

Table of Contents ……………………………………………………... iv

List of Figures ………………………………………………………… vii

List of Tables ……………………………………………………...... x

Nomenclature……………………………………………………………. xi

Chapter – 1 Introduction ………………………………………………. 1

1.1 The Hybrid Rocket ……………………………………………… 2

1.2 Advantages and Disadvantages ………………………………………. 3

1.3 Boundary Layer Combustion ………………………………………… 5

1.4 Combustion Instability ……………………………………………….. 7

1.5 Structure of the Thesis ……………………………………………... 9

1.6 References for Chapter 1 ……………………………………………... 11

Chapter –2 Literature Review ……………………………………………. 12

2.1 Survey of Existing Research …………………………………………….. 13

2.2 Aim of the Study ………………………………………………………... 17

2.3 References for Chapter 2 ……………………………………………... 18

Chapter – 3 Modeling Hybrid Rocket Combustion Instability …………… 20

3.1 Modeling Hybrid Rocket Boundary Layer Combustion ………………….. 21

3.2 Boundary Layer Delay ……………………………………………….. 26

3.3 Self-Excited Oscillations ……………………………………………... 28

3.4 Analogy with a Generalized Non-Linear Oscillating System ……………... 30

3.5 Derivation of Oscillatory Regression Rate Equation ……………………... 32

3.6 Conclusion ………………………………………………………... 36

3.7 References for Chapter 3 ……………………………………………... 37

Chapter –4 Numerical Modeling of Internal Ballistics …………………….. 38
4.1 Introduction to the Numerical Modeling ………………………………. 39
4.2 Gas Dynamics Model ………………………………………………... 40
  4.2.1 Governing Equations ……………………………………………. 41
  4.2.2 Gas Dynamics Model Domain Definition ………………………... 43
  4.2.3 Boundary Conditions ……………………………………………. 44
  4.2.4 Numerical Solution ……………………………………………… 45
  4.2.5 Evaluation of Discretized Flux ………………………………….... 46
  4.2.6 Higher Order Spatial Accuracy ………………………………….... 49
  4.2.7 Higher Order Temporal Accuracy ……………………………….. 52
  4.2.8 Energy Balance Equation ………………………………………... 53
  4.2.9 Quasi-Steady State Approximation ………………………………. 55
  4.2.10 Convergence of the Steady State Solution ……………………….. 55
4.3 Heat-Feedback Model ……………………………………………….... 57
  4.3.1 Evaluation of Convective Heat Transfer …………………………... 57
4.4 Combustion Model – Chemical Equilibrium Model …………………... 59
  4.4.1 Chemical Equilibrium Calculation ……………………………….. 59
  4.4.2 Chemical Composition in the Quasi 1-Dimensional Flow Field ……... 60
  4.4.3 Chemical Composition in the Flame Region ……………………... 61
4.5 Thermal Conduction Model ………………………………………….... 62
  4.5.2 Domain Definition ………………………………………………. 63
  4.5.3 Boundary Conditions ……………………………………………. 63
  4.5.4 Numerical Solution ……………………………………………… 64
  4.5.5 Pyrolysis of the Fuel …………………………………………….... 64
4.6 Model Integration …………………………………………………… 67
  4.6.1 Coupling of the sub-systems …………………………………….... 67
  4.6.2 Marching till Burn Time …………………………………………. 67
  4.6.3 Averaging Method for Regression Rate ………………………….... 69
4.7 References for Chapter 4 …………………………………………….... 70

Chapter –5 Computational Analysis of Hybrid Rocket Internal Ballistics ... 71

5.1 Results of Steady State Characteristics ………………………………….... 72

  5.1.1 Prediction of Internal Ballistics …………………………………….... 72

  5.1.2 Grid Dependency Results ………………………………………….... 75

  5.1.3 Validation of the Numerical Model ………………………………….. 76

5.2 Results of Transient Characteristics …………………………………….... 78

  5.2.1 Transient Behavior of the Thermal Oscillator ……………………….... 79

  5.2.2 Perturbation Analysis ………………………………………………. 81

  5.2.3 Modeling Boundary Layer Delay ………………………………….... 83

  5.2.4 Results obtained on Modeling Boundary Layer Delay ……….... 85

  5.2.5 Spatial Variation Effects ……………………………………… 90

5.3 Parametric Analysis ……………………………………………….... 94

  5.3.1 Effect of Boundary Layer Delay ……………………………..… 94

    5.3.1.1 Effect on the Frequency of Oscillations …………………… 94

    5.3.1.2 Effect on the Non-Linear Behaviour ……………………… 96

  5.3.2 Effect of Port Diameter ……………………………………… 98

  5.3.3 Effect of Power Exponent in Blowing Functional Form ……….. 99

5.4 Comparison with Experimental Results …………………………… 102

5.5 Conclusions …………………………………………………… 106

5.6 References for Chapter 5 ……………………………………… 108

Chapter – 6 Conclusion ……………………………………………. 109

6.1 Conclusion of the Thesis ……………………………………… 110

6.2 Future Extension of Work …………………………………….. 112

List of Figures

Fig. 1.1 Classical hybrid rocket schematic ……………………………... 2

Fig. 1.2 Historical and projected commercial orbital launches …………... 3

Fig. 1.3 Hybrid rocket in operation during the flight of VSS Unity……… 4

Fig. 1.4 Processes in Turbulent Boundary Layer Combustion …………... 6

Fig. 1.5 Pressure-time trace for a GOX/paraffin-based hybrid motor …… 8

Fig. 1.6 FFT plot of a pressure time trace of a typical paraffin-based motor 9

Fig. 2.1 High frequency chamber pressure versus time – Test 1……..…… 13

Fig. 2.2 Regions of regression rate dependency ……………………...… 15

Fig. 3.1 Effect of blowing parameter on ratio of skin-coefficient friction .. 24

Fig. 3.2 Variation of ratio of coefficient of skin friction based on different functional forms of blowing parameter ………………………... 25

Fig. 3.3 Delayed dependence of heat feedback on regression rate……… 28

Fig. 3.4 Simple damped oscillating system …………………………….. 29

Fig. 3.5a Presence of a limit cycle; *t = 0.1* ……………………...……... 30

Fig. 3.5b Increase in value of amplitude; *t= 0.4* …………………………... 31

Fig. 3.5c Finite DC Shift, *t = 1* …………………………………………… 31

Fig. 3.5d Non-linear frequency shift, *t = 10* ……………….…………… 31

Fig. 3.6 Energy balance at the regressing fuel surface …………………... 32

Fig. 3.7 Oscillatory regression with no thermal delay ………..………… 36

Fig. 4.1 Schematic of the HR combustion chamber ………...………... 40

Fig. 4.2 Domain for Gas-Dynamics Model …………………..………… 43

Fig. 4.3 Piece-wise linear MUSCL reconstruction of data ……...……. 49

Fig. 4.4 Schematic of the thermal conduction ……………..…………… 62

Fig. 4.5 Relationship between sub-models ……………...…………… 67

Fig. 4.6 Time marching flowchart ……………………………………… 68

Fig. 5.1a Steady state – pressure profile ………………………………….. 74

Fig. 5.1b Steady state – velocity profile …………………………….…... 75

Fig. 5.1c Steady state – density profile …………………………………… 75

Fig. 5.1d Steady state – temperature profile ……………………………… 75

Fig. 5.1e Steady state – mixture fraction profile ………………………..…….. 75

Fig. 5.1f Steady state – regression rate profile ………………………..……. 75

Fig. 5.2 Spatial regression rate at the end of different burns …………… 76

Fig. 5.3 Grid convergence calculation result – Test 1 …………………… 76

Fig. 5.4 Temporally averaged oxidizer mass flux vs. spatially and temporally averaged regression rate ……………………………. 77

Fig. 5.5 Overshooting of the thermal oscillator during instantaneous throttling ……………………………..…………………... 80

Fig. 5.6 Temporal solution with initial velocity perturbation …..………. 83

Fig. 5.7 Boundary layer delay along port length ………..………………. 85

Fig. 5.8a Linear region to non-linear transition …………………………... 86

Fig. 5.8b Temporal variation of non-dimensional pressure ………………. 87

Fig. 5.9 Temporal variation of non-dimensional regression rate ………... 88

Fig. 5.10 FFT of pressure oscillations …………………………..…….. 89

Fig. 5.11 FFT of regression rate oscillations ……………………………... 89

Fig. 5.12 Spatial variation of pressure at different times …………………. 91

Fig. 5.13 Spatial variation of non-dimensionalized pressure amplitude ….. 91

Fig. 5.14 Time varying non-dimensional pressure amplitude at 3 different axial locations …………………….………………………… 92

Fig. 5.15 Spatial variation in FFT of pressure oscillations ……..……… 93

Fig. 5.15 Spatial variation in FFT of regression rate oscillations ………... 93

Fig. 5.17a FFT of pressure oscillations for $\tau_{bl=2T}$ ………………..………... 95

Fig. 5.17b FFT of pressure oscillations for $\tau_{bl=2.5T}$ ……………………..…. 95

Fig. 5.17c FFT of pressure oscillations for $\tau_{bl=3T}$ ………………………….. 96

Fig. 5.18a Dependence of RMS pressure amplitude on boundary layer delay …………………………………………………..….. 97

Fig. 5.18b Dependence of DC shift on boundary layer delay ……………… 98

Fig. 5.19 Effect of port diameter on the non-dimensionalized pressure amplitude ……………………………………………………. 99

Fig. 5.20 C_f/C_{f0} dependence on blowing power exponent, *k* ……………… 100

Fig. 5.21 Effect of pressure *k* on the derivative of heat-flux ……………… 101

Fig. 5.22 Effect of parameter *k* on the non-linear characteristics ………… 101
Fig. 5.23 Experimental result of test 11R ………………………………… 104
Fig. 5.24 Numerical result for test 11R …………………………………... 104
Fig. 5.25 Experimental result of test 9R ………………………………….. 105
Fig. 5.26 Numerical result of test 9R ……………………………………... 106

List of Tables

Table 4.1 Subsonic inflow condition ………………………………………... 44

Table 4.2 Parameters in Arrhenius type equation and solid fuel enthalpy equation ………………………………………………………. 66

Table 5.1 Experimental conditions for steady state validation …………...… 72

Table 5.2 Physical properties of HDPE ……………………………………... 73

Table 5.3 List of natural frequency prediction for different modes present … 90

Table 5.4 Numerical prediction of frequency of primary hybrid oscillation mode ………………………………………………………. 96

Table 5.5 Experimental conditions for validation of unsteady analysis ……. 103

Table 5.6 Physical properties of HTPB ……………………………………... 103

Nomenclature

A = cross sectional area
A_c = pre-exponential factor
Bt = thermochemical blowing parameter
C_f = wall-friction coefficient
D = primary parameter which is perturbed
E_a = activation energy
F = flux vector
G = total flux
G_{ox} = oxidizer mass flux
K_{ox} = oxidizer concentration
LM = lagrange multiplier
L_p = port length
N_c = number of cells in the flowfield grid
N_F = number of cells in the solid fuel
O/F = oxidizer-to-fuel ratio
P_c = chamber pressure
Q = conserved vector
Q_c = heat flux input
R = radius of the cross-section of the fuel grain
R_e = residual of specific total energy
R_p = residual of pressure
R_t = residual of temperature
R_u = universal gas constant
S_{MASS} = mass addition source term
S_{Q1D} = quasi 1-dimensional flowfield source term
T = temperature
Y_i = mass fraction of chemical species, i
a = parameter in eqn. 3.5.15
amp = percentage amplitude of perturbation

b_i = mole number of atomic elements, i per unit mass of mixture gas
c = speed of sound
$c_{p,\,i}$ = specific heat of chemical species, i at constant pressure
e = specific internal energy
$e_{reaction}$ = fuel degradation zone thickness
e_t = specific total energy
h_F = heat of formation
h_i = specific enthalpy of species i
h_v = effective heat of gasification of the solid fuel
h_w = specific enthalpy of the fuel gas evaporating from the surface of the solid fuel
k = constant used in eqn. 3.3.1
L_p = perimeter of cross-section of the fuel grain
$\dot{m}_F$ = mass addition from the surface of the solid fuel
$\dot{m}_{ox}$ = oxidizer mass flow rate
n = constant used in eqn. 3.5.15
p = pressure
q = constant used in eqn. 3.3.1
$\dot{r}$ = solid fuel regression rate
t = time
t_b = total burn time of the motor
u = velocity
w = cell variable
x = axial location as measured from the port-head
y = location as measured normal to the regressing fuel surface
z = axial location as measured from port end
Δh_i^0 = standard enthalpy of formation of chemical species, i
Δx = space interval
Δt = time interval
α = thermal diffusivity
ε = mixture fraction

λ = thermal conductivity
μ = viscosity
π = ratio of circumference to diameter of a circle
ρ = density
ω = angular frequency

Subscripts
1 = fuel stream
2 = oxidizer stream
avg = spatial and temporal averaged value
bl = boundary layer
C = combustion chamber
e = free stream value
f = fuel
final = final state
fl = flame location
initial = initial state
o = steady state value
ox = oxidizer
s = solid fuel
sr = regressing surface
T = throat
wall = outer wall of the solid fuel
z = axial location as measured from port end

Superscripts
avg = spatial and temporal averaged value
L = left hand extrapolated boundary variable
R = right hand extrapolated boundary variable
t = transpose

Abbreviations and Acronyms

AUSM = Advective Upstream Splitting Method

CEA = Chemical Equilibrium with Applications

CFD = Computational Fluid Dynamics

FFT = Fast Fourier Transform

GOX = Gaseous OXygen

HDPE = High Density PolyEthylene

HTPB = Hydroxyl Terminated PolyButadiene

MUSCL = Monotonic Upstream-centered Scheme for Conservation Laws

NASA = National Aeronautics and Space Administration

TNT = Tri-Nitro Toluene

CHAPTER – 1

INTRODUCTION

1.1 The Hybrid Rocket

In the broadest of scope, a hybrid rocket can be considered as a chemical propulsion system which uses both solid and liquid as propellants. In the more typical and so-called classical hybrid, the fuel is in solid state and the oxidizer is in liquid/gaseous state. A schematic of a typical classical hybrid rocket is shown in Fig. 1.1 [1-1]. Even though commonly assumed to be placed between the solids and the liquids - which is fair to say only in terms of performance, hybrid rockets inherently different compared to these two systems when their method of operation is compared. In solids, the fuel and the oxidizer are intimately mixed and cast into a single solid phase. The combustion occurs at the surface of the solid fuel which is heated by the reaction flame to the ignition temperature. This essentially leads to microscopic diffusion combustion. In liquid both the oxidizer and the fuel are intimately mixed near the injector to form a pre-mixed combustion mixture, which then burns inside the combustion chamber. Therefore, in both these cases, throughout the combustion chamber there is a uniform mixture of oxidizer and the fuel. However, in the hybrid rocket, the combustion occurs in the form of a macroscopic turbulent diffusion flame. Hence, along the length of the combustion chamber, the value of oxidizer to fuel ratio (O/F) varies and it ends at a composition which determines the rocket performance.

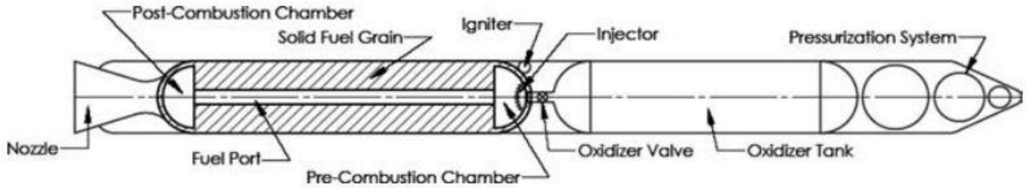

Fig. 1.1 Classical hybrid rocket schematic highlighting the key components of the system [1-1]

In the recent years, the interest in the research on hybrid rockets has grown by large. This is contributed to the necessity of reliable, safe and cost-effective orbital launch systems for increasingly growing number of satellites. Fig. 1.2 shows the prediction of the estimated number commercial orbital launches for the next decade [1-2]. It predicts that the number of launches is going to increase by a minimum of 40% compared to the actual launches in the year 2017.

With multiple mega satellite constellations being planned for the next decade, the demand for the rocket launches is only going to be more and hence it will spur the growth of research in development of better launch systems. The specific interest in hybrid systems is because of the alternative and attractive option of using them instead of the conventional liquid and solid systems. In general liquid rockets are high-performance and efficient chemical propulsion systems. However, they suffer from the pitfalls of complexity and the requirement of extensive plumbing. Solid rockets are much simpler as they have both the oxidizer and the fuel premixed. Therefore, they are lower in cost and easier to design. However, the main disadvantage is the explosive danger and the inability for thrust control and termination. This is where the hybrid rocket has an advantage. With half of the plumbing of the liquid rocket, but retaining its operational flexibility and eliminating the risk of explosion [1-3], it provides a unique alternative from the typical modes of chemical propulsion.

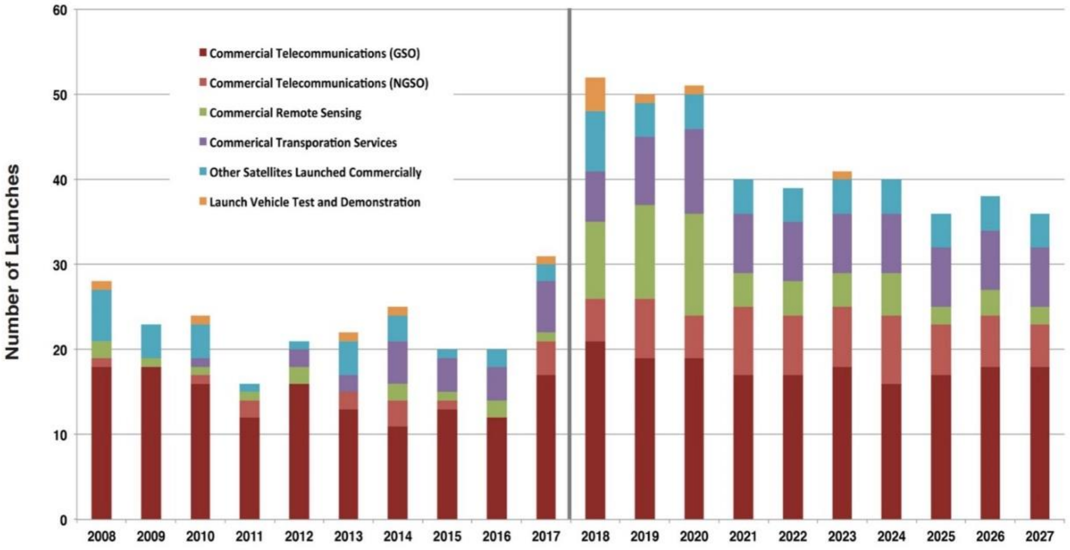

Fig. 1.2 Historical and projected commercial orbital launches [1-2]

1.2 Advantages and Disadvantages

In this section the fundamental differences between the classical hybrid and the liquid or solid rocket is explained. The advantages are followed by the disadvantages.

i. Safety: The solid fuel is inert and hence can be manufactured, transported and handled safely as per conventional commercial practice. An intimate mixture of fuel and oxidizer is never possible. So, the possibility of a run-off leading to an explosion is none. In fact, the TNT equivalent of hybrids are defined to be zero. This is one of the main reasons why hybrids are a very popular consideration for human space flight and space tourism. For example, the rocket motors powering the commercial sub-orbital space tourism spacecrafts – the SpaceShip One and the SpaceShip Two are hybrid rockets powered by a HTPB/N2O motors as shown in Fig. 1.3.

ii. Grain robustness: Since, in hybrids the burning occurs only down the port of the chamber where the liquid oxidizer is encountered, cracks in the solid fuel will not lead to catastrophic explosion as it happens in the solid rocket case.

iii. Propellant versatility: The selection of propellants for hybrids is theoretically more than of liquids and solids alone. Dense energetic materials as solid fuel can be used to increase the energy density and at the same time liquid oxidizers can be used to provide higher energy levels.

iv. Low cost: Due to the safety and ease of usage associated with the hybrids, the total operational costs are greatly reduced when using hybrid systems. The cost reduction can come from reduction in handling costs, manufacturing costs and transportation of fuel/oxidizer costs.

Fig. 1.3 Hybrid rocket in operation during the flight test of the VSS Unity [1-4]

Despite the advantages, the following are some of the common disadvantages associated with hybrid rockets,

i. Low regression rate: The regression rates of hybrids are typically lesser than solids and this results in either long combustion chambers or multiple ports to provide enough burning surface to obtain the required thrust. This also results in low volumetric fuel loading. This was one of the major challenges that was faced by the AMROC motor company that tested hybrid rocket motors for adoption following the 1986 Challenger disaster. However, new formulated liquifying fuels and novel oxidizer injection techniques have the potential to eliminate this problem.
ii. O/F shift: During its operation, the port radius constantly increases resulting an O/F shift with time, which can cause lower theoretical performance. Although, with proper design, control and novel oxidizer injection techniques this shift can be reduced.
iii. Slower transients: In general, the thrust response to throttling is slower in hybrids, because of the inherently different nature of mixing of fuel/oxidizer and combustion in hybrids.
iv. Combustion Instability: Low frequency combustion instabilities have been commonly observed across a wide scale of rocket motor firings. These complex transient phenomenon needs to be carefully studied, understood and eliminated in order to prevent potential motor failures. This theme would be the central scope of this thesis.

1.3 Boundary Layer Combustion

The above-mentioned characteristics, the advantages and the disadvantages all can be explained through the mechanism of combustion in hybrid systems which is its most unique feature - the presence of a macroscopic diffusion flame. Fig. 1.4 describes clearly the processes occurring in the boundary layer combustion in hybrids. After ignition, a chemically reaction boundary layer begins to form over the surface of the fuel, starting from the head end of the motor. The boundary layer is typically turbulent due to the high axial injection Reynolds number used in hybrids. This region is characterised by strong velocity, temperature and their gradients normal to the surface. The transport of mass, momentum and energy are dominated by the turbulent flow characteristics.

After ignition, the diffusion flame region forms in the boundary layer. The flame usually resides at an approximate location of 10 - 20 % boundary layer thickness above the regressing surface. Heat from the flame reaches the surface of the solid through all the three forms of heat transfer - conduction, convection and radiation. This influx of energy to the solid fuel surface causes it to undergo pyrolysis. During pyrolysis, both the physical state and the chemical composition of the fuel changes. The pyrolyzed fuel then reaches the flame region by convection and diffusion. Here, it mixes with the oxidizer which had been transported to the flame region from the core flow through turbulent processes. The fuel and the oxidizer react and provide further heat for pyrolysis and the whole process is hence sustained. The fuel mass flux due to pyrolysis, results in the shielding/blocking of the heat transfer from the flame region to the surface, which in turn causes a decrease in the regression rate and hence corresponding strength of the wall blowing effect and in turn, a weakening of the blocking action, allowing more heat to reach the surface. This results in a self-regulatory mechanism in hybrids comprising of the interaction between heat flux, blowing effect and heat flux blockage. This is one of the distinguishing characteristics of the hybrid systems.

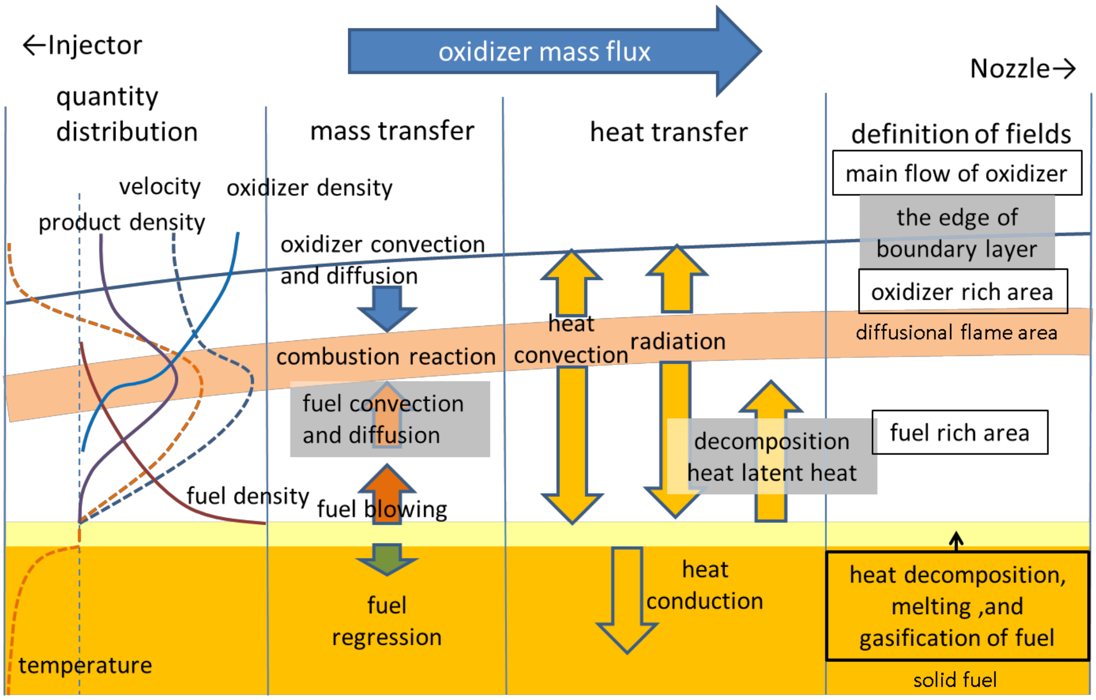

Fig. 1.4 Processes in Turbulent Boundary Layer Combustion

To be noted is that in hybrids, the gas flow is always within the annular region of the solid fuel. Hence, it can be resembled to an internal pipe flow. Therefore, as a natural corollary, it is expected that the gas in the core flow will undergo acceleration in the axial direction, due to constant addition of fuel mass and increase in pressure due to the combustion. Since, the boundary layers also grow continuously in the axial direction, they meet at some point downstream (usually L/D - 5). After this, the properties within the boundary layer downstream this axial location are different compared to upstream values, and when studying chamber configurations with long L/D ratios, this must be considered.

1.4 Combustion Instability

In the design of any chemical propulsion system, the combustion instability plays a very important role. It is also one of the most difficult aspects of the development. The system must be designed so that the oscillations due to the instabilities do not result in compromise of the mission parameters. During its run, a rocket may have a host of transient phenomena that can potentially couple to the instability and leading to a growth in the chamber pressure oscillations. Therefore, it is impertinent to have a thorough understanding of the transient combustion characteristics, so that its stability behaviour can be predicted.

Development of hybrid rockets began as early as the 1930s and since then the field has had varying popularity with many different experiments being conducted with different rocket parameters. However, one phenomenon which has been widely reported over a wide range of motor specifications [1-5,1-6] is a type of low-frequency instability, coined the name, 'Intrinsic Low Frequency Instability (ILFI). This non-acoustic instability has been found to be unique to hybrid systems. The frequency range of the pressure fluctuations is typically in the lower end of the frequency spectrum (5-50Hz). Fig. 1.5 shows the pressure-time trace of a paraffin-based/GOX hybrid tested [5]. It is very clear that the instability is decoupled from the feed pressure. Also seen is that the pressure oscillations do not grow unbounded. Fig. 1.6 shows a Fast Fourier Transform (FFT) for the same test shown in Fig. 1.5 [1-5], where the low frequency spectrum is clearly visible.

One of the main, if not the most important parameter in hybrid rocket design in the regression rate which is defined as the rate at which the solid fuel is converted into gaseous fuel. Regression rate directly influences the mass addition of fuel to the oxidizer flow field and is strongly affected by the various processes resulting in the turbulent boundary layer. Fluctuations to the regression rate can cause unplanned thrust fluctuations and result in excessive structural/thermal loading, which may prove fatal to the mission success.

In general, it is seen that the oscillations in hybrid systems are fortunately limited to 50-60% of the mean chamber pressure, and hence do not typically result in unbounded large-amplitude oscillations such as that occurring in solid systems and which results in catastrophic explosion. However, these oscillations are still significant enough to cause mission failure and hence warrants extensive understanding of the various phenomena that contributes to the instability.

Therefore, before commercial production and usage of hybrid systems can be realized, it is clearly necessary to completely understand the mechanism(s) associated with the generation of ILFI and the parameters which influence it. Ways to control the different non-linear effects such as limit cycle amplitude or DC shift during the instability must also be devised. An exploration of the physical processes causing this instability would be the core theme of this thesis.

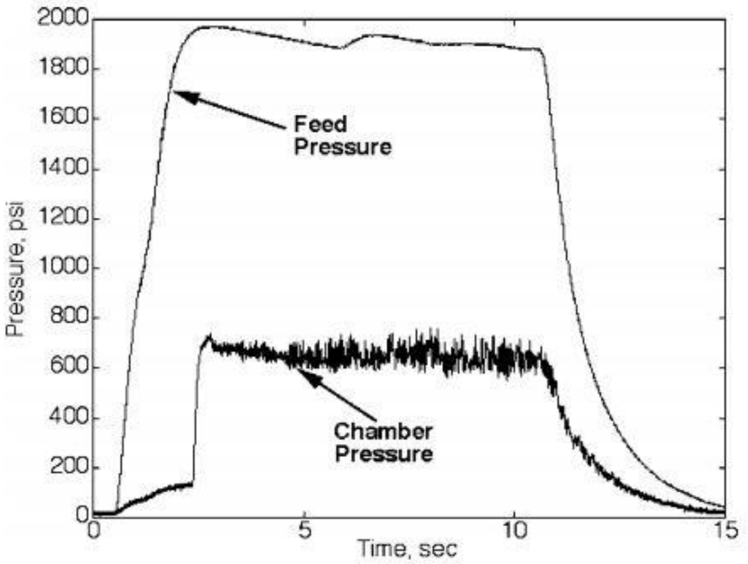

Fig. 1.5 Pressure-time trace for a GOX/paraffin-based hybrid motor [1-5]

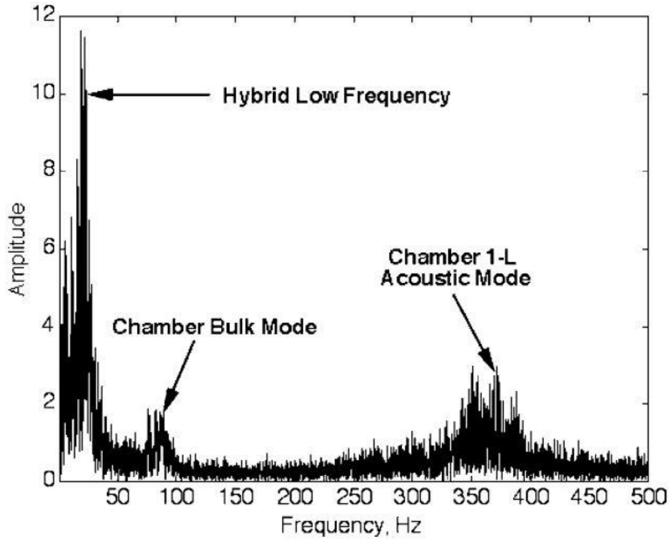

Fig. 1.6 FFT plot of a pressure-time trace of a typical paraffin-based motor [1-5]

1.5 Structure of the Thesis

The thesis is structured into a total of 5 chapters. As seen, Chapter 1 introduced to the reader, an explanation of the basics of the hybrid rocket motors, why they are an excellent choice for the next generation of chemical propulsion systems and some of the problems plaguing their development. Also, an introduction was given to the unique mechanism of macroscopic turbulent boundary layer combustion present in hybrids. Further, the problem of combustion instability in hybrids was introduced.

Chapter 2 would deal with review of the existing research in the open literature available with regards to the problem of the hybrid rocket combustion instability. This chapter would then define the limitations of the existing models available for prediction of combustion instability and therefore define the scope of the thesis.

In Chapter 3, a physical explanation of the presence of combustion instability in hybrid rockets in explained through developed generalized analytical models for oscillatory regression rates in hybrid rockets. Further, the limitations of analytical models in capturing the entirety of the phenomenon would be explained warranting the usage of numerical modelling in order to further study the problem.

Chapter 4 explains the numerical methodology used and the coupling between the different numerical models constructed. The results of grid convergence tests are shown as well as validation of the numerical model through comparison with experimental data for prediction of time and spatial averaged steady state regression rates.

Chapter 5 deals with an in-depth study of the transient process of combustion instability in hybrids using the constructed numerical model. The effect of different parameters on the stability behaviour of the rocket motor are explained. Further comparisons are made with experiments, for the prediction of non-linear characteristics during the combustion instability obtained with the developed numerical model.

Chapter 6 wraps up the discussions in the previous chapters and concludes with the salient features of the thesis. Future work possible in this area are also discussed.

1.6 References for Chapter 1

[1-1] Chiaverini, M., Review of Solid Fuel Regression Rate Behaviour in Classical and Nonclassical Hybrid Rocket Motors, Fundamentals of Hybrid Rocket Combustion and Propulsion, edited by M. J. Chiaverini, and K. K. Kuo, Vol. 218, Progress in Astronautics and Aeronautics, AIAA, Reston, VA, 2007.

[1-2] Federal Aviation Administration (FAA). The Annual Compendium of Commercial Space Transportation: 2018. Washington, DC: FAA Office of Commercial Space Transportation, 2018.

[1-3] A. Takahashi and T. Shimada. "Essentially Nonexplosive Propulsion Paving a Way for Fail-Safe Space Transportation". In: 31st ISTS Japan. 2017.

[1-4] www.virgingalactic.com. Accessed 20 November, 2018.

[1-5] Karabeyoglu, A., Zilwa, S.D., Cantwell, B. and Zilliac, G., 2005. Modeling of hybrid rocket low frequency instabilities. Journal of propulsion and power, 21(6), pp.1107-1116.

[1-6] Karabeyoglu, A., 2007. Combustion instability and transient behavior in hybrid rocket motors. Progress in Astronautics and Aeronautics, 218, p.351.

CHAPTER – 2

LITERATURE REVIEW

This chapter highlights the important research carried out so far in the area of instabilities in hybrid rockets. Knowing this would help us define the domain and scope of our problem succinctly – which would form the motive of this thesis research.

2.1 Survey of existing research

The phenomenon of combustion instabilities in hybrid rockets have been relatively well documented before in literature. Boardman et. al. [2-1, 2-2] conducted experimental investigation on combustion instability in 11-inch and 24-inch diameter and 1500 lbf thrust HTPB/PCPD and LOX [2-2]/GOX [2-1] hybrid rocket motors. Large amplitude low-frequency instabilities were seen in all the experiments coincident with acoustic oscillations. The tests on the 11 and 24-inch AMROC and JIRAD motors showed instability in the pressure range of 2-3 Hz and 8-15 Hz (clearly non-acoustic) respectively. The amplitude of the pressure oscillations was 15-20 % and 5- 60 % of the mean chamber pressure for the AMROC and JIRAD motors respectively. It was found injection patterns and other design changes such as presence of fuel fins or bluff-body flame-holders which resulted in flowfield conducive to efficient flame holding near the port entrance relatively increased the stability of the motors. Fig. 2.1 shows the representative unstable behaviour in a JIRAD motor.

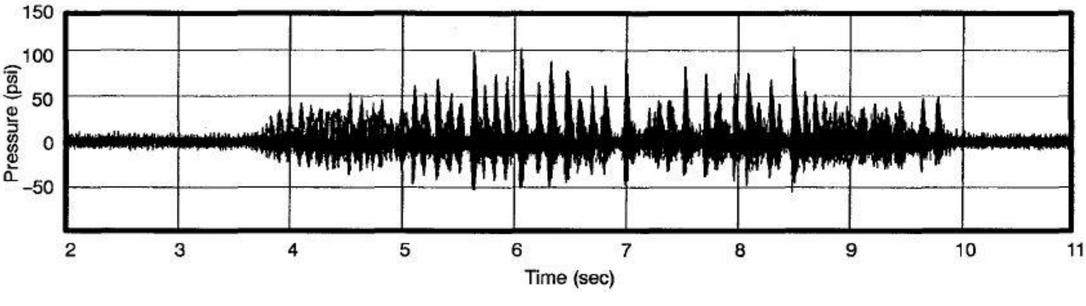

Fig. 2.1 High frequency chamber pressure versus time – Test 1 [2-2]

Griener et. al. [2-3] highlighted the effect of vortex shedding in the stability behaviour of hybrid rocket motors and argued that the coupling of the vortex shedding frequency (associated with the Kelvin-Helmholtz type instability) with the acoustic frequencies resulted in the combustion instabilities. Similar theory based on parietal vortex shedding due to the interaction between a turbulent oxidizer stream and an evaporating surface fuel flow, has been proposed by Kim et. al. [2-4]. However, this theory does not explain the reason behind why changing the post-combustion chamber length did not affect the stability characteristics of the motor. It also doesn't explain why the low-frequency instability in hybrids scale with the port length. Further, in experiments and numerical simulations by Jerome et. al. [2-5] failed to capture the low-frequency combustion instabilities.

Similar findings have been reported by more recent experimental investigations by Carmicino et. al. [2-6] on experiments with lab scale hybrid rocket motors. Like Boardman's results, it is reported that axial injection resulted in more stable behaviour compared to radial injections of oxidizer. Similarly, vortex shedding in the post combustion chamber were considered as driving mechanisms for large scale pressure oscillations. But still a theory that could explain the prevalence of low-frequency instability across wide scaled rocket motors could not be established.

One other reason that was provided was the vaporization lag of the liquid oxidizer which might couple with the combustion and fluid flow processes and result in an instability [2-7]. However, this theory fails to explain the presence of the instability even in the case of the usage of gaseous oxidizers, where there is no vaporization lag [2-1].

Jenkins et. al. attempted to explain this phenomenon through an analogy to the L* instability in solid rockets [2-8]. Coupling of regression rate to pressure in hybrids may occur only under extreme regions of operation - at high oxidizer mass flux because the system becomes chemical kinetics controlled and at low oxidizer mass fluxes where the effect of radiation may be significant over the effect of convective heat flux. This is clearly shown below in Fig. 2.2. [2-9].

Under this case, it has been shown that the pressure coupling can provide energy input to sustain instability analogous to solid rocket instability. However, this theory can only be applied to the afore mentioned extreme regions of operation and hence cannot give explanation for the phenomenon happening under normal operating conditions too.

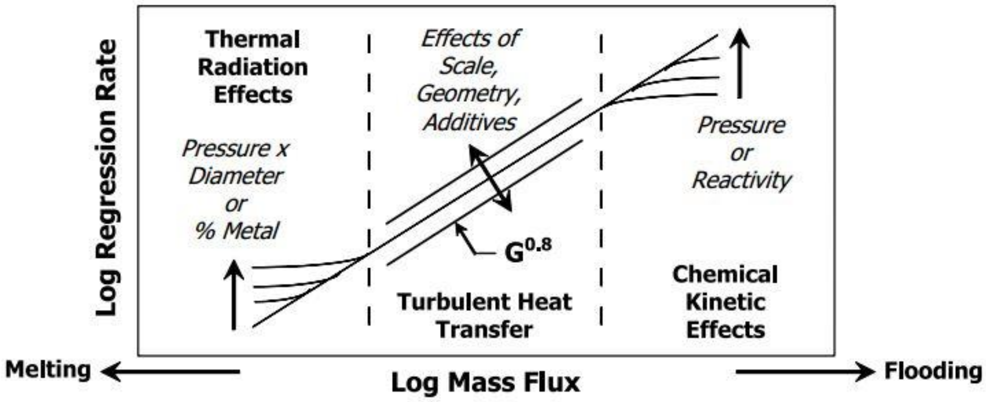

Fig. 2.2 Regions of regression rate dependency [2-9]

The most seminal work in this area was done by Karabeyoglu et. al [2-10, 2-11]. A semi-analytical model was proposed taking into consideration various time delays in the overall system. The combustion instability behaviour in hybrids was shown to be the result of the so-called ‘boundary layer delay’ in hybrids - which is the delay for the boundary layer to adjust itself to changes. The model could also explain that the instability was inherent/intrinsic to hybrid rocket motors due to the nature of diffusion flame. This model has been able to successfully determine the frequency range of the ILFI reported in experimental literature. The frequency of the oscillations was given by the formula below,

$$f_{ILFI} = 0.234\left(2 + \frac{1}{OF}\right)\left(\frac{G_o R T_{avg}}{L P_C}\right) \tag{2.1}$$

However, the model fails to provide a quantitative estimate of the amplitude of the frequencies. Due to the linearized modeling, it also predicts an infinite growth of the oscillation, whereas the ILFI is of limit-cycle region. The model hence captures only the linear region of the stability as limit-cycle is essentially a non-linear phenomenon. Therefore, this analytical approach has certain limitations and further research is needed to establish a process for determination of the non-linear characteristics of combustion instability.

Due to the inherent high costs associated with the testing of instability through experimental approach and limitations associated with the analytical approaches, more recent investigations using numerical approach with computational fluid dynamics (CFD) have been carried out.

Barato et. al. [2-12] used a computational fluid dynamics approach to study this problem. When they modelled the above-mentioned boundary layer delay, it was found that the motor was unstable further verifying Karabeyoglu's theory. However, their CFD model and its applications are severely limited as the combustion chamber was modelled as a zero-dimensional model – resulting in no simulation of interaction with any acoustics and other real-world non-linear effects.

Another computational study was carried out by Stoia-Djeska et. al [2-13] in order to understand the transient behaviour in hybrid rocket motors. Note that compared to the above study, a 1-dimensional combustion chamber model was used. Therefore, theoretically the acoustics could be simulated. Like Barato's study, upon consideration of a boundary layer delay, the simulated system was found to be unstable. However, in their simulation, an exponentially increasing amplitude of pressure oscillation was reported. This is partly due to their erroneous consideration of averaged regression rates from experiments as the input rather than time-dependent calculation of regression rates. We will show later, that the hybrid rocket combustion instability is due to the coupling of both the thermal and the boundary layer time lags and one without the other cannot by themselves result in an instability.

Funami et. al [2-14] also tried to simulate the unsteady transient behaviour with a CFD approach. They attempted to pulse the motor with pressure oscillations in order to elicit an unstable response akin to a solid rocket motor. However, due to non-consideration of any boundary layer effect, naturally it was found that the system was stable for all pulsing.

It is well understood that the simulation of non-linear effects such as limit cycle amplitude and DC shift during a transient such as combustion instability is a difficult task. Few parallels in solid rocket literature exists [2-15] – Flandro et. al, showcase how non-linear estimations based on wave steepening can give a good estimate on the limit cycle amplitude, DC shift effects and triggering amplitudes.

J.P. Arves et. al. [2-16, 2-17] tried to explain the DC shift in hybrid motors based on the c* efficiency between the DC shifted regions. However, an estimation of the magnitude of such effects was not discussed.

However, to our knowledge no analytical/numerical study have been conducted so far that can capture the combustion instability phenomenon in hybrids in its entirety including both the linear stability characteristics and the effect of various practical rocket parameters on the non-linear effects.

This review thus opens the niche in literature that the thesis would address.

2.2 Aim of the Study

The design needs of the research would be to evaluate and predict the internal ballistics of a hybrid rocket motor during transient phenomenon such as combustion instability. In order to address this, a computational model would be developed for the transient simulation of an axial-injected hybrid rocket motor. This model should be able to:

- Capture the linear stability response characteristics of the motor (frequency of pressure and regression rate oscillations).
- Capture the characteristics of the non-linear response (such as limit cycle amplitude and DC shift)
- Predict the physical explanation and theory behind unstable behavioural response of hybrid motors.
- Predict if a given motor configuration would be intrinsically stable or not.

Further, using the model, parametric analyses would also be conducted in order to measure the effect of different parameters on the intrinsic hybrid rocket combustion instability behaviour.

2.3 References for Chapter 2

[2-1] Boardman, T.A., Brinton, D. H., Carpenter, R. L., and Zolods, T. F., “An Experimental Investigation of Pressure Oscillations and Their Suppression in Subscale Hybrid Rocket Motors,” AIAA Paper 95-2689, July 1995.

[2-2] Boardman, T. A., Carpenter, R. L., and Claflin, S. E., “A Comparative Study of the Effects of Liquid-Versus Gaseous-Oxygen Injection on Combustion Stability in 11inch-Diameter Hybrid Motors,” AIAA Paper 97-2936, July 1997.

[2-3] Greiner, B. and FREDERICK, JR, R., 1993, June. Hybrid rocket instability. In 29th Joint Propulsion Conference and Exhibit (p. 2553).

[2-4] Kim, B., Na, Y., Shin, K.-H., and Lee, C., “Nonlinear Combustion and Fluid Mechanics in a Hybrid Rocket,” Journal of Propulsion and Power, Vol. 28, No. 6, 2012, pp. 1351–1358.

[2-5] Messineo, J., Lestrade, J.Y., Hijlkema, J. and Anthoine, J., 2016. Vortex shedding influence on hybrid rocket pressure oscillations and combustion efficiency. Journal of Propulsion and Power, 32(6), pp.1386-1394.

[2-6] Carmicino, C., 2009. Acoustics, vortex shedding, and low-frequency dynamics interaction in an unstable hybrid rocket. Journal of Propulsion and Power, 25(6), pp.1322-1335.

[2-7] Guthrie, D. M., & Wolf, R. S. (1991). Non-acoustic combustion instability in hybrid rocket motors. *AIAA Paper*, *2916*, 11.

[2-8] Jenkins, R. M., and Cook, J. R., “A Preliminary Analysis of Low Frequency Pressure Oscillations in Hybrid Rocket Motors,” AIAA Paper 95-2690, July 1995.

[2-9] Chiaverini, M., 2007. Review of Solid-Fuel Regression Rate Behavior in Classical and Nonclassical Hybrid Rocket Motors. Progress in Astronautics and Aeronautics, 218, pp. 93.

[2-9] Karabeyoglu, A., Zilwa, S.D., Cantwell, B. and Zilliac, G., 2005. Modeling of hybrid rocket low frequency instabilities. Journal of propulsion and power, 21(6), pp.1107-1116.

[2-10] Karabeyoglu, A., 2007. Combustion instability and transient behavior in hybrid rocket motors. Progress in Astronautics and Aeronautics, 218, p.351.

[2-11] Barato, F., Bellomo, N., Faenza, M., Lazzarin, M., Bettella, A. and Pavarin, D., 2015. Numerical model to analyse transient behavior and instabilities on hybrid rocket motors. Journal of Propulsion and Power, 31(2), pp.643-653.

[2-12] Stoia-Djeska, M. and Mingireanu, F., 2010. A Computational Fluid Dynamics Based Stability Analysis for Hybrid Rocket Motor Combustion. In 16th AIAA/CEAS Aeroacoustics Conference (p. 3909).

[2-13] Funami. Y., Novozhilov, V. & Shimada. T. (2010). Unsteady Internal Ballistics of Hybrid Rocket: Quasi-1D Simulation. Asian Joint Conference on Propulsion and Power. Miyazaki.

[2-14] Flandro, G.A., Fischbach, S.R. and Majdalani, J., 2007. Nonlinear rocket motor stability prediction: limit amplitude, triggering, and mean pressure shift. Physics of Fluids, 19(9), p.094101.

[2-15] Arves, J., Jones, H., Arves, J. and Jones, H., 1997, July. Explanation of the' DC shift 'in hybrid motors. In 33rd Joint Propulsion Conference and Exhibit (p. 2938).

[2-16] Arves, J., Jones, H., Arves, J. and Jones, H., 1997, July. Elimination of 'DC shift' in hybrid motors. In 33rd Joint Propulsion Conference and Exhibit (p. 2939).

CHAPTER – 3

MODELING HYBRID ROCKET COMBUSTION INSTABILITY

This chapter explains the physical reasoning behind the presence of Intrinsic Low-Frequency combustion Instability (ILFI) in hybrid rocket motors. The concept of boundary layer delay is explained followed by an analogy to a simple non-linear oscillating system in order to portray ILFI occurring as a result of 'self-excited' oscillations. Further, an attempt is made to derive a generalized oscillating non-linear equation for regression rate in hybrids.

3.1 Modeling Hybrid Rocket Boundary Layer Combustion

As described in Section 1.2, the unique characteristic of hybrid rocket combustion is the presence of a macroscopic diffusion flame occurring in the turbulent boundary layer. Therefore, naturally, the heat released from the flame region (where the combustion is taking place), to the regressing fuel surface is dependent on the properties of the boundary layer. Naturally, the burning rate or the regression rate is also dependent on the properties of the boundary layer. In hybrids (mainly the axial-injection variant), the primary variable through which the regression rate can be controlled is through controlling the quantity of oxidizer injected. This change results in a change to the local port mass flux which in turn changes the heat-feedback from the flame to the burning fuel surface (wall). However, modeling this transient is not straight forward as the response of the heat-feedback to the fuel is also dependent on the regression rate itself due to the blowing/blowing effect, as in hybrids, the presence of unburnt fuel decreases the amount of heat from the flame reaching the regressing surface. The analytical modelling of this complex heat-feedback was originally done by Marxman et. al. [3-1] for steady state combustion and extended for quasi-steady transient phenomenon by Karabeyoglu et. al. [3-2]. For the sake of completeness, the formulation is derived below.

With the assumption that the radiative heat-flux is negligible, the total heat-flux to the wall $Q_w(t)$, is equal to the convective heat flux $Q_c(t)$. This is a valid assumption for the analysis done here. This is because, if the radiative heat transfer is considered, then it automatically reduces the convective heat transfer due to an increase in the regression rate, resulting in increased blockage effect. This results in such that, the total heat transfers due to both the convective and the radiative components, doesn't change much compared to when only considering the convective heat transfer. However, care should be noted that this assumption is valid only for cases where metallized particles or soot are not present, as the presence of such particles greatly reduce the regression rate due to radiation.

The instantaneous convective heat flux from the flame to the regressing fuel surface can be expressed as,

$$Q_c(t) = C_h \rho_{fl} u_{fl} \left(h_{fl} - h_{sr} \right) = C_h \rho_{fl} u_{fl} \Delta h \tag{3.1}$$

where h_{fl} *and* h_{sr} are enthalpies at the flame and at the regressing fuel surface.

Assuming, that the classic Reynolds analogy exists and that the Lewis and Prandtl number are equal to 1 during such a quasi-steady transient behavior, the heat transfer coefficient, C_h can be replaced by the aerodynamic parameter of the boundary layer, the coefficient of skin friction, C_f. This results in the convective heat flux expression being,

$$C_h = \frac{1}{2} C_f \left(\frac{\rho_e u_e^2}{\rho_{fl} u_{fl}^2} \right) \tag{3.2}$$

$$Q_{c0} = \frac{1}{2} C_f G_0 \left(\frac{u_e}{u_{fl}} \right)_0 \Delta h \tag{3.3}$$

where, G is the total local mass flux at the port, $\rho_e u_e$.

Note that due to the application of Reynolds's analogy, the expression for the convective heat flux as given by Eqn. 3.3 is valid only for steady state analysis. An analytical expression for the unsteady convective heat flux is not known apriori and therefore subsequent modification is required before its application in unsteady analysis. This would be discussed in detail in the next chapter.

Now, the skin coefficient friction, C_f in hybrids is not known apriori due to the unique nature of turbulent boundary layer with the presence of wall injection. Therefore, in *general* this parameter is represented by equating it the well-known skin coefficient friction for a turbulent boundary layer without any wall injection, C_{f0} and then multiplying it by a unique factor C_f/C_{f0}, (which we would like to call, the skin-coefficient ratio) that encapsulates the effect of wall blowing. It should be noted that this parameter is dependent on the regression rate, as the presence of more regression rate equates to an increase in the quantity of wall injection which in turn changes the boundary layer properties.

$$Q_{c_0} = \frac{1}{2} C_{f0} \left(\frac{C_f}{C_{f0}}\right)_0 G_0 \left(\frac{u_e}{u_{fl}}\right)_0 \Delta h \tag{3.4}$$

An estimate of the value of u_e/u_{fl} was provided by Marxman [3-1] by using integral technique of boundary layer theory as,

$$\frac{u_e}{u_{fl}} = [(K_{ox} + OF + K_{ox})\left(\frac{\Delta h}{h_v}\right)]/[\left(OF\left(\frac{\Delta h}{h_v}\right)\right] \tag{3.5}$$

In order to quantify this effect, a new parameter is defined called the aerodynamic blowing parameter (Spalding's mass transfer number),

$$B_a = \frac{(\rho v)_w}{\frac{GC_f}{2}} \tag{3.6}$$

This blowing parameter, B_a is an important dimensionless parameter in boundary layer flow as it is an aerodynamic similarity parameter i.e. the velocity profiles in the boundary layer are similar when B_a is constant.

Now, the ratio of C_f/C_{f0}, which is the ratio between skin coefficient friction with and without surface injection (blowing), can be calculated as a function of the aerodynamic parameter B_a. Note that $C_f/C_{f0} = C_h/C_{h0}$, when Pr=1. The derivation for the same is expressed well in literature [3-3], and is given by,

$$\frac{C_f}{C_{f0_0}} = \frac{C_h}{C_{h0}} = \left(\left[\frac{\ln(1+B_a)}{B_a}\right]^{\frac{4}{5}} \left[\frac{\left(1+\frac{13B_a}{10}+\frac{4B_a^2}{11}\right)}{(1+B_a)\left(1+\frac{B_a}{2}\right)^2}\right]^{\frac{1}{5}}\right)_0 \tag{3.7}$$

This ratio is given by Fig. 3.1 [3-1],

As seen from Fig. 3.1, the complex form in Eqn. 3.6 can be expressed in simpler terms by fitting different curves.

For example, with a power law fit, it can be expressed as,

$$\frac{C_f}{C_{f0}} = qB_a^{-k}; \quad q = 1.2, \; k = 0.77 \tag{3.8}$$

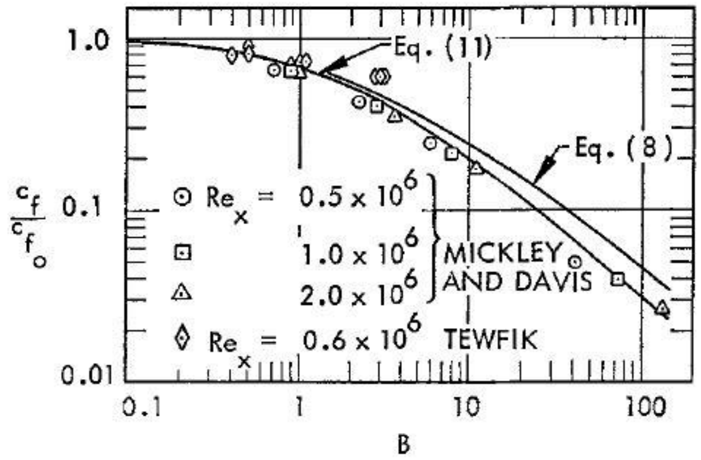

Fig. 3.1 Effect of blowing parameter on ratio of skin-coefficient friction [3-1]

This expression can be express the value of ratio of coefficient of skin friction with good accuracy over a large value of B_a. However, care should be excised while making its implementation at lower B_a values as the power law fit can result in non-physical values of even greater than 1 (See Fig. 3.2). Care should also be taken on the consideration of the combination of values of *{q, k}* for different ranges of B_a. For example, in the range of $1 \leq B_a \leq 15$, the best combination of *{q, k}* lies in the range of *{0.77-0.99, 0.5-0.6}*. In our study, the value of C_f/C_{f0} is artificially limited to the physically maximum value of 1 even if the value provided by Eqn. 3.8 is higher than that.

The expression in Eqn. 3.7 can also be simply expressed as,

$$\frac{C_f}{C_{f0}} = \frac{\ln(1 + B_a)}{B_a} \tag{3.9}$$

which is the same as given by Lees [3-4] formulation obtained by using a ‘film sheet theory’.

Additionally, Eqn. 3.7 can be expressed as in an inverse power law fit as,

$$\frac{C_f}{C_{f0}} = q^k(q + B_a)^{-k} \tag{3.10}$$

This expression gives a more accurate fit of the equation, as when $B_a \rightarrow 0$, $C_f/C_{f0} \rightarrow 1$, which is physically correct. The difference in using different functional forms for the expression of C_f/C_{f0} is shown below in Fig. 3.2,

Continuing the derivation of Eqn. 3.3 and assuming a power law fit as in Eqn. 3.6, Eqn. 3.4 can be written as,

$$B_a = \left(\frac{(\rho v)_{wall}}{\frac{qGC_{f0}}{2}}\right)^{\frac{1}{1-k}} = \left(\frac{\dot{r}\rho_f}{\frac{qGC_{f0}}{2}}\right)^{\frac{1}{1-k}} \tag{3.11}$$

Under steady state condition, B_a reduces to B_t which is the thermochemical blowing parameter, which is a thermodynamic constant that characterizes the system.

$$B_t = \left(\frac{u_e}{u_b}\right) \Delta h/h\_\nu \tag{3.12}$$

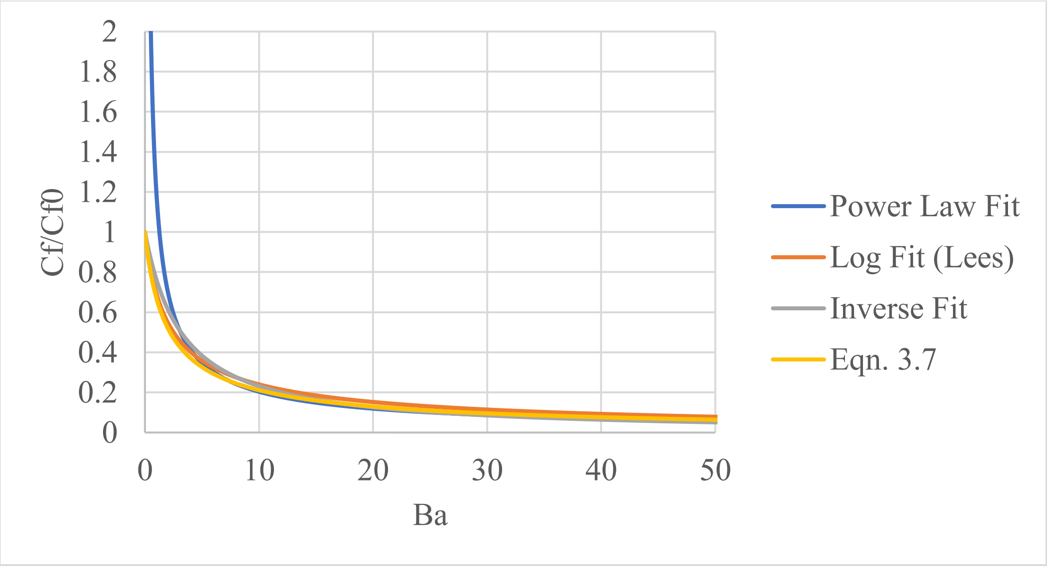

Fig. 3.2 Variation of ratio of coefficient of skin friction based on different functional forms of blowing parameter

Reducing the Eqn. 3.3 with Eqn. 3.9, and considering that $Cf_{0/2} = 0.03(Gz/\mu)^{(-0.2)}$ results in,

$$Q_{c_0} = \left(\frac{0.03q}{\mu}\right)^{\frac{1}{1-k}} \left(\frac{B_t h_v}{\rho_f^{\frac{k}{k}-1}}\right) x^{-\frac{0.2}{1-k}} \; G_0^{\frac{\dot{0}.8}{1-k}} \; \dot{r}_0^{\;-\frac{k}{1-k}} \tag{3.13.1}$$

This is the expression for the steady state convective heat flux felt by the wall (regressing fuel surface) in hybrid rocket motors. Here, $\dot{r}$ is the local regression rate. It should be well understood that the convective heat flux is dependent on the regression rate itself due to the blowing/blocking effect.

Note that form of convective heat flux as given by Eqn. 3.13.1 is valid only for steady state analysis and modification is required in order to extend it for usage in unsteady analysis. As first approximation, it is assumed that Reynold's analogy is valid in unsteady analysis and therefore the convective heat flux can be calculated as a function of the aerodynamic properties of the boundary layer. Next, it is assumed that the ratio of coefficient frictions with and without blowing (of the form in Eqn. 3.8-3.10) is also valid during unsteady analysis. However, it would be shown in the next section that the expression as given in 3.13.1 that is modified by the considerations above is also not accurate in representing the unsteady convective heat flux and further modification is necessary.

3.2 Boundary Layer Delay

During the derivation of the expression for convective heat flux in hybrid rockets (till Eq. 3.13), it was assumed that $Q_c(t)$ is dependent on $\dot{r}\,(t)$ – this is valid only if it is assumed that the changes to the regression rate instantaneously changes the heat flux. This means that the boundary layer responds and changes itself quickly and without any delay to the changes in the regression rate. However, this assumption is not valid in hybrid rocket motors.

This is because of the finite time needed for the boundary layer to adjust itself to any disturbance – either from the boundary layer edge or from the regressing surface. This finite delay will be called as the 'boundary layer delay' and it is dependent on the turbulent diffusion timescale across the boundary layer – which means that it is dependent on the turbulent diffusion speed and the thickness of the boundary layer. While the expression in Eqn. 3.13 is valid for steady state condition, in order to use it for unsteady analysis, a modification is necessary. As a first approximation, this modification is done by the consideration of simple first order boundary layer delay.

For the standard incompressible turbulent boundary layer, the boundary layer thickness can be expressed as,

$$\delta = 0.37xRe_x^{-0.2} \tag{3.14}$$

Here, Re is the local Reynolds number given by, $Re = u_e\rho x/\mu$

And the diffusion speed can be expressed in terms of the shear stress and fluid density as,

$$u_{bl} = \sqrt{\frac{\tau_0}{\rho}} = \sqrt{\frac{0.03\rho u_e Re_x^{-0.2}}{\rho}} \tag{3.15}$$

Resulting in the expression of boundary layer time delay (for incompressible flow over flat plate without surface injection) as,

$$\tau_{bl}(x,t) = \frac{\delta}{u_{bl}} = \frac{2.18Re_x^{-0.1}(t)x}{u_e(t)} \tag{3.16.1}$$

In hybrid rocket engines, this value of τ_{bl} will be slightly different due to the increase in the thickness of the boundary layer due to surface (wall) injection. Also, since the dependence on regression rate is weak for large values of Re as in hybrid rockets, it can be replaced by a single constant. Therefore, this value can be obtained empirically from experimental data [3-5] as,

$$\tau_{bl}(x,t) \approx 2.55x/u_e(t) \tag{3.16.2}$$

In order to model this boundary layer delay, the convective heat flux equation 3.4 must be modified as,

$$Q_c(t) = \frac{1}{2}C_{f0}\left(\frac{C_f}{C_{f0}}\right)_{(t-\tau_{bl})} G\left(\frac{u_e}{u_{fl}}\right)\Delta h \tag{3.17}$$

Expanding this into Eqn. 3.13, the delay in the wall heat flux to adjust itself to changes to the regression rate can be written as,

$$Q_c(t) = \left(\frac{0.03q}{\mu}\right)^{\frac{1}{1-k}} \left(\frac{B_t h_v}{\rho_f^{\frac{k}{k}-1}}\right) x^{-\frac{0.2}{1-k}}\ G(t)^{\frac{0.8}{1-k}}\ \dot{r}(t - \tau_{bl}(x,t))^{-\frac{k}{1-k}} \tag{3.18}$$

It was analysed by Karabeyoglu et. al. [3-5] that consideration of such a delay resulted in an unstable behaviour in hybrids characterizing the ILFI phenomenon reported. Now, an explanation on why such consideration results in unstable behaviour would be explained.

3.3 Self-Excited Oscillations

Self-excited oscillations have been studied well in liquid rocket literature [3-6, 3-7] with regards to combustion instability. The idea has also been applied to general ducted flames [3-8] and more generalized systems [3-9]. However, the concept has never been applied to study the combustion instabilities in hybrid rocket motors.

The basic idea behind a ‘self-excited’ oscillation is that the driving force necessary for sustaining the oscillation is controlled by the oscillation itself (in comparison to forced oscillation, where a system is externally forced at different resonant frequencies). For the linear instability, this can be considered as due to a positive feedback into the system resulting in a ‘negative damping’. This can be envisioned as a stable open-loop system becoming unstable due to the presence of a feedback as shown in Fig. 3.3.

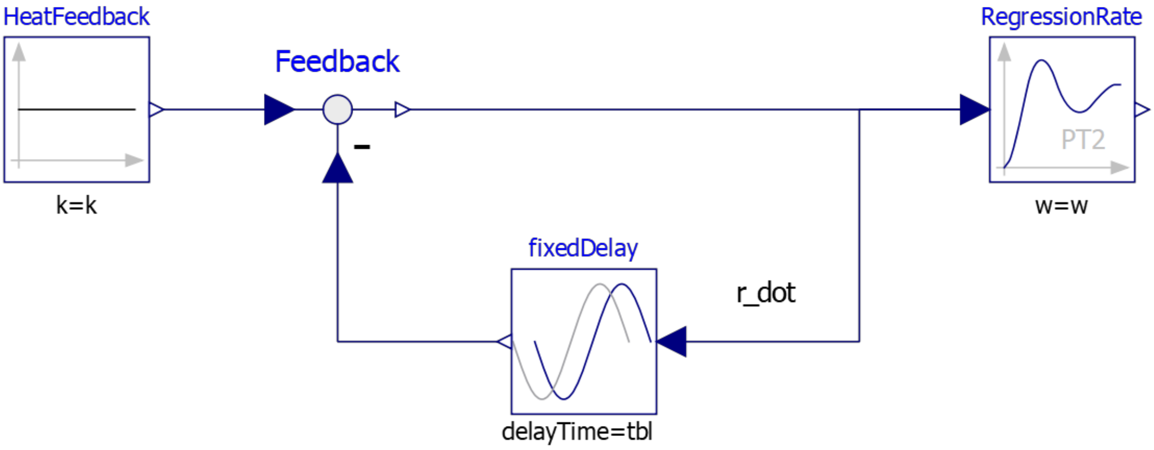

Fig. 3.3 Delayed dependence of heat feedback on regression rate

Consider a simple damped harmonic oscillator as shown in Fig. 3.4.

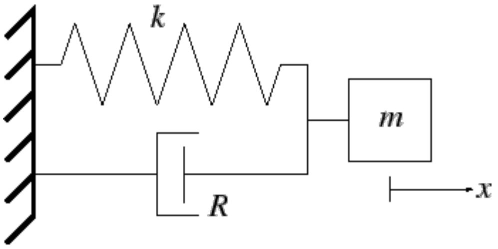

Fig. 3.4 Simple damped oscillating system

The equation of motion for the oscillator can be written as,

$$m\ddot{x}(t) + kx(t) + R\dot{x}(t) = 0 \tag{3.19}$$

Upon consideration of behaviour in which the restoring force in the system, *kx* is dependent not on the instantaneous time *t* but on the displacement at some time before *x(t-c)*, the oscillatory equation becomes,

$$m\ddot{x}(t) + \ kx(t - c) + R\dot{x}(t) = 0 \tag{3.20}$$

Expanding the term *kx(t-c)* by using Taylor series expansion, Eq. 3.20 can be written as,

$$m\ddot{x}(t) + \dot{x}(t)[-k + R] + (k)x(t) = 0 \tag{3.21}$$

As seen from Eqn. 3.21, the consideration of the time delay, results in a 'negative damping' term. The presence of this negative damping term results in an oscillating increase in the amplitude of the system. It should also be noted that the magnitude of the negative damping term is directly proportional to the value of the time delay implying that an increase in the time delay should increase the negative damping and therefore the rate of growth of the oscillations.

3.4 Analogy with a Generalized Non-Linear Oscillating System

In order to understand qualitatively, the effect of the magnitude of the time delay *c*, on the non-linear effects such as formation of a limit cycle, its amplitude, the DC shift and the non-linear frequency shift, let us consider a generalized non-linear equation of the Lienard type (with a negative damping term),

$$\ddot{x}(t) - f(x)\dot{x}(t) + x(t) = 0 \tag{3.22}$$

Assuming, *f(x)* is a simple polynomial equation with order 2 and of the type, $(c - x^2 + x)$,

$$\ddot{x}(t) - (c - x^2 + x)\dot{x}(t) + x(t) = 0 \tag{3.23}$$

Note that this oscillator has a negative damping term ($-c\dot{x}(t)$). Assuming arbitrary initial conditions $\dot{x}(t) = 0$ and $x=0.1$; it can be shown that just by relatively varying only the value of *t* (akin to the time delay), many different non-linear effects can be simulated.

The results are shown in Fig. 3.5 a-d.

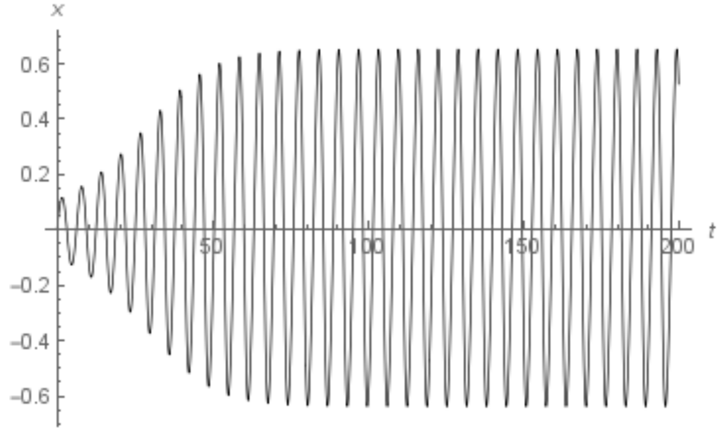

Fig. 3.5.a Presence of a limit cycle; $t = 0.1$

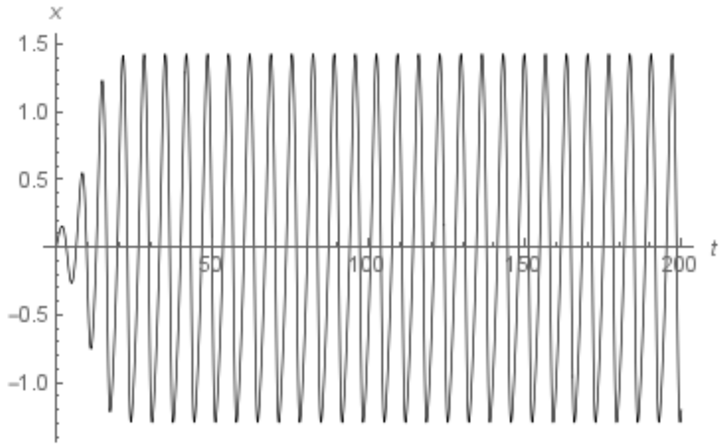

Fig. 3.5.b Increase in value of amplitude; *t = 0.*

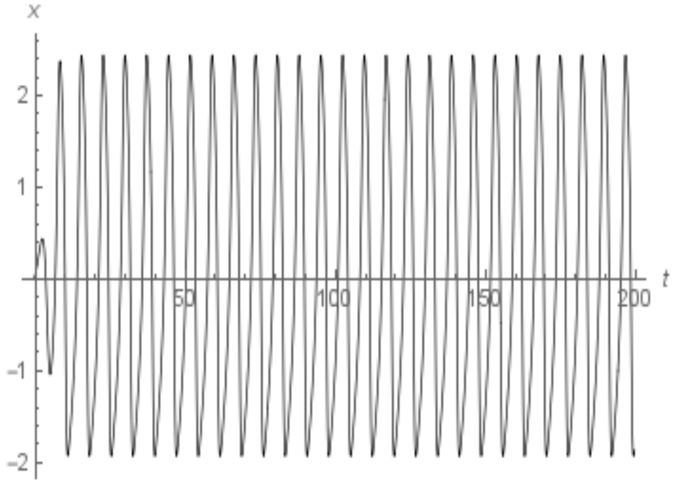

Fig. 3.5.c Finite DC Shift; *t = 1*

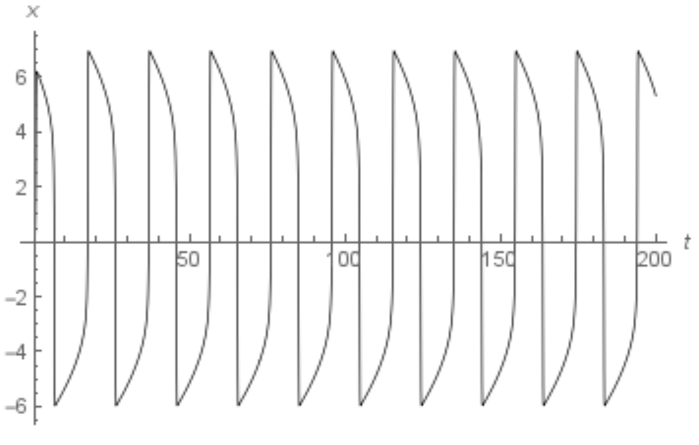

Fig. 3.5.d Non-linear frequency shift; *t = 10*

As can be seen from the results above, relatively the value of the time delay (which in turn affects the negative damping) can result in a variety of non-linear phenomenon. This is important to understand as it will be shown later with numerical simulation that it is indeed the case – with different boundary layer delay values, the non-linear effects are affected.

3.5 Derivation of Oscillatory Regression Rate Equation

An attempt is made here to derive the oscillatory regression rate equation like a non-linear form of Eqn. 3.23. In order to start with the derivation, let us consider the heat balance equation at the surface of the regressing fuel as shown in Fig. 3.6,

$$\lambda_g \left(\frac{\partial T}{\partial y}\right)_{y=+0}(t) = \lambda_s \left(\frac{\partial T}{\partial y}\right)_{y=-0}(t) + \rho_s \dot{r}(t) h_v \tag{3.24}$$

(1) (2) (3)

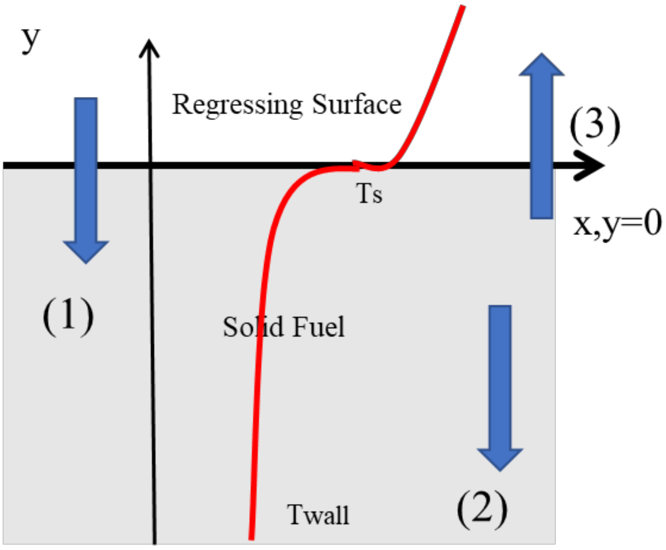

Fig. 3.6 Energy balance at the regressing fuel surface

The value of $\lambda_g \left(\frac{\partial T}{\partial y}\right)_{y=+0}$ is as given by Eqn. 3.18. The value of heat transfer into the solid fuel must ideally be calculated unsteadily. An analytical closed solution for the same is not available and hence, numerical model needs to be used to solve the same. However, as first attempt, the value of $\lambda_s \left(\frac{\partial T}{\partial y}\right)_{y=-0}(t)$ would be taken equal to the value at steady state with the assumption that the solid thermal fuel relaxation time is much larger than the boundary layer delay values. This results in the equation 3.24 being expanded as,

$$\left(\frac{0.03q}{\mu}\right)^{\frac{1}{1-k}} \left(\frac{B_t h_v}{\rho_f^{\frac{k}{k}-1}}\right) x^{-\frac{0.2}{1-k}} \; \dot{G}(t)^{\frac{0.8}{1-k}} \; \dot{r}(t-\tau_{bl}(x,t))^{-\frac{k}{1-k}} = (T_s - T_{wall})\frac{\lambda_s}{\alpha_s}\dot{r}(t) + \rho_s h_v \dot{r}(t) \tag{3.25}$$

Reducing this equation by considering only terms that are function of $\dot{r}\ (t)$ and considering a spatially averaged equation to remove dependence on *x*:

$$Af(\dot{r}(t-\tau_{bl})) = (T_s - T_{wall})\frac{\lambda_s}{\alpha_s}\dot{r}(t) + B\dot{r}(t) \tag{3.26}$$

Here, $A = \left(\frac{0.03q}{\mu}\right)^{\frac{1}{1-k}} \left(\frac{B_t h_v}{\rho_f^{\frac{k}{k}-1}}\right) x^{-\frac{0.2}{1-k}} \; \dot{G}(t)^{\frac{0.8}{1-k}}$; $B=\rho_s h_v$; $f(\dot{r}(t-\tau_{bl})) = \dot{r}(t-\tau_{bl}(x,t))^{-\frac{k}{1-k}}$

Assuming an Arrhenius relation for pyrolysis of the solid fuel,

$$\dot{r}(t) = A_c \exp(-\frac{E_a}{RT_s}) \tag{3.27}$$

Therefore, the surface temperature T_s can be expressed as a function of regression rate $\dot{r}\ (t)$ as,

$$T_s(t) = \frac{Ea/R}{logA_c - log\dot{r}(t)} \tag{3.28}$$

Now equation 3.26 can be further reduced as,

$$Af(\dot{r}(t-\tau_{bl})) = \left(\frac{D_1}{D_2 - log\dot{r}(t)}\right) + B\dot{r}(t) - D_3\dot{r}(t) \tag{3.29}$$

Here, $D_1 = \frac{\lambda_s}{\alpha_s}\frac{Ea}{R}$; $D_2 = \log A_c$; $D_3 = \frac{\lambda_s}{\alpha_s}T_{wall}$

Assuming, $\dot{r}\,(t\text{-}\tau_{bl}) = \dot{r}\,(t)\text{-}\Delta h$, where Δh is small enough so that the term can be expanded in a Taylor series,

$$Af(\dot{r}(t-\tau_{bl})) = Af(\dot{r}(t) - \Delta h) = A[f(\dot{r}(t)) - f'(\dot{r}(t)).\Delta h] \tag{3.30}$$

By definition, $\Delta h = \dot{r}\,(t) - \dot{r}\,(t\text{-}\tau_{bl}) = \dot{r}\,'(t).\ \tau_{bl},$

$$Af(\dot{r}(t-\tau_{bl})) = A[f(\dot{r}(t)) - f'(\dot{r}(t)).\dot{r}'(t).\tau_{bl}] \tag{3.31}$$

Therefore, Eqn. 3.29 can be written as,

$$A[f(\dot{r}(t)) - f'(\dot{r}(t)).\dot{r}'(t).\tau_{bl}] = \left(\frac{D_1}{D_2 - log\dot{r}(t)}\right) + B\dot{r}(t) - D_3\dot{r}(t) \tag{3.32}$$

As can be clearly seen from Eqn. 3.32, due to the consideration of a time delay, there exists a 'negative' damping in the system.

However, in order to bring this equation of the form of Eqn. 3.23 in a second order differential form equation for oscillatory motion, we take a derivative of Eqn. 3.33,

This results in,

$$\begin{aligned} A[f'^{(\dot{r}(t))} - [f''(\dot{r}(t)).\dot{r}'(t).\tau_{bl} + f'\dot{r}(t).\dot{r}''(t).\tau_{bl}]] \\ = \left(\frac{D_1}{\dot{r}(t)(D_2 - log\dot{r}(t))^2}\right) + (B - D_3)\dot{r}'(t) \end{aligned} \tag{3.33}$$

Assuming, k=0.5 in Eqn. 3.25 results in,

$$f(\dot{r}(t)) = \frac{1}{\dot{r}(t)}; \quad f'(\dot{r}(t)) = -\frac{1}{\dot{r}(t)^2} \quad ; \quad f''(\dot{r}(t)) = \frac{2}{\dot{r}(t)^3} \tag{3.34}$$

Substituting, Eqn. 3.34 in Eqn. 3.33 and simplifying; Taking $\dot{r}\ (t) = x$ symbolically,

$$x'' - x'\left[\frac{2}{x} + \frac{(B - D_3)x^2}{A\tau_{bl}}\right] - x\left[\frac{D_1}{A\tau_{bl}\ (D_2 - logx)^2}\right] - \frac{1}{\tau_{bl}} = 0 \tag{3.35}$$

This is the oscillatory regression rate equation in hybrids under the assumption that the thermal transient effects can be neglected (even though – this is not true in reality). Now, there is no closed form of solution for this second order ordinary differential equation. So, an attempt is made to solve it using a numerical integration.

For a given motor specification, the values of constants, *B, D1, D2, D3,* can be fixed. For example, in this case, the constants are estimated for a HDPE/GOX motor tested by Karabeyoglu [3-10] and from our previous numerical work [3-11].

The result obtained is as shown below in Fig. 3.7. It is observed that the system is unstable, however, the equation results in an unbounded growth of regression rate. This may be a result of using a steady state approximation of the transfer of heat into the solid fuel. Our conclusion is that therefore it is not straightforward for the case of hybrid rocket motors, to derive an oscillatory equation of motion for the regression rate due to the complex nature of the problem.

This is the main reason why we would choose to utilize numerical modelling of the physics of the individual phenomenon inside the combustion chamber of the motor using a computational fluid dynamics model. The results obtained using the CFD models would be discussed in the upcoming chapters.

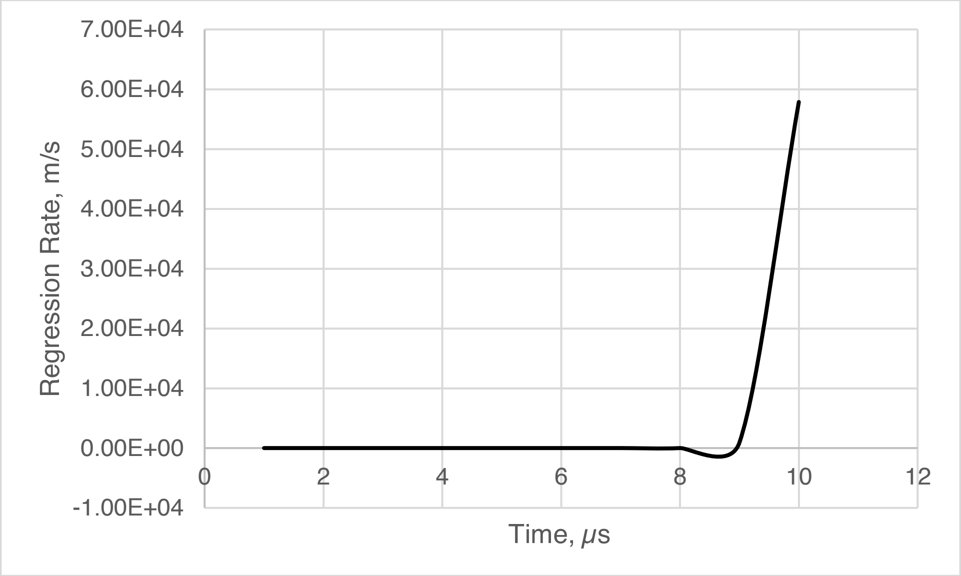

Fig. 3.7 Oscillatory regression with no thermal delay

3.6 Conclusion

In this chapter, a quantitative relation for the unsteady convective flux heat feedback from the flame to the regressing surface is derived. The concept of boundary layer delay is introduced, which is the delay experienced by the wall heat flux to the changes in the mass flux in the boundary layer. The concept of self-excited oscillations is introduced and it is shown that in the presence of a positive feedback due to time delay, the system can have ‘negative’ damping, which can render the system unstable. With an analogy to a simple non-linear oscillator, it is also shown that the magnitude of the time delay can affect the non-linear characteristics of the system.

Finally, an attempt is made to model the hybrid rocket intrinsic combustion instability analytically. The results show an unstable system. However, it is concluded that it is not straightforward to derive the oscillatory regression rate equation due to the requirement of the non-steady form of the thermal gradient at the burning solid surface – which is not available analytically for the hybrid rocket boundary condition of thermal conduction on a moving regressing surface. Therefore, to proceed, this problem is it is decided that this problem is best tackled using a numerical approach with computational fluid dynamics.

3.7 References for Chapter 3

[3-1] Marxman, G. and Gilbert, M., 1963, January. Turbulent boundary layer combustion in the hybrid rocket. In Symposium (International) on Combustion (Vol. 9, No. 1, pp. 371-383). Elsevier.

[3-2] Karabeyoglu, M.A. and Altman, D., 1999. Dynamic modeling of hybrid rocket combustion. Journal of Propulsion and Power, 15(4), pp.562-571.

[3-3] Marxman, G.A., 1965, January. Combustion in the turbulent boundary layer on a vaporizing surface. In Symposium (International) on Combustion (Vol. 10, No. 1, pp. 1337-1349). Elsevier.

[3-4] Lees, L., 1958, March. Convective heat transfer with mass addition and chemical reactions. In Combustion and Propulsion, Third AGARD Colloquium (pp. 451-498). Pergamon Press, New York.

[3-5] Karabeyoglu, A., 2007. Combustion instability and transient behavior in hybrid rocket motors. Progress in Astronautics and Aeronautics, 218, p.351.

[3-6] Culick, F.E.C., 1988. Combustion instabilities in liquid-fuelled propulsion systems.

[3-7] Zielke, W., Wylie, E.B. and Keller, R.B., 1969. Forced and self-excited oscillations in propellant lines. Journal of Basic Engineering, 91(4), pp.671-677.

[3-8] Dowling, A.P., 1997. Nonlinear self-excited oscillations of a ducted flame. Journal of fluid mechanics, 346, pp.271-290.

[3-9] Jenkins, A., 2013. Self-oscillation. Physics Reports, 525(2), pp.167-222.

[3-10] Karabeyoglu, A., Cantwell, B. and Stevens, J., 2005, July. Evaluation of the Homologous Series of Normal Alkanes as Hybrid Rocket Fuels. In 41st AIAA/ASME/SAE/ASEE Joint Propulsion Conference & Exhibit (p. 3908).

[3-11] Karthikeyan, G. and Shimada, T., 2018. Numerical Parametric Analysis of Combustion Instability in Axial-Injected Hybrid Rocket Motors. Journal of Propulsion and Power, 34(6), pp.1542-1552.

CHAPTER – 4

NUMERICAL MODELING OF INTERNAL BALLISTICS

As explained in the previous chapter, in order to understand the transient behaviour in hybrids and study the intrinsic combustion instability phenomenon, a numerical approach using CFD is one of the best ways to conduct the study.

The numerical modelling methodology would be explained in this chapter along with a validation of the numerical model with experimental data for the prediction of the steady state regression rates.

4.1 Introduction to the Numerical Modelling

Axial-injected hybrid rocket motors is computationally modelled. The overall numerical model is divided into sub-models for the ease of construction and verification. Each individual model is then coupled with each other resulting in the overall model.

The following are the sub-models which are used:

i. Gas Dynamics Model - For simulation of the flow-field inside the hybrid rocket combustion chamber and nozzle.

ii. Combustion Model - For simulation of the combustion occurring between the oxidizer from the inlet and the fuel which is injected into the combustion chamber from the solid surface regressing surface. This model is further divided into two:

   a. Heat Feedback Model - For simulation of heat input into the solid surface as a result of combustion.

   b. Chemical equilibrium Model - For the simulation of the combustion characteristics such as species composition, temperature and pressure in the mean flow and in the flame region.

iii. Thermal Conduction Model - For simulation of thermal energy flow into the solid fuel.

Each of the model would be further discussed in the following sub-sections of the chapter. The domain of each model in the hybrid rocket is highlighted in Fig. 4.1.

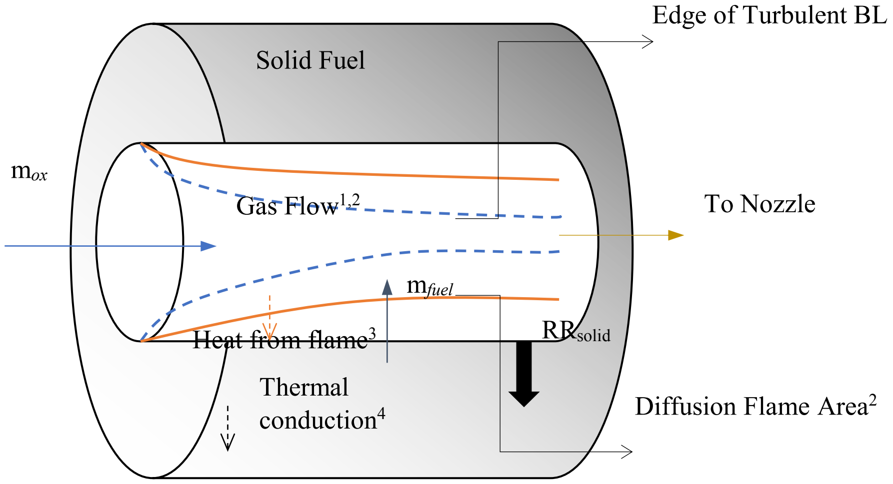

Fig. 4.1 Schematic of the HR combustion chamber showing the different regions of calculation and the sub-models associated

The superscripts denote the following: 1. Gas dynamics model 2. Chemical equilibrium model 3. Heat feedback model 4. Thermal conduction model

4.2 Gas Dynamics Model

Hybrid rocket combustion flow-fields involve complex fluid dynamics coupled with combustion, turbulence, radiation, spray atomization and vaporization in the case of liquid-phase oxidizer or liquefying fuels and fuel surface pyrolysis. However, for the sake of simplicity the following assumptions are made while constructing the numerical model:

i. Turbulence is not modelled explicitly. The effect of turbulence on the heat transfer to the fuel surface is implicitly present with the help of heat feedback model (see Section. 4.3).

ii. Effect of radiation is assumed to be negligible. Section 3.2 explains why this assumption can be valid.

iii. Atomization process is not considered since the oxidizer is assumed to be present in the gaseous phase.

iv. The fuel is assumed to vaporize directly from the solid phase into gaseous phase. Any liquid melt layer, if present is assumed to be of infinitely thin width.

v. The gases present are always assumed to behave as ideal gases under all operating conditions.

vi. The final product of the pyrolysis is assumed to be only the monomer of the polymeric fuel considered. This monomer is assumed to be only in gaseous phase.

vii. The velocity of all chemical species is assumed to be constant. Instantaneous chemistry (chemical equilibrium) is assumed. See Section 4.3.

viii. The flame is modelled as a sheet with different properties at different axial locations. The flame thickness is assumed to be negligible.

ix. Short nozzle is considered in adherence with the short nozzle theory. No nozzle throat erosion is considered.

4.2.1 Governing Equations

Under these assumptions, it is reasonably valid to model the gas dynamics flow-field part using a Quasi - 1 Dimensional (Q1D) Euler equations solver. The dimension is along the axial direction and 'quasi' because of the ability to accommodate the change in area. In Q1D model, the representative values of physical quantities are area-averaged values and only changes along the axial direction are captured. The flow field is modelled using compressible Euler equations along with the conservation of the mixture fraction, which determines the relative quantities of fuel and oxidizer in the mainstream. The external source addition from the solid fuel surface is modelled as another source term. The equations used for modelling are described below.

$$\frac{\partial A\boldsymbol{Q}}{\partial t}+\frac{\partial A\boldsymbol{F}}{\partial x}=\boldsymbol{S}_{Q1D}+\ \boldsymbol{S}_{MASS} \tag{4.2.1}$$

$$\boldsymbol{Q}=(\rho\ \ \rho u\ \ \rho e_t\ \ \rho\varepsilon\,)^t \tag{4.2.2}$$

$$\boldsymbol{F}=\ (\rho u\ \ \rho u^2+p\ \ (\rho e_t\ +p)u\ \ \rho\varepsilon u)^{\boldsymbol{t}} \tag{4.2.3}$$

$$\boldsymbol{S}_{Q1D}=(\,0\ \ \frac{pdA}{dx}\ \ 0\ 0\,)^t \tag{4.2.4}$$

$$\boldsymbol{S}_{MASS} = (\dot{m}_F l_p \;\; 0 \;\; \dot{m}_F l_p h_w \;\; \dot{m}_F l_p\,)^t \tag{4.2.5}$$

The mixture fraction, ε is defined as follows,

$$\varepsilon = \frac{b_C - b_{C,2}}{b_{C,1} - b_{C,2}} \tag{4.2.6}$$

where b_C is the mole number of atomic element C (Carbon) per unit mass of mixture gas and 1,2 represents the fuel and oxidizer stream respectively. When defined this way, it essentially results in a conserved quantity which can be transported across the fluid flow. This is because, in our model limitation is placed on the model for the consideration of the choice of oxidizer. Only those oxidizers are considered whose chemical composition do not possess 'Carbon' element. This means that, any value of C present should come only from the fuel. Therefore, by tracking this along the axial port of the combustion chamber, the ratio of the fuel and oxidizer can be estimated.

Specific total energy of the mixture gas, e_t is defined as follows,

$$e_t = e + \frac{u^2}{2} \tag{4.2.7}$$

Specific internal energy, *e* is defined as,

$$e = \textstyle\sum_i h_i Y_i - \frac{p}{\rho} \tag{4.2.8}$$

Here, *i* is species and varies from *i=1 to N*, where N is the total number of chemical species present in the system.

Enthalpy of reactant *i*, h_i, is expressed as,

$$h_i = \Delta h_i^0 + \int_{T_r}^{T} c_{p,i} dT \tag{4.2.9}$$

The specific heat at constant pressure for each reactant, $c_{p,\,i}$ is a function of temperature. This is obtained by fitting the JANAF's table data as a polynomial based on NASA CEA database [4-1], of the form,

$$\frac{C_{p,i}}{R_u/w_i} = a_{i,1}T^{-2} + a_{i,2}T^{-1} + a_{i,3} + a_{i,4}T + a_{i,5}T^2 + a_{i,6}T^3 + a_{i,7}T^4 \tag{4.2.10}$$

$$\frac{h_i}{R_u/w_i} = -a_{i,1}T^{-2} + a_{i,2}T^{-1}lnT + a_{i,3} + a_{i,4}\left(\frac{T}{2}\right) + a_{i,5}\left(\frac{T^2}{3}\right) + a_{i,6}\left(\frac{T^3}{4}\right) + a_{i,7}\left(\frac{T^4}{5}\right) + \frac{b_{i,1}}{T} \quad (4.2.11)$$

This results in the equation of ideal gas which closes the above equation set as,

$$p = \sum_i \frac{Y_i}{w_i}\rho R_u T \quad (4.2.12)$$

The above equations, 4.2.1 to 4.2.12 are then solved numerically at each time step in order to obtain the internal ballistics of the rocket motor.

4.2.2 Gas Dynamics Model Domain Definition

The domain modelled is as shown in Fig. 4.2. It consists of a combustion chamber of constant area and a convergent-divergent nozzle of variable area. The length of the combustion chamber varies for each of the test conducted and the length of the nozzle is fixed as 10% of that of the length of the combustion chamber. The grid size is assumed to be uniform throughout both the combustion chamber and the nozzle and the number of grid points is fixed to be either 301/201 or 61/41 configuration (depending on the necessity) for combustion chamber/nozzle system. The results of a grid sensitivity test would be shown later in the Chapter.

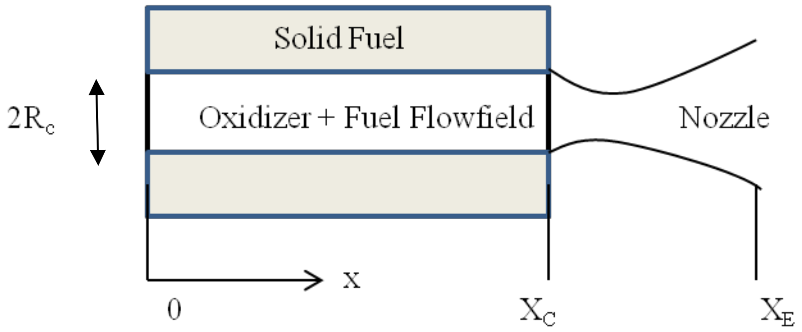

Fig. 4.2 Domain for Gas-Dynamics Model

The radius of the combustion chamber is as per specification based on required motor specification, and the radius of the nozzle is given based on a custom second order polynomial using the following formula,

$$r(x) = R_T - \frac{R_C - R_T}{(x_C - x_T)^4}(x - x_T)^4 + \frac{2(R_C - R_T)}{(x_C - x_T)^2}(x - x_T)^2 \qquad (4.2.13)$$

4.2.3 Boundary Conditions

Subsonic inlet boundary conditions are applied to the head end of the combustion chamber and the supersonic outlet boundary conditions are applied to the end of the nozzle. For subsonic inlet conditions, two external characteristic flow variables should be provided and one variable should be interpolated from inside the calculation domain. In our case, *(ρ and u)* – inlet mass flow rate is specified while pressure, p is interpolated from the flow domain. This essentially results in fixing the inlet entropy at the boundary condition.

The subsonic inlet conditions are as mentioned in Table 4.1. The outlet conditions are supersonic conditions, in which the values of all the variables required are interpolated (zeroth order) from inside the domain.

Table 4.1 Subsonic inflow conditions

Quantity	**Value**
Mass Flow Rate	As per conditions required
Pressure	Zeroth-order interpolation from inside the domain – results in a specular wall for pressure waves / or Externally Given
Temperature of Injection	300 [K] – Assumption because of GOX oxidizer / or Interpolated
Mixture Fraction	0 [-]

4.2.4 Numerical Solution

The equations 4.2.1 to 4.2.12 are to be solved numerically in order to obtain the flow field characteristics. In this section, the numerical method used to do so, is explained.

Discretization of the governing equations

The discretization of equation 4.1 is carried out using a finite volume method. Therefore, the domain is assumed to be divided into numerous elements of volumes, called cells, each with a unique notation, *i*. Upon integration on both sides of any cell, *i*, at the cell boundaries, $x_{i-1/2}$ and $x_{i+1/2} = x_{i-1/2} + \Delta x_i$, where Δx_i is the cell width, results in the following form of equation.

$$\int_{\mathrm{xi}-1/2}^{\mathrm{xi}+1/2} \left(\frac{\partial AQ}{\partial t} + \frac{\partial AF}{\partial x}\right) dx = \int_{\mathrm{xi}-1/2}^{\mathrm{xi}+1/2} \left(S_{Q1D} + S_{MASS}\right) dx \tag{4.2.14}$$

Now, the average amount of quantity in the cell, *i,* is defined as follows,

$$\bar{Q}_i \equiv \frac{\int_{\mathrm{xi}-1/2}^{\mathrm{xi}+1/2} Q dx}{\int_{\mathrm{xi}-1/2}^{\mathrm{xi}+1/2} dx} = \frac{\int_{\mathrm{xi}-1/2}^{\mathrm{xi}+1/2} Q dx}{\Delta x_i} \tag{4.2.15}$$

$$\bar{S}_{Q1D,i} \equiv \frac{\int_{\mathrm{xi}-1/2}^{\mathrm{xi}+1/2} S_{Q1D} dx}{\int_{\mathrm{xi}-1/2}^{\mathrm{xi}+1/2} dx} = \frac{\int_{\mathrm{xi}-1/2}^{\mathrm{xi}+1/2} S_{Q1D} dx}{\Delta x_i} \tag{4.2.16}$$

$$\bar{S}_{MASS,i} \equiv \frac{\int_{\mathrm{xi}-1/2}^{\mathrm{xi}+1/2} S_{MASS} dx}{\int_{\mathrm{xi}-1/2}^{\mathrm{xi}+1/2} dx} = \frac{\int_{\mathrm{xi}-1/2}^{\mathrm{xi}+1/2} S_{MASS} dx}{\Delta x_i} \tag{4.2.17}$$

Using this averaged amount, the following can be expressed,

$$\frac{d\bar{Q}_i}{dt}\Delta x_i + \mathrm{F}_{\mathrm{i}+1/2} - \mathrm{F}_{\mathrm{i}-1/2} = \bar{S}_{Q1D,i}\Delta x_i + \bar{S}_{MASS,i}\Delta x_i \tag{4.2.18}$$

Upon re-organization,

$$\frac{d\bar{Q}_i}{dt}\Delta x_i + \frac{\mathrm{F}_{\mathrm{i}+1/2} - \mathrm{F}_{\mathrm{i}-1/2}}{\Delta x_i} = \bar{S}_{Q1D,i} + \bar{S}_{MASS,i} \tag{4.2.19}$$

Now, integrating the equation 3.2.16 on both sides from time *t = nΔt* to *t=(n+1) Δt*,

$$\int_{n\Delta t}^{(n+1)\Delta t} \frac{d\bar{Q}_i}{dt} dt = \int_{n\Delta t}^{(n+1)\Delta t} \left(\frac{\mathrm{F}_{\mathrm{i}-1/2} - \mathrm{F}_{\mathrm{i}+1/2}}{\Delta x_i} + \bar{S}_{Q1D,i} + \bar{S}_{MASS,i} \right) dt \tag{4.2.20}$$

$$\bar{Q}_i^{\,\mathrm{n}+1} - \bar{Q}_i^{\,\mathrm{n}} = \int_{n\Delta t}^{(n+1)\Delta t} \left(\frac{\mathrm{F}_{\mathrm{i}-1/2} - \mathrm{F}_{\mathrm{i}+1/2}}{\Delta x_i} + \bar{S}_{Q1D,i} + \bar{S}_{MASS,i} \right) dt \tag{4.2.21}$$

Upon the execution of an explicit time stepping method, the following can be obtained,

$$\bar{Q}_i^{\,\mathrm{n}+1} - \bar{Q}_i^{\,\mathrm{n}} = \frac{\Delta t}{\Delta x_i} \left(F_{i-1/2}^{n} - F_{i+1/2}^{n} \right) + \Delta t \left(\bar{S}_{Q1D,i}{}^{n} + \bar{S}_{MASS,i}{}^{n} \right) \tag{4.2.22}$$

Hence, the conserved variable required at the next time step can be obtained once the flux variable and the source terms at the current time step are known.

$$\bar{Q}_i^{\,\mathrm{n}+1} = \bar{Q}_i^{\,\mathrm{n}} + \frac{\Delta t}{\Delta x_i} \left(F_{i-1/2}^{n} - F_{i+1/2}^{n} \right) + \Delta t \left(\bar{S}_{Q1D,i}{}^{n} + \bar{S}_{MASS,i}{}^{n} \right) \tag{4.2.23}$$

To be noted that this is the simplest type of time stepping, and is called the First order Euler method because of the first order accuracy in time. This means that errors in temporal domain are of the order of 2.

4.2.5 Evaluation of Discretised Flux

The flux splitting has been carried out using the AUSMDV [4-2] scheme. This scheme has been found to have properties of accurate and robust resolution for shock and contact discontinuities, computational simplicity and a similar extension to any general conservation laws like that of chemically reacting flows. A brief explanation of the model is presented here.

Splitting the Flux F, into mass flux and pressure flux as,

$$F = \begin{pmatrix} \rho u \\ \rho u^2 + p \\ (\rho e_t + p)u \end{pmatrix} = \rho u \begin{pmatrix} 1 \\ u \\ \left(e_t + \dfrac{p}{\rho}\right) \end{pmatrix} + \begin{pmatrix} 0 \\ p \\ p \end{pmatrix} = \rho u \psi + P \tag{4.2.24}$$

The velocity splitting is carried out as,

$$u_L^+ = \begin{cases} \alpha_L \left(\dfrac{(u_L + a_m)^2}{4a_m} - \dfrac{u_L + |u_L|}{2}\right) + \dfrac{u_L + |u_L|}{2} & if \ \dfrac{|u_L|}{a_m} \leq 1 \\ \dfrac{u_L + |u_L|}{2} & otherwise \end{cases} \tag{4.2.25}$$

$$u_R^- = \begin{cases} \alpha_R \left(\dfrac{(u_R + a_m)^2}{4a_m} - \dfrac{u_R + |u_R|}{2}\right) + \dfrac{u_R + |u_R|}{2} & if \ \dfrac{|u_R|}{a_m} \leq 1 \\ \dfrac{u_R + |u_R|}{2} & otherwise \end{cases} \tag{4.2.26}$$

$$\alpha_L = \frac{2\left(\frac{\mathrm{p}}{\rho}\right)_{\mathrm{L}}}{\left(\frac{\mathrm{p}}{\rho}\right)_{\mathrm{L}} + \left(\frac{\mathrm{p}}{\rho}\right)_{\mathrm{R}}}, \qquad \alpha_R = \frac{2\left(\frac{\mathrm{p}}{\rho}\right)_{\mathrm{R}}}{\left(\frac{\mathrm{p}}{\rho}\right)_{\mathrm{L}} + \left(\frac{\mathrm{p}}{\rho}\right)_{\mathrm{R}}} \tag{4.2.27}$$

$$a_m = \max(\alpha_L, \alpha_R) \tag{4.2.28}$$

In the above equations, *a* represents the speed of sound in the cell, and *L* and *R* represent the left and right boundaries of the cell. Using, the above equations, now the mass flux can be defined as,

$$(\rho u)_{1/2} = u_L^+ \rho_L + u_R^- \rho_R \tag{4.2.29}$$

Now, the pressure splitting is carried out in order to define the pressure flux,

$$p_L^+ = \begin{cases} \dfrac{p_L}{4}\left(\left(\dfrac{u_L}{a_m}\right)^2 \left(2 - \dfrac{u_L}{a_m}\right)\right) & if \ \dfrac{|u_L|}{a_m} \leq 1 \\ p_L \dfrac{u_L + |u_L|}{2u_L} & otherwise \end{cases} \tag{4.2.30}$$

$$p_R^- = \begin{cases} \frac{p_R}{4}\left(\left(\frac{u_R}{a_m}\right)^2\left(2+\frac{u_R}{a_m}\right)\right) & if\ \frac{|u_R|}{a_m} \leq 1 \\ p_R\frac{u_R + |u_R|}{2u_R} & otherwise \end{cases} \tag{4.2.31}$$

Using the above equations, the numerical flux $F_{1/2}$ (not considering the second component), can be written as,

$$F_{1/2} = \frac{1}{2}\left[(\rho u)_{1/2}(\psi_L + \psi_R) - \left|(\rho u)_{1/2}\right|(\psi_R - \psi_L)\right] + P_{1/2} \tag{4.2.32}$$

The second component in the equation 3.2.22, $(F_{1/2})_2$ is now derived,

$$\left(F_{1/2}\right)_2 = (\rho u^2)_{1/2} + (P_{1/2})_2 \tag{4.2.33}$$

$$(\rho u^2)_{1/2} = \left(\frac{1}{2}+s\right)(\rho u^2)_{AUSMV} + \left(\frac{1}{2}-s\right)(\rho u^2)_{AUSMD} \tag{4.2.34}$$

$$(\rho u^2)_{AUSMV} = u_L^+(\rho u)_L + u_R^-(\rho u)_R \tag{4.2.35}$$

$$(\rho u^2)_{AUSMD} = \frac{1}{2}\left[(\rho u)_{\frac{1}{2}}(u_L + u_R) - \left|(\rho u)_{\frac{1}{2}}\right|(u_R - u_L)\right] \tag{4.2.36}$$

Here, *s* is the switching function of the pressure gradient between AUSMD and AUSMV splitting and is defined as,

$$s = \frac{1}{2}\min\left(1, \mathrm{K}\frac{|p_R - p_L|}{\min(p_R, p_R)}\right) \tag{4.2.37}$$

Hence, as seen AUSMDV scheme is a combination of both AUSMD and AUSMV schemes. The averaging gives more preference to the AUSMV in order to make use of its superior shock capturing ability. In our method, the value of K is taken as 10.

4.2.6 Higher Order Spatial Accuracy

In order to achieve higher spatial accuracy, the cell centre (cell-averaged) values of the conservative variables can be modified at the boundaries. This approach is called the Variable Extrapolation approach or simply MUSCL which expands to Monotone Upstream-centered Scheme for Conservation Laws. For the first order method, it is assumed that any conserved variable, w_i is represented by an integral average in cell $I_i = [\, x_{i-1/2},\ x_{+1/2}]$ as represented by equation 4.2.15.

As a first step in achieving higher order, the following piece-wise linear, local reconstruction of w_i can be constructed as shown in Fig. 3.3,

$$w_i(\mathrm{x}) = w_i(0) + \frac{(x - x_i)}{\Delta x}\Delta_i, \quad x \in [0, \Delta x] \tag{4.2.38}$$

where Δ_i/Δ_x is a slope which is chosen accordingly in cell I_i. Here, the values of $w_i(\mathrm{x})$ at the left and right boundaries of the cell as defined by superscript L and R, are given by,

$$w_{i+1/2}{}^{L} = w_i(0) - \frac{1}{2}\Delta_i, \quad w_{i-1/2}{}^{R} = w_i(0) + \frac{1}{2}\Delta_i \tag{4.2.39}$$

It is to be noted that the integral of $w_i(\mathrm{x})$ in the cell is same as that of w_i and hence the reconstruction process preserves the conservation.

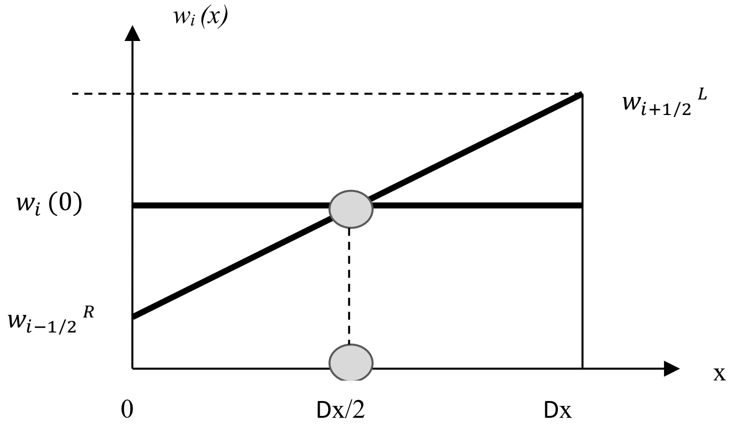

Fig. 4.3 Piece-wise linear MUSCL reconstruction of data

In general, for even higher accuracies, the following reconstructions are used,

$$w_{i+1/2}{}^{L} = w_i(0) + \frac{1}{4}[(1-k)\nabla w_i + (1+k)\Delta w_i] \tag{4.2.40}$$

$$w_{i-1/2}{}^{R} = w_i(0) + \frac{1}{4}[(1+k)\nabla w_i + (1-k)\Delta w_i] \tag{4.2.41}$$

$$\nabla w_i = w_i - w_{i-1} \tag{4.2.42}$$

$$\Delta w_i = w_{i+1} - w_i \tag{4.2.43}$$

In the equations, 4.2.40 and 4.2.41, k is the parameter which controls the spatial accuracy. The value of -1 for k results in the spatial accuracy of second order, and value of -1/3 results in the accuracy of third order.

However, this kind of reconstruction results in spurious oscillations in the vicinity of high gradients, which will be eliminated by the introduction of a flux slope limiter and which will result in making the scheme, Total Variational Diminishing (TVD). The limiters are constructed as defined below,

$$w_{i+1/2}{}^{L,lim} = w_i + \frac{1}{2}\delta w_{lim} \tag{4.2.44}$$

$$w_{i-1/2}{}^{R,lim} = w_i - \frac{1}{2}\delta w_{lim} \tag{4.2.45}$$

$$\delta w_{lim} = \frac{1}{2}\{sgn(\delta w_{lim}{}^{R}) + sgn(\delta w_{lim}{}^{L})\}\min(|\delta w_{lim}{}^{R}|, |\delta w_{lim}{}^{L}|) \tag{4.2.46}$$

$$\delta w_{lim}{}^{L} = R^{L}(\theta)\delta w^{L} \tag{4.2.47}$$

$$\delta w_{lim}{}^{R} = R^{R}(\theta)\delta w^{R} \tag{4.2.48}$$

$$\theta = \frac{\Delta w_i}{\nabla w_i} \tag{4.2.49}$$

$$\delta w^L = \frac{1}{2}[(1-k)\nabla w_i + (1+k)\Delta w_i] \tag{4.2.50}$$

$$\delta w^R = \frac{1}{2}[(1+k)\nabla w_i + (1-k)\Delta w_i] \tag{4.2.51}$$

Here, $R^R(\theta)$ and $R^L(\theta)$ are the slope limiters and they follow the following conditions,

i. If w_{i-1}, w_i, w_{i+1}, do not increase (or decrease) monotonically, then ($\theta < 0$) and hence, , $R^R(\theta)$ and $R^L(\theta)$ take the value 0.

ii. If w_{i-1}, w_i, w_{i+1}, increase monotonically, then $w_{i-1} \le w_i - \frac{1}{2}\delta {w_{lim}}^R \le w_i$ and $w_i \le w_i + \frac{1}{2}\delta {w_{lim}}^L \le w_{i+1}$.

iii. If w_{i-1}, w_i, w_{i+1}, decrease monotonically, then $w_{i-1} \ge w_i - \frac{1}{2}\delta {w_{lim}}^R \ge w_i$ and $w_i \ge w_i + \frac{1}{2}\delta {w_{lim}}^L \ge w_{i+1}$.

iv. If $\nabla w_i = 0$ and $\Delta w_i \ne 0$ (i.e. $\theta \to \infty$), then $R^R(\theta) = 0$ and $0 \le R^L(\theta) \le \frac{4}{1+k}$.

v. If $\nabla w_i \ne 0$ and $\Delta w_i = 0$ (i.e. $\theta = 0$), then $R^L(\theta) = 0$ and $0 \le R^R(\theta) \le \frac{4}{1+k}$.

From condition ii, the following can be derived,

$$w_{i-1} \le w_i - \frac{1}{2}\delta {w_{lim}}^R \le w_i$$

$$-\nabla w_i \le w_i - \frac{1}{2}\delta {w_{lim}}^R \le 0$$

$$-\nabla w_i \le w_i - \frac{1}{2}R^R(\theta)\delta w^R \le 0$$

$$2\nabla w_i \ge R^R(\theta)\delta w^R \ge 0$$

$$\frac{2\nabla w_i}{\delta w^R} \geq R^R(\theta) \geq 0 \quad [\,\delta w^R > 0\,]$$

$$\frac{2\nabla w_i}{\frac{1}{2}[(1+k)\nabla w_i + (1-k)\Delta w_i]} \geq R^R(\theta) \geq 0$$

$$\frac{4}{[(1+k)+(1-k)]\theta} \geq R^R(\theta) \geq 0$$

In the same manner, from condition ii, the following relation for limiter, $R^L(\theta)$ can be obtained,

$$0 \leq R^L(\theta) \leq \frac{4\theta}{[(1-k)+(1+k)]\theta}$$

Condition iii is same as condition, ii, and then taking the other conditions into consideration, the following finalized equations for limiters can be obtained,

$$0 \leq R^L(\theta) \leq min\left(\frac{4\theta}{[(1-k)+(1+k)]\theta}, \quad 1\right) \tag{4.2.52}$$

$$0 \leq R^R(\theta) \leq min\left(\frac{4}{[(1+k)+(1-k)]\theta}, \quad 1\right) \tag{4.2.53}$$

4.2 7. Higher Order Temporal Accuracy

In our calculations, for the transient analysis of hybrid rocket, time accuracy is of high importance. Hence, in order to achieve a higher temporal accuracy, a fourth order Runge Kutta method, (the so called ‘Classic Runge Kutta Method’) is applied as given below,

$$\bar{Q}_i^{(1)} = \bar{Q}_i^{\,\mathrm{n}} + \frac{\Delta t}{\Delta x_i}\left(F^n_{i-1/2} - F^n_{i+1/2}\right) + \Delta t\left(\bar{S}_{Q1D,i}{}^{n} + \bar{S}_{MASS,i}{}^{n}\right) \tag{4.2.54}$$

$$\bar{Q}_i^{(2)} = \frac{1}{2}\left\{\bar{Q}_1^{\,\mathrm{n}} + \frac{\frac{\Delta t}{2}}{\Delta x_i}\left(F^n_{i-\frac{1}{2}} - F^n_{i+\frac{1}{2}}\right) + \frac{\Delta t}{2}\left(\bar{S}_{Q1D,i}{}^{n} + \bar{S}_{MASS,i}{}^{n}\right)\right\} \tag{4.2.55}$$

$$\bar{Q}_i^{(3)} = \frac{1}{2}\left\{\bar{Q}_1^{\,\mathrm{n}} + \frac{\frac{\Delta t}{2}}{\Delta x_i}\left(F^n_{i-\frac{1}{2}} - F^n_{i+\frac{1}{2}}\right) + \frac{\Delta t}{2}\left(\bar{S}_{Q1D,i}{}^{n} + \bar{S}_{MASS,i}{}^{n}\right)\right\} \tag{4.2.56}$$

$$\bar{Q}_i^{(4)} = \left\{\bar{Q}_1^{\,\mathrm{n}} + \frac{\Delta t}{\Delta x_i}\left(F^n_{i-\frac{1}{2}} - F^n_{i+\frac{1}{2}}\right) + \Delta t\left(\bar{S}_{Q1D,i}{}^{n} + \bar{S}_{MASS,i}{}^{n}\right)\right\} \tag{4.2.57}$$

$$\bar{Q}_i^{\,\mathrm{n+1}} = \frac{1}{6}\left\{\bar{Q}_i^{(1)} + 2\bar{Q}_i^{(2)} + 2\bar{Q}_i^{(3)} + \bar{Q}_i^{(4)}\right\} \tag{4.2.58}$$

In the above equations, the value of Δt, is obtained as follows,

$$\Delta t_i = CFL\frac{\Delta x_i}{|u_i| + a_i} \tag{4.2.59}$$

As seen, the time step, Δt_i here is defined for each cell. This is referred to as local-time stepping, in which each cell gets its own time step which scales with the maximum time step that ensures local stability. This will result in a uniform Courant number for all the cells. As a result of this method, the time-accuracy is lost, but time needed to march to the steady-state value is accelerated and it has been shown that it does not affect the steady state solutions [4-3].

Using such an approach is equivalent to preconditioning the residual by a scalar. The preconditions remove the stiffness associated with the spatial variations in the largest characteristic speed and in cell size. However, to be noted is that, when time accurate solutions are required, such as in instability analysis, we use a global time stepping method, in which Δt_i is replaced by a single value of Δt. CFL here is the Courant-Friedrichs-Lewy number which is taken as 0.3 in our calculations.

4.2.8 Energy Balance Equation

Upon closer inspection of the equation 4.2.1, it is clear that for solving the equation and marching in time, it requires the cognizance of the value of $\dot{m}_f$, which is the mass addition of the gasified fuel from the regressing surface. This parameter needs to be known at each current time step. In order to obtain this equation, the energy balance equation at the surface of the solid fuel needs to be solved. The equation is as described below (as previously explained in Section 3.1),

$$\lambda_s \left(\frac{\partial T}{\partial y}\right)_{y=-0} = \lambda_g \left(\frac{\partial T}{\partial y}\right)_{y=+0} - \rho_s \dot{r} h_v \tag{4.2.60}$$

In this equation, y is the location normal to the solid fuel surface. The solid fuel surface is at $y=0$. The inside of the fuel is at $y < 0$. The left-hand side of the equation refers to the thermal conduction of the heat from the flame into the solid fuel, and will be modelled using the thermal conduction model which will be explained in Section 4.5. The first term on the right-hand side of the equation refers to the heat feedback from the flame region into the solid fuel. This will be modelled using an existing analytical model which will be explained in section 3.3. The second term on the right-hand side of the equation refers to the energy required for the solid fuel to vaporise.

When the above equation is solved using the models described above, the value of the solid fuel regression rate, $\dot{r}$ can be obtained, and through it, the value of $\dot{m}_f$ can be obtained since, $\dot{m}_f = \rho_s \dot{r}$.

The heat of gasification, h_v which includes the latent heat and the decomposition heat, is expressed as,

$$h_v = h_{monomer,g}\,(T_{sr}) - h_{polymer,f}\,(T_m) \tag{4.2.61}$$

The monomer here is only gas. It is evaluated fitting the values of temperature against the JANAF Data [15]. The evaluation of $h_{polymer,f}$ is carried out as below with the assumption of constant specific heat $c_{polymer,f}$ of the solid polymer,

$$h_{polymer,f} = \Delta h^0_{polymer} + c_{polymer,f}\,(T_{sr} - T_r) \tag{4.2.62}$$

4.2.9 Quasi-Steady State Approximation

In the combustion of a hybrid rocket, there are many characteristic times involved such as characteristic time for the mainstream gaseous flow, the time for thermal conduction and the time for combustion reactions. In order to analyse the regression rate and the internal ballistics of the hybrid rocket, it is necessary to define a 'steady' state at which the results are investigated, but in practical case, there is no true 'steady' state because due to the continuous vaporization of the fuel, the channel shape (port radius) is always changing, resulting in change in the flow characteristic continuously. However, it is assumed that the change in the shape is quasi-static with respect to the change of the interior of the flow field. In other words, at any given moment, the stationary solution of the flow field corresponds to the flow path shape at that time (converged solution). Hence, with this methodology, the radius of the port can be fixed in the calculations for the quasi-steady state for the given instantaneous configuration of the combustion chamber.

4.2.10 Convergence of the Steady State Solution

In order to determine if the flow-field inside the combustion chamber has reached the 'quasi' steady state defined above, the following residuals of pressure, total energy and temperature distribution inside the solid fuel are monitored. The residuals of pressure and total energy are described here. The residual of temperature distribution inside the fuel will be described in Section 4.5.4.

$$R_e \leq \varepsilon \text{ and } R_p \leq \varepsilon \tag{4.2.63}$$

$$R_e = \frac{\sqrt{\sum_{i=1}^{N_c}\left(e_{t,i}^{n+1} - e_{t,i}^{n}\right)^2}}{N_c} \tag{4.2.64}$$

$$R_p = \frac{\sqrt{\sum_{i=1}^{N_c}\left(p_{t,i}^{n+1} - p_{t,i}^{n}\right)^2}}{N_c} \tag{4.2.65}$$

In our calculations, the residual limit, ε is set to 1×10^{-6}.

This ends the discussion on the construction of the gas dynamics model.

4.3 Heat-Feedback Model

Due to the usage of Euler equations for laminar flow, the viscous effect is not modelled. As a natural corollary, the boundary layer is not modelled directly. This means that the transport of heat to the solid fuel surface is not modelled implicitly using the model. This warrants for the usage of an external model which can simulate this heat transfer. For this, an analytical model for the turbulent heat transfer is used.

4.3.1 Evaluation of Convective Heat Transfer

The model used has been proposed first by Marxman using the diffusion limited theory [4-4] and later modified by Karabeyoglu [4-5], the derivation of which was done in Chapter 3 and the same is expressed here in Eqn. 4.3.1. The expression shows that for a given propellant combination and at a position along the length of the fuel, the heat feedback is dependent on the total mass flux, *G* and regression rate $\dot{r}$. The dependence on the total mass flux is straight forward because at higher values of mass flux, more energy is released through combustion. The dependence on $\dot{r}$ is due to the blowing/blockage effect.

$$\lambda_g \left(\frac{\partial T}{\partial y}\right)_{y=+0} = \left[\frac{0.03\,q}{\mu^{-0.2}}\right]^{\frac{1}{(1-k)}} \left[\frac{B_t h_v'}{\rho_s^{\frac{k}{(1-k)}}}\right] x^{\frac{-0.2}{(1-k)}}\, G^{\frac{0.8}{(1-k)}}\, \dot{r}^{\frac{-k}{(1-k)}} \qquad (4.3.1)$$

The thermo chemical blowing parameter B_t is expressed as below,

$$B_t = \frac{u_e}{u_{fl}} \frac{h_{fl} - h_{Sr}}{h_{v'}} \qquad (4.3.2)$$

Here, $\mathrm{h}_{v'}$ is the total heat of gasification which includes not only the heat required for melting and vaporization (latent heat of vaporization) but also the heat required to raise the solid fuel temperature from the initial temperature to the fuel surface temperature.

For the ratio of the speeds at the edge of the boundary layer u_e and at the flame u_{fl}, the following formulation proposed by Marxman [4-4] is used,

$$\frac{u_e}{u_{fl}} = \frac{K_{ox} + \left(\frac{O}{F} + K_{ox}\right)\frac{h_{fl} - h_{sr}}{h'_v}}{\frac{O}{F}\,\frac{h_{fl} - h_{sr}}{h'_v}} \quad (4.3.3)$$

Since, the oxidizer is 100 % gaseous oxygen, the value of the oxidizer concentration in the oxidizer stream, K_{ox} is taken as 1. The value of O/F at the flame region is assumed to be as stoichiometric value.

In the above equation 4.3.3**,** the value of h_{fl} and h_{sr} are the specific enthalpies at the flame location and at the surface defined with respect to the base temperature T_r = 298.15 K. It is assumed that the composition of the gas at the fuel surface is 100 % fuel. Hence, the values are described as,

$$h_{fl} = h_P(T_{fl}) - h_P(T_r) \quad (4.3.4)$$

$$h_{sr} = h_F(T_S) - h_F(T_r) \quad (4.3.5)$$

The above specific enthalpies are expressed as function obtained by the JANAF table's data [8].

The constants q and k are related to the skin-friction coefficient. The ratio of skin-friction coefficient with/without surface blowing C_f/C_{f0} means the reduction in skin-friction caused by surface-blowing, which is called 'blocking effect'. Marxman expressed the ratio C_f/C_{f0} as a function of aerodynamic blowing parameter B_a, as discussed in Chapter 3. Here a power law fit is taken as the function form of the original equation as shown in Eqn. 3.7

$$\frac{C_f}{C_{f0}} = qB_a^{-k} \quad (4.3.6)$$

The parameters q and k in the equation are defined by the equation. In our study, the values are taken as q = 0.74 and k = 0.53, from the reduction of Eqn. 3.7 for the considered range of $1 < B_a < 15$.

4.4 Combustion Model - Chemical Equilibrium Calculation

4.4.1 Chemical Equilibrium Calculation

If the chemical equilibrium compositions of a chemical system are known a priori then the theoretical thermodynamic properties for the system can be calculated. For this, a model based on the NASA CEA [4-1] has been developed. Chemical equilibrium is usually described with the use of either equilibrium constants or the minimization of free energy. However, when using the approach of minimization of free energy, the species can be treated independently without the specification of the set of reactions they follow. The free energy that can be minimized can be either Gibbs free energy or the Helmholtz free energy.

In general, the combustion phenomenon involves many species and elementary reactions. However, from a computational cost point of view, it is difficult to simulate all the reactions and the species. Hence, in our model, for the combustion of a hydrocarbon, C_xH_y, only 9 species are considered - O_2, CO_2, H_2O, CO, H_2, OH, O, H and C_xH_y. This restriction is imposed by having as number of species with which the flame temperature obtained does not differ substantially from the flame temperature obtained when there is no restriction considered. This calculation is carried out using NASA CEA code.

Using this model, it is assumed that the fuel gas and the oxidizer are mixed and reacted instantly. The output of this model are the temperature and the chemical composition of the combustion gas, obtained after the chemical equilibrium calculation. The concept of the calculation [4-1] is based on the minimization of free energy by Lagrange's method of undetermined multipliers (LM) under the constraint conditions that the mole numbers of the atomic elements are conserved. The reader is encouraged to refer to [4-1] for a more detailed discussion on the solution methodology.

The mixture fraction as defined in equation 4.2.6 bears relation to the assigned number of mole numbers of atomic elements. Under the assumption that all the chemical species have the same velocity, the following relations can be derived,

$$b_C^0 = \frac{1}{14}\varepsilon \tag{4.4.1}$$

$$b_H^0 = \frac{1}{7}\varepsilon \tag{4.4.2}$$

$$b_O^0 = \frac{1}{16}(1-\varepsilon) \tag{4.4.3}$$

If the thermodynamic states are specified by the assignment of density and specific internal energy, then Helmholtz energy is used for the free energy minimization. If the assigned properties are pressure and specific enthalpy, then Gibbs energy is used for the free energy minimization.

The function minimized, *F* is as follows,

$$F = f + \sum_i LM_i(b_i - b_i^0) \tag{4.4.4}$$

The following are the two chemical equilibrium calculations executed in our combustion model.

4.4.2 Chemical composition in the Quasi -1-Dimensional flow field

For calculation of cross-sectional average temperature and cross-sectional average composition of Q1D flow field and the estimation of specific heat ratio and speed of sound, Helmholtz energy minimization is carried out. This is done due to the relative ease usage of choice of input variables for the minimization of Helmholtz energy – which is density and internal energy. Both these variables are the primitive variables obtained from conservation of density, momentum and total energy, used in the time marching of CFD calculations and therefore are readily available. Therefore, the choice of using Helmholtz energy minimization is mainly for the ease of calculation. It is estimated that the effect of usage of the alternate minimization would be relatively small even though a rigorous study on the same has not been carried out yet. This would our target in the future.

4.4.3 Chemical composition in the Flame Region

For calculation of the thermochemical blowing parameter, the thermochemical properties at the flame such as the flame temperature and chemical composition (and through that, the flame enthalpy) are required. In ideal cases, flame extinction may be caused by the absence of oxidizer or other reasons. However, in our model, it is assumed that the flame is always present at any axial location, x. In order to estimate the flame temperature and the chemical composition, the minimization of Gibbs free energy is carried out using the mixture fraction, pressure and the specific enthalpy. It is assumed that at the flame, the mixture fraction takes the stoichiometric value. The area mean pressure obtained from the output of equation 4.2.1 is used as input of pressure in this model. Even though the enthalpy at the flame is different compared to the area-averaged value, since it is difficult the calculate the enthalpy at the flame exactly, it is approximated by the usage of the area-averaged enthalpy of the Quasi - 1 Dimensional flowfield. The choice of using Gibbs energy minimization for the flame is due to the valid assumption that the combustion is a constant pressure process.

Solving these two sub-models, we obtain the parameters required as input into the heat-feedback model.

This ends the section on the chemical equilibrium calculations.

4.5 Thermal Conduction Model

This model is used to simulate the heat transfer into the solid fuel. It is necessary because as seen in the energy balance equation, the temperature gradient at the surface of the regressing fuel needs to be known in order to solve it. The modelling is done through a finite difference method. It is assumed that the heat transfer along the x-axis (port length) inside the solid fuel is negligible. It is also assumed that the outer end of the solid fuel is always kept at the initial wall temperature, T_{wall}.

4.5.1 Governing Equations

The one-dimensional thermal conduction equation, into the solid fuel (Fourier's law of heat conduction), which is solved with the co-ordinate, y fixed at the regressing surface, is given as,

$$\frac{\partial T}{\partial t} + \dot{r}\frac{\partial T}{\partial y} - \alpha_s \frac{\partial^2 T}{\partial y^2} = 0 \tag{4.5.1}$$

This equation is solved at each individual location, x along the axis. A schematic of the model is shown in Fig. 4.4.

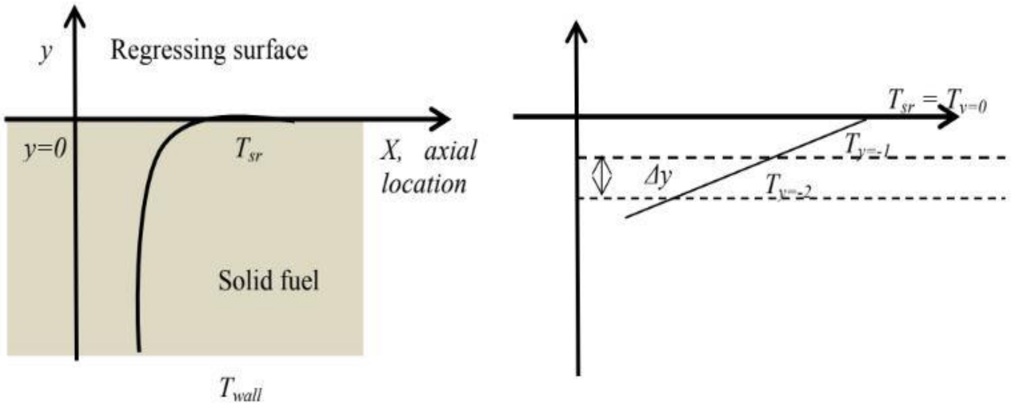

Fig. 4.4 Schematic of the thermal conduction model

The calculation of the thermal gradient at the surface, $y=-0$ for usage in Eqn. 4.2.60 is given as,

$$\lambda_s \left(\frac{\partial T}{\partial y}\right)_{y=-0} = \frac{\left(-3T_{sr} + 4T_{y=-1} - T_{y=-2}\right)}{2\Delta y}\lambda_f \tag{4.5.2}$$

There exists a closed form of analytical solution for Eqn. 4.5.1, which is the steady state solution for the equation and it is given by the following expression,

$$T(y) = T_{wall} + (T_{sr} - T_{wall})e^{\left(\frac{\dot{r}y}{\alpha_s}\right)} for - \infty \leq y \leq 0 \tag{4.5.3}$$

Therefore, for reaching steady state, the derivative of Eqn. 4.5.3 at *t=0* (Eqn. 4.5.4), can directly be used for evaluation of $\lambda_s \left(\frac{\partial T}{\partial y}\right)_{y=-0}$ instead of the form in the Eqn. 4.5.2.

$$\lambda_s \left(\frac{\partial T}{\partial y}\right)_{y=-0} = \lambda_s (T_{sr} - T_{wall}) \left(\frac{\dot{r}}{\alpha_s}\right) \tag{4.5.4}$$

4.5.2 Domain Definition

50 grid points (N_F) are used to model the inside of the solid fuel and the width of the solid fuel is taken as 0.1 m. The grid spacing is exponential with finer grid sizing towards the solid fuel grain in order to resolve the temperature gradient at the surface accurately. The actual conduction zone is much shorter and of the order of 2.5mm because of relatively short distance from the regressing fuel surface where the effect of thermal diffusion is felt. Hence, this approximation is valid.

4.5.3 Boundary Conditions

Dirichlet boundary conditions are applied to the domain with the surface temperature being T_{sr} and the wall temperature at y → -∞ as T_{wall}. The temperature at the surface is not known beforehand. It must be solved through the solution of the non-linear energy balance equation. For accelerated convergence, the initial condition is taken from the analytical profile obtained from equation 4.5.3.

4.5.4 Numerical Solution

A finite difference method is used to solve the Eqn. 4.5.1. It is assumed that the thermal conduction is only 1 Dimensional at each axial location of the port. The spatial derivatives in equation 4.5.1 are replaced by second-order central differencing approximations. This results in second order spatial accuracy with the error of the order of 3. Since, the aim is to generate long time marching solutions for studying the numerical instability, a first order type Euler Explicit scheme cannot be used. This is because,

1. Euler scheme introduces numerical diffusion because of its nature
2. The global error may be significant even with relatively very small time-steps.

Hence, a two stage Runge-Kutta method has been applied here, which results in the temporal accuracy of 2nd order. The scheme is made numerically stable by following the condition described below,

$$\Delta t = \frac{Stability\ criterion \text{ x } \Delta y^2}{\alpha_f} \tag{4.5.5}$$

Typical value of Δy and Δt are 1 x 10^{-5} and ≈ 5 x 10^{-4}. Here, the value of stability criterion must be less than or equal to 0.5. In our study, it is assumed as 0.4.

The residual for calculation of the steady state is defined as follows,

$$R_t = \frac{\sqrt{\sum_{j=1}^{N_F}\left(T_{t,j}^{n+1} - T_{j,i}^{n}\right)^2}}{N_F} \tag{4.5.6}$$

Here, R_t is the temperature residual and the solution are said to have reached the steady state when, R_t < 1 x 10^{-5}.

4.5.5 Pyrolysis rate of the fuel

It is known that the solutions of equations 4.3.1 and 4.5.2 are necessary to be given as input into the energy balance equation 4.2.60 in order to obtain the value of $\dot{m}_f$, which is again needed as input into equation 4.2.1, in order to march forward in time. However, upon inspection of the equation of convective heat flux - 4.3.1, it is seen that there are two unknowns in the equation which needs to be known for solving it - the surface temperature, T_s and the regression rate $\dot{r}$. In order to eliminate this constraint, one of the variables needs to be written as the function of the other. This is done by using the pyrolysis law for fuels.

Arrhenius-type equation is empirically used as pyrolysis rate equation 4.5.7,

$$\dot{r} = A_c exp\left(\frac{-E_a}{R_u T_s}\right) e_{reaction} \tag{4.5.7}$$

The list of parameters described above vary for different fuels and for our current case, the chosen fuel is High Density Polyethylene (HDPE). The parameters for the same are provided below in Table. 3.2. [20,21]

After reducing the equation 4.3.1 as a function of T_s alone, it is possible to solve the energy balance equation, 4.2.60 which is non-linear in T_s, by using an approximated iterative approach such as Newton-Raphson method, which results in obtaining the value of $\dot{m}_f$ as,

$$\dot{m}_f = \rho_S \dot{r} \tag{4.5.8}$$

The methodology of Newton-Raphson is as follows,

Rewrite equation 4.3.1 as a function of T_s alone.

$$f(T_s) = 0 \tag{4.5.9}$$

The value of the surface temperature at the next iterated step, T_s^{n+1} is given as a function of the current time step, T_s^n as,

$$T_S^{n+1} = T_S^n - \frac{f(T_s^n)}{f'(T_s^n)} \tag{4.5.10}$$

This process is iterated till the residue of the variable, err_{Ts}, as defined by the equation takes a value less than the limit, $\varepsilon = 1 \times 10^{-6}$.

$$err_{T_s} = \left| \frac{T_S^{n+1} - T_S^n}{T_S^{n+1}} \right| < \varepsilon \tag{4.5.11}$$

Table 4.2 Parameters in Arrhenius-type equation and solid fuel properties

Quantity	**Value**	**Unit**
Pre-exponential factor, A_c	2.0×10^{16}	(s^{-1})
Activation energy, E_a	1.5×10^{5}	J/mol
Degradation Zone Thickness, $e_{reaction}$	25	µm
Standard enthalpy of formation of HDPE, $\Delta h^0_{polymer}$	-1800	kJ/kg
Specific heat of HDPE, $c_{polymer}$	1300	J/(kg. K)
Melting Point, Tm	400	K
Reference Temperature T_r	298.15	K

4.6 Model Integration

4.6.1. Coupling of the Sub-Systems

Each of the individual sub-models - gas dynamics, combustion, thermal feedback and the thermal conduction models are now coupled with each other, enabling to march in time and get the required solutions.

The coupling process is as shown in Fig. 4.5.

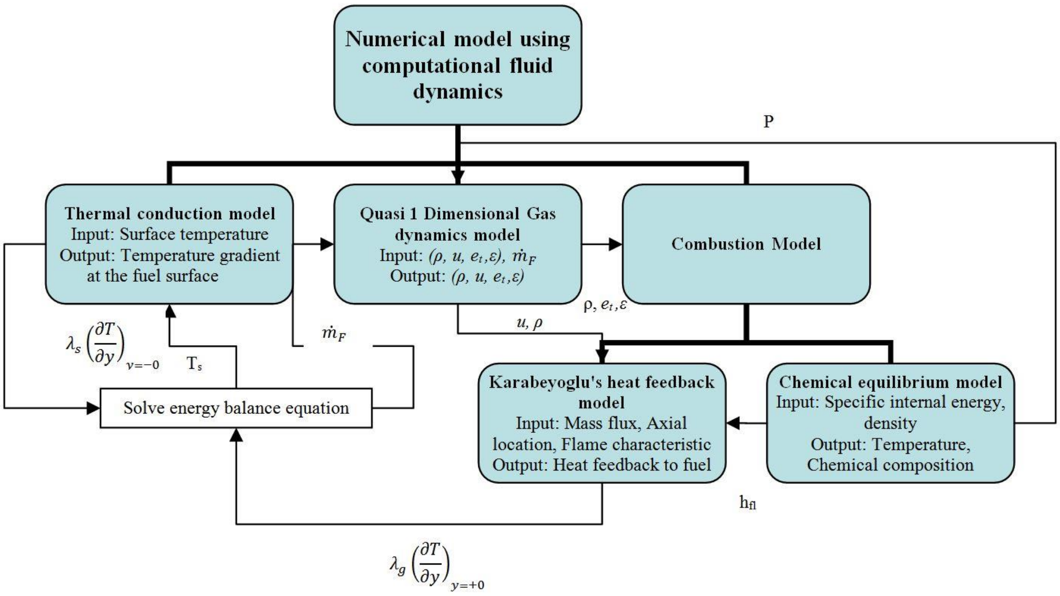

Fig. 4.5 Relationship between sub-models

4.6.2 Marching till Burn Time

Since, in our study, the average regression rates obtained are compared with experimental data, it is enough for us to simulate the combustion till the quasi-steady state, but till the burn time D_{time} corresponding to the experiments. This is done by calculating the regression rate of each quasi-steady state and then change the port shape with respect to the fuel retraction speed and re-calculate till next quasi-steady state. To be noted is that the process of nozzle erosion is not considered in this study, hence the throat diameter does not change over time. The above-mentioned process is repeated till the required burn time is achieved. Specific burn times for each experiment is different, and are specified in the results section. Fig. 4.6 shows the time-marching diagram for our methodology.

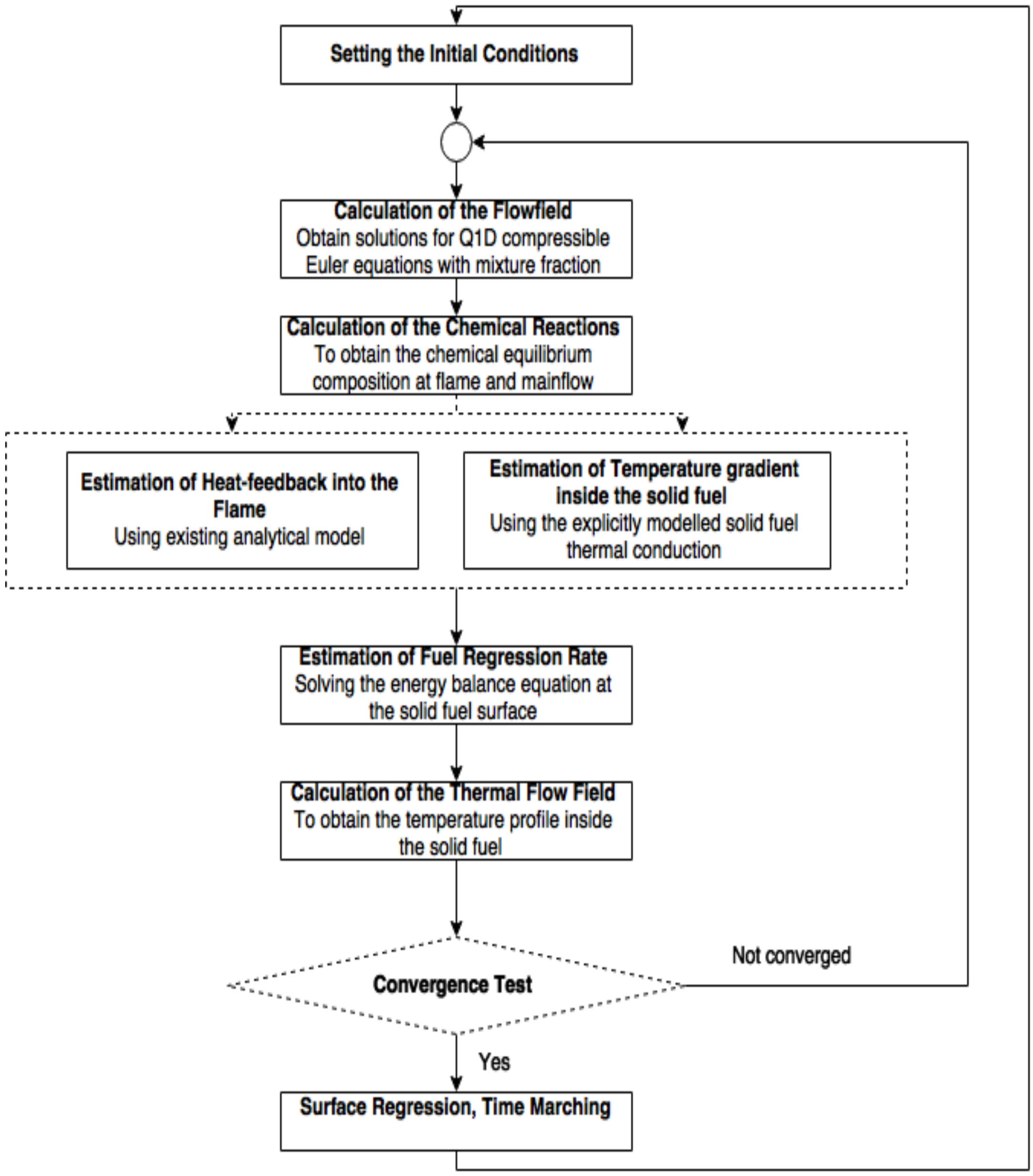

Fig. 4.6 Time marching flowchart

For unsteady transient analysis, the port area is considered fixed throughout, whereas the time marching continues without consideration of the residuals.

4.6.3 Averaging Method for Regression Rate

Once the calculation is completed for the required time, the time and space averaging of the regression rate and oxidizer flux are estimated using the port radius profile obtained at the end of the calculation,

$$\Delta m_F = \rho_S \int_0^{L_p} \pi\left(r_{final}^2 - r_{initial}^2\right) dx \tag{4.6.1}$$

$$\overline{r_{final}} = \sqrt{r_{initial}^2 + \frac{\Delta m_F}{\pi \rho_S L_p}} \tag{4.6.2}$$

$$\bar{\dot{r}} = \frac{\overline{\overline{r_{final}} - r_{initial}}}{t_b} \tag{4.6.3}$$

$$\overline{G_{OX}} = \frac{4\dot{m}_{ox}}{\pi\left(r_{initial} + \overline{r_{final}}\right)^2} \tag{4.6.4}$$

After obtaining several results, they are fit against the empirical expression as follows,

$$\bar{\dot{r}} = a\overline{G_{OX}}^n \tag{4.6.5}$$

In this expression, it is to be noted that the unit of $\bar{\dot{r}}$ is mm/s whereas the unit of $\overline{G_{OX}}$ is kg/ (m^2. s). The constants *a* and *n* are determined by least squares curve fit.

This finishes the discussion on the construction of the global numerical model for the temporal prediction of the regression rate and other internal ballistics of the hybrid rocket system.

4.7 References for Chapter 4

[4-1] McBride, B. J., & Gordon, S. (1996). Computer program for calculation of complex chemical equilibrium compositions and applications: I. Analysis. *NASA reference publication*, *1311*, 84-85.

[4-2] Wada, Y., & Liou, M.S. (1997). An accurate and robust flux splitting scheme for shock and contact discontinuities. SIAM Journal on Scientific Computing18(3), 633-657.

[4-3] Leer, B.L., & Roe, P. (1991). Characteristic time-stepping or local preconditioning of the Euler equations. AIAA Paper, 91-1552.

[4-4] Marxman, G. and Gilbert, M., 1963, January. Turbulent boundary layer combustion in the hybrid rocket. In Symposium (International) on Combustion (Vol. 9, No. 1, pp. 371-383). Elsevier.

[4-5] Karabeyoglu, A., 2007. Combustion instability and transient behavior in hybrid rocket motors. Progress in Astronautics and Aeronautics, 218, p.351.

CHAPTER – 5

COMPUTATIONAL ANALYSIS OF HYBRID ROCKET INTERNAL BALLISTICS

5.1 Results of Steady State Characteristics

5.1.1. Prediction of Internal Ballistics

As the first step after the construction of the numerical model, an analysis of the prediction of the internal ballistics of the motor by the model is carried out. The conditions of the calculations are conformed to lab-scale experiments conducted with HDPE fuel and GOX oxidizer by Karabeyoglu [5-1].

The experimental specifications and motor configurations are provided below in Table. 5.1

Table 5.1 Experimental conditions for steady state validation [5-1]

Test Number	**Initial port internal diameter (mm)**	**Grain length (cm)**	**Nozzle throat diameter (mm)**	**Oxidizer flow rate (g/s)**	**Burn time (s)**
1	12.8	30.48	9.78	45.5	3.0
2	17.0	30.48	9.78	45.3	3.0
3	22.0	30.48	9.53	32.8	3.0
4	12.8	30.48	9.91	32.9	3.0

The physical properties of the fuel HDPE are as given in Table 5.2.

Fig. 5.1 a-h show the predicted internal ballistics variables conforming to Test 1 of Table 5.1. The axial length of 0.3048 m corresponds to the end of the fuel grain. After that, the results correspond to the convergent-divergent supersonic nozzle region.

Table 5.2. Physical properties of HDPE

Property	**Value**	**Unit**
Thermal conductivity, l_s	0.1554	W/ (m.K)
Density of the solid fuel, ρ_s	950	kg/m^3
Heat of vaporization, h_v	2719.6	kJ/kg
Thermal diffusivity, α_s	9.8 x 10^{-8}	m^2/s
Activation energy, E_a	2.52 x 10^5	J/mole
Pre-exponential factor, A_c	5 x 10^{11}	s^{-1}
Specific heat of the solid, C_p	1260	J/ (kg. K)

From the figures, the following can be explained. The density of the gas is high near the port entrance and gradually decreases over the axial length of the port. The combustion chamber pressure also decreases gradually over the fuel port. The mean velocity of the gas, the temperature and the mixture fraction increase over the port length as expected. Note that the mixture fraction is below the stoichiometric value of around 0.2 showing that the flowfield is oxidizer rich.

From Fig. 5.1.f, the regression rate is maximum at the port entrance and decreases monotonically along the port length, reaches a minimum and then increases. This axial dependence on regression rate can be explained based on the heat-feedback model used by us which is based on Marxman's diffusion limited analysis and can be expressed as below:

$$\rho_f r(\dot{x}, t) \propto G^{0.8}(x, t) x^{-0.2}(t) \tag{5.1}$$

It is seen that the fuel regression rate at any axial position, x mainly depends on the total local mass flux at the port G, and as a result depends on both the oxidizer flow entering the combustion chamber and all the fuel injected upstream of that axial location, x. Also, since, the value of G decreases as the port area increases during the burning, it is expected that the local regression rate decreases with time. However, the regression rate also exhibits a weak dependence on the axial position, which is because of the effect of the boundary layer growth on heat transfer. As the boundary layer increases in the downstream direction, the boundary layer temperature and velocity gradients perpendicular the fuel surface become less and so the convective heat flux also decreases. The combination of these two competing effects, results in a point of minimum regression rate downstream along the fuel port.

Fig. 5.2 shows the spatial regression rate for the same conditions as Test 1 from above, but with a grain length of 300.48 cm. The grain length is artificially increased here in order to have enough port length to observe the effects described above and obtain the point of minimum regression rate downstream. It shows relatively high regression rate near the leading edge of the fuel, but decreases with axial location for an interval, reaches a minimum and then increases again.

The point of minimum regression rate (highlighted by a yellow dot) corresponds to the crossover between the two competing effects of boundary layer growth. Nearer to the head end of the port, the effect of boundary layer is dominant, however more the distance from the head, more the effect of local mass flux becomes prominent. It is also seen that the point of minimum regression rate moves slightly downstream along time. It may be because the decrease of mass flux with time will tend to increase the boundary-layer growth effect and hence move the point of minimum regression rate downstream with time. However, with a large port length, there would come a point inevitable along the axis, the when the boundary layer thickness becomes equal to the port radius, which means that the hybrid boundary layers merge together. After they merge, the diffusion thickness for the oxidizer part becomes a large fraction of the port radius and changes very slowly with axial distance, resulting in different characteristics.

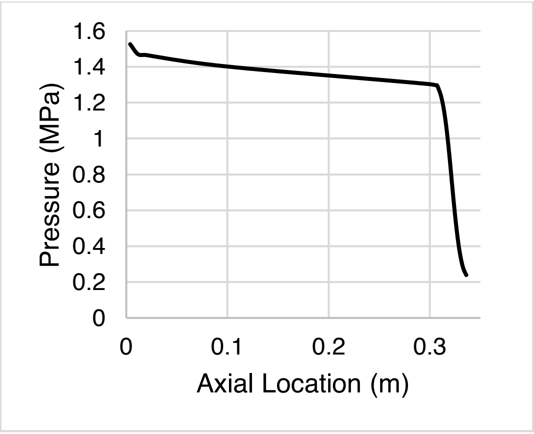

Fig. 5.1.a Steady State - Pressure

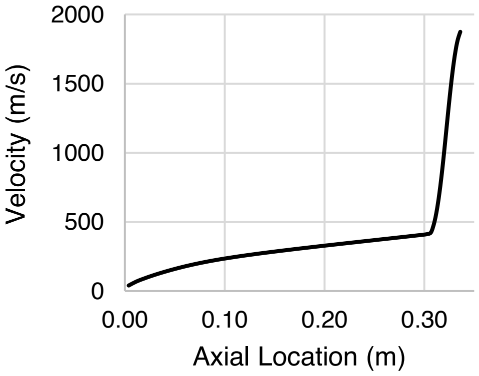

Fig. 5.1.b Steady State - Velocity

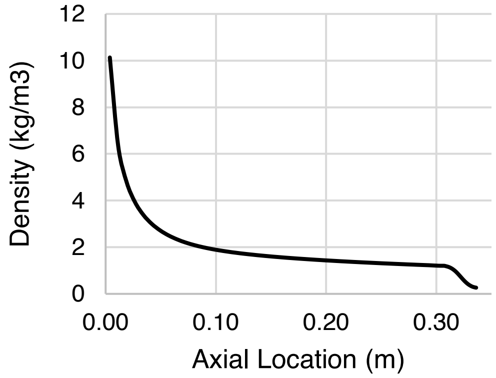

Fig. 5.1.c Steady State – Density

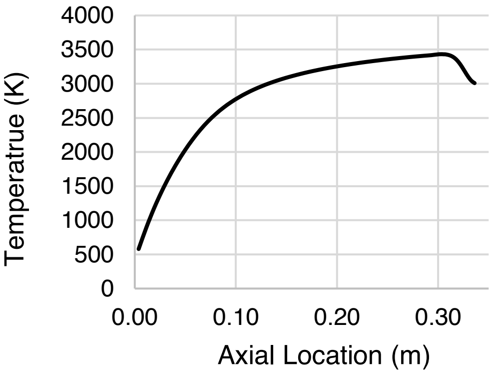

Fig. 5.1. d Steady State - Temperature

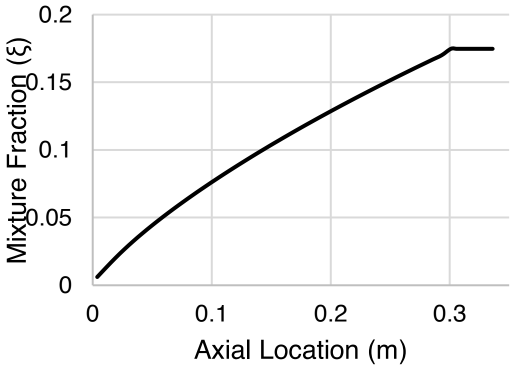

Fig. 5.1.e Steady State – Mixture Fraction

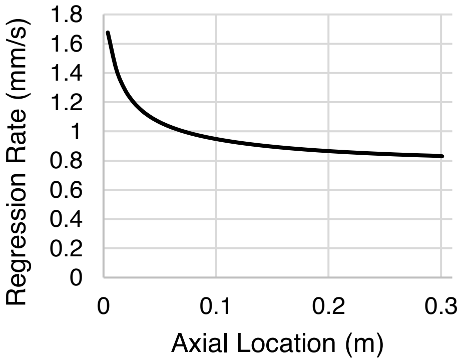

Fig. 5.1.f Steady State – Regression Rate

5.1.2 Grid Dependency Results

Grid convergence calculation has been carried out for the configuration of motor tests in Table 1. to determine the appropriate number of grid points required. Fig. 5.3 shows the representative case of Test 1's regression rate prediction for a grid configuration of X/Y where X is the number of grid points in the combustion chamber and Y is the number of grid points in the nozzle. Tests have been conducted with configurations of 20/10, 30/15, 40/20 and 50/25. As seen from the figure, a minimum of 40/20 grid points is necessary for grid convergence. Therefore, all calculations in this study are carried out using this configuration.

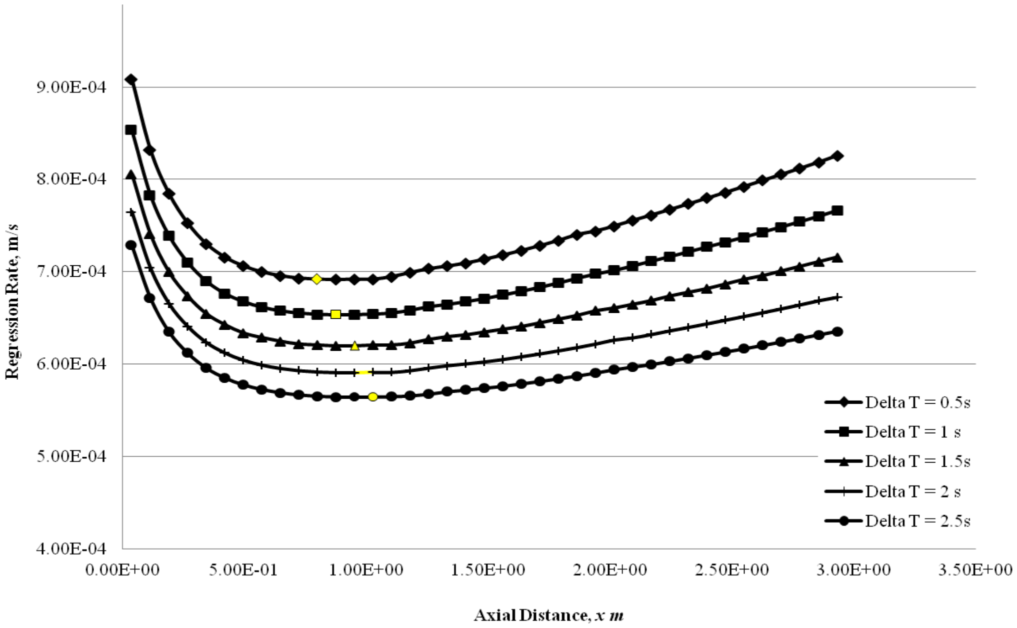

Fig. 5.2 Spatial regression rate at the end of different burn times

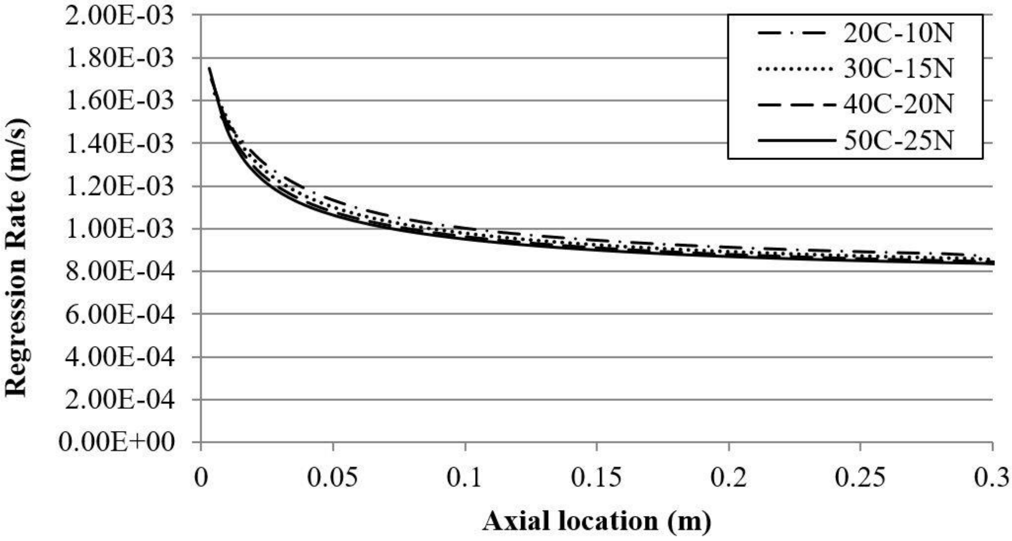

Fig. 5.3 Grid-convergence calculation result – Test 1

5.1.3 Validation of the Numerical Model

Results of the computational model and the experimental results are compared in Fig. 5.4**.** The X and Y axes are time and spatially averaged oxidizer mass flux (in kg/m^2. s) and regression rate (in mm/s) respectively. It is seen that our results vary from the experiments by a factor of

± 20 %. Also, the factors *a* and *n* obtained from our results are "0.0062" and "0.8353" as against "0.488" and "0.62" obtained from experiments respectively. It is seen that our model over-predicts the value of *n* when compared to the experimental result, however it confirms to the analytical value of approximately 0.8 which was proposed by Marxman [5-2]. Also, the values of the factors may be compromised because of the presence of only for data points.

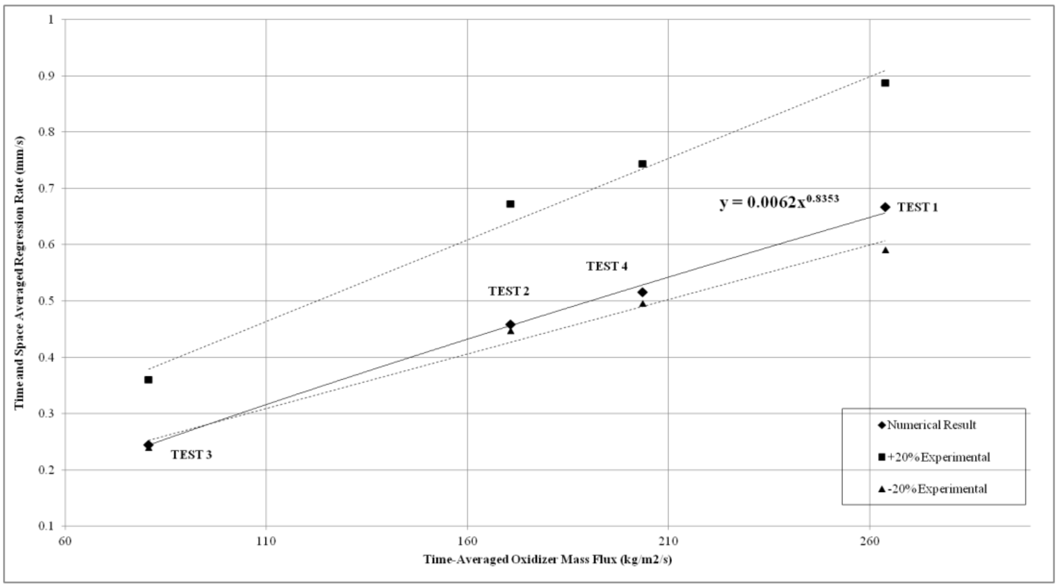

Fig. 5.4 Temporally averaged oxidizer mass flux Vs. Spatially and temporally averaged regression rate

Hence, it is concluded that our current time-dependent model can accurately predict the steady state regression rate with reasonable accuracy, and hence can be used for further investigation of time-dependent phenomena.

5.2 Results of Transient Characteristics

This section would present the results obtained during the transient analysis of the hybrid rocket motor. The motor specification is the same as that of the Test 1 from Karabeyoglu [5-1].

The rocket motor modelled may be considered as a series of oscillations each with its own characteristic springs and damping coefficients and unique frequency of oscillation, connected in a non-linear fashion. In our numerical modelling, the oscillators modelled are the thermal oscillator of the solid fuel, the acoustic oscillator due to the gas dynamics in the closed combustion chamber. Associated with each of the oscillator is a characteristic damping - the thermal damping effect and the supersonic nozzle damping respectively. Other oscillators that could be modelled into the system are the boundary layer oscillator and the vortex shedding oscillator. Due to the damping presented by these oscillators, it is expected that system would tend to be stable, unless there is a coupling between any of the oscillators resulting in a closed feedback loop that satisfies the Rayleigh criterion that is defined as [5-4],

> *"If heat be given to the air at the moment of greatest condensation, or be taken from it at the moment of greatest rarefaction, the vibration is encouraged. On the other hand, if heat be given at the moment of greatest rarefaction, or abstracted at the moment of greatest condensation, the vibration is discouraged.".*

This can be expressed mathematically, by defining the unsteady heat release *q (x, t)* and pressure oscillation *p (x, t)*. Then the necessary condition for the existence of combustion instability is satisfied if,

$$\int \int \int p(x,t)\ q(x,t) dV > 0 \qquad (5.2)$$

Therefore, strictly speaking, the instability of the combustion is not the primary issue, the coupling between this heat-transfer between the combustion and the fluid motion such as pressure or velocity are the drivers of the 'combustion instability'. This is in particular a challenging problem, because the necessary energy required for triggering and sustaining these oscillations can easily be provided by the combustion phenomenon itself. Reverting to the discussion on the oscillators modelled in the hybrid rocket, it is clear from the discussion in Section 3.1 of Chapter 3 that under certain conditions such as delayed feedback, it is possible that the system can have a 'negative' damping. Under this case, it is possible that if the negative damping is large enough that the overall damping of the system becomes negative, then it is expected that all the oscillators present in the system would be excited and oscillate in their respective natural frequencies. This is the central proposition of the thesis and it would be shown that how certain effects such as the boundary layer delay can give rise to instabilities in hybrid rocket motors.

5.2.1 Transient Behaviour of the Thermal Oscillator

Before a transient analysis using the combined numerical model developed in Chapter 4 and used above for the steady state analysis in Section 5.1 above, at first, the behaviour of the transient behaviour of the thermal oscillator would now be explained. Considering the standalone Thermal Model developed in Section 4.5, the response of the solid fuel thermal conduction to a varying heat-flux would now be considered. Note that the surface temperature and therefore the regression rate is still solved using the energy balance equation (Eqn. 4.2.60). However, the heat into the solid due to the flame is not modelled and instead given directly as input to the solid fuel surface.

The case of instantaneous throttling is considered. These cases are simulated by the usage of a step function for the heat loading to the solid fuel surface. Fig. 5.5 shows the response of the regression rates for different activation energies of fuels along with the instantaneous response curve. In the case of instantaneous response curve, it is assumed that the solid fuel has zero thermal lag. Hence, it represents exactly the shape of the heat input. The response of the regression rates follows the instantaneous curves perfectly, but results in overshooting the final steady value by around 20 %. However, with time, the curve relaxes to its equilibrium position. In the Fig. 5.5, the regression rate is non-dimensionalized with respect to the initial steady state value before throttling. The throttling ratio is 2:1 throttle up situation for the PE fuel with the value of the input heat flux being fixed constant in all the three cases.

From this result, important deductions can be made. This overshooting phenomenon can be explained because of the rapid change in temperature in only a very small region close to the regressing surface upon the application of an instantaneous headload. Note that, as given in Eqn. 4.2.60 and in Eqn. 4.5.2, only the thermal gradient at the surface determines the instantaneous regression rate.

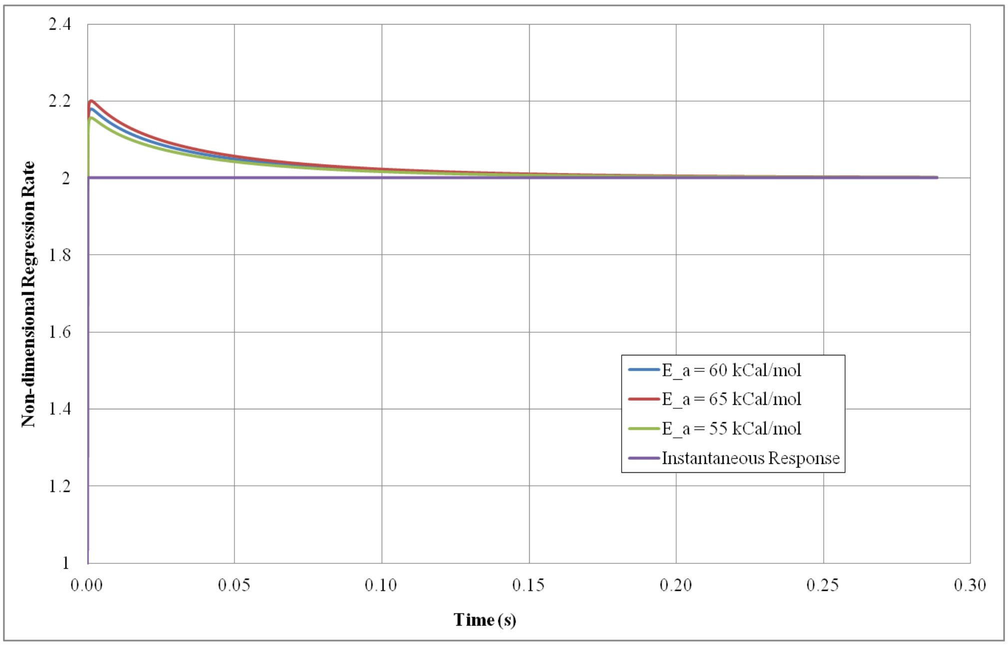

Fig. 5.5 Overshooting of the thermal oscillator during instantaneous throttling

When an instantaneous input is applied, the region near the surface responds first and fast, whereas the rest of the profile remains unchanged. In this very short time, the surface temperature and the surface temperature gradient (parameters which define the regression rate) reach the value at the end steady state and cross it. This sudden adaptation of the temperature profile close to the surface results in the overshooting phenomenon. The decay asymptotically to the steady state is because of the relaxation time of the entire thermal profile inside the solid fuel conduction zone. An estimate of the thickness of the conduction zone, e_{cond} and the associated residence time can be given by considering the Eqn. 4.5.3. Assuming that, T- T_{wall} is 10^{-2} times that of the T_s, we obtain,

$$e_{cond} = \frac{\alpha_s}{\dot{r}} \ln(10^2) \qquad (5.3)$$

For example, assuming a regression rate of 1 mm/s and a thermal diffusivity of 1E-03 cm^2/s, we get a conduction thickness of 0.45 mm and the associated timescale of 0.5s. The important idea is that this timescale is also dependent on the regression rate. Upon the increase of regression rate, the time scale decreases. Also, to be noted is that, this timescale is different from the timescale of the solid fuel kinetics associated with the pyrolysis and degradation of the solid fuel in a zone very close to the regressing surface. This mechanism is though not explicitly modelled in our current study. The thickness of the degradation zone, $e_{pyrolysis}$ can also be derived [5-5] and is given as,

$$e_{pyrolysis} = \frac{-\alpha_s}{\dot{r}} \ln\left(\frac{1 - \Delta T}{T_s - T_{wall}}\right) \tag{5.4}$$

Where $\varDelta T$ is taken as 150K and upon substituting same values of $\dot{r}$ being 1 mm/s and the thermal diffusivity being 1E-03 cm^2/s, the thickness of this reaction zone comes to be 25µm with an associated residence time of 25ms.

Due to these characteristic delays present in the system, it is possible that another mechanism such as the boundary layer delay can interact with this thermal oscillator and produce instabilities. This would be the case, as would be shown in the next sections.

5.2.2 Perturbation Analysis

The numerical model that has been described in the Chapter 4 and used for the prediction of steady state regression rates shown in section 5.1 earlier would now be used for the transient analysis. Global time stepping is used now instead of the local time stepping employed earlier in order to obtain time accurate solutions.

The first methodology of investigation is the perturbation analysis which has been well studied and applied previously to studies in combustion instability (for e.g. by Shimada et. al. [5-3]). The method is to apply a small initial perturbation to the steady state solution of the system and then follow its temporal evolution in order to investigate the growth/decay characteristics. If the system is in stable equilibrium, then the oscillations should decay out, however, if the system is in unstable equilibrium, then the oscillations are expected to grow. Since, in hybrids, the regression rate depends on the oxidizer mass flux instead of pressure, pressure perturbations are not added. However, it is also possible that the regression rate for hybrids depends on pressure not directly, but through the mass flux, which is a product of density and velocity and density being a linear function of the chamber pressure when ideal gas law is used. But this cannot be conceptually predicted as a change in pressure may not lead to significant increase in mass flux because the velocity can accommodate itself to keep the changes in mass flux small. Therefore, the initial perturbation is applied by adding first mode each of standing wave of density and velocity to the steady state results. This is defined by

$$G(x,0) = G(x) + amp(G_o(x)) \cos\left(\frac{\pi x}{L_P}\right) \tag{5.5}$$

The value of *amp* is the amplitude of perturbation added, expressed as percentage of the steady state value. In our study, the value was varied as 0.1, 1 and 10%. Note that for these simulations, the steady state form of the convective heat-flux is used without any boundary layer time delay.

Fig. 5.6, shows the percentage change in the regression rate vs. time plots, at the head-end, middle of the chamber and the chamber exit for initial perturbations with velocity and density respectively. The percent change is calculated with respect to the initial steady state values. It is seen that in all the cases, there is a rapid decay in the regression rate oscillations indicating the lack of a driving force needed for the amplification. This concludes that the motor modelled by the numerical model is inherently stable.

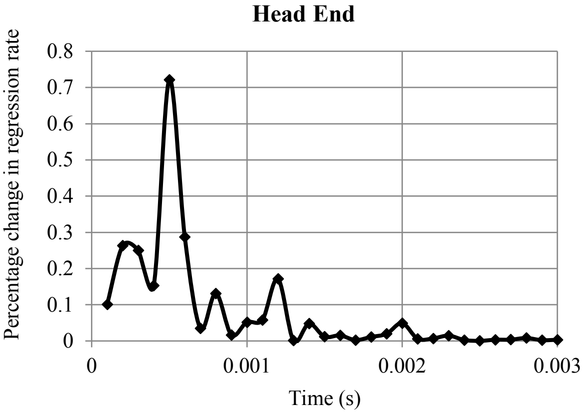

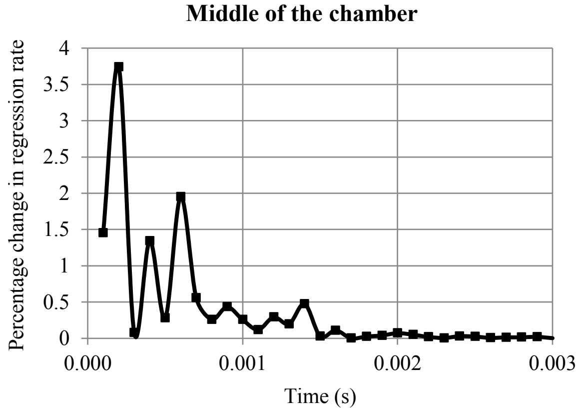

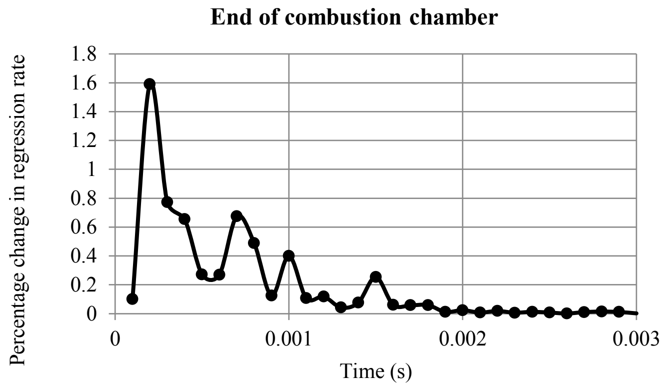

Fig. 5.6 Temporal solution with initial velocity perturbation

5.2.3 Modeling Boundary Layer Delay

As explained in Chapter 3, the assumption that the boundary layer adjusts itself instantaneously to the changes in the oxidizer mass flux and regression rate fails to be true. This is because of the finite time needed for the information to propagate from the edge of the boundary layer to the axial position in the burning surface at its diffusion speed. This boundary layer delay in the propagation of information can result in instability. To this end, in order to simulate such a delay, the equation for heat flux to the regressing fuel surface as defined earlier in Eqn., 4.3.1 is modified as,

$$\lambda_g \left(\frac{\partial T}{\partial y}\right)_{y=+0} (x,t) =$$

$$\left[\frac{0.03\, q}{\mu^{-0.2}}\right]^{\frac{1}{(1-k)}} (x,t) \left[\frac{B_t h_v'}{\frac{k}{\rho_s^{(1-k)}}}\right] (x,t)\; x^{\frac{-0.2}{(1-k)}}\; G^{\frac{0.8}{(1-k)}}(x,t)\, \dot{r}_{old}^{\frac{-k}{(1-k)}}(x, t-\tau_{bl}(x)) \qquad (5.6)$$

Here, $\dot{r}_{old}$ represents the regression rate calculated not at current time, but at some finite time in the past $(t-\tau_{bl}(x))$, depending on the value of the boundary layer delay time τ_{bl}. This way, a delay in the propagation of information from the edge of the boundary layer to the axial location on the fuel grain surface is established.

This time delay is a function of the thickness of the boundary layer and the macroscopic turbulent diffusion speed. The thickness of the boundary layer for an incompressible flow over a flat plate is defined as,

$$\delta = 0.3xRe_x^{-0.2} \tag{5.7}$$

The diffusion speed is a function of the molecular viscosity and the shear stress and can be represented as,

$$u^* = \sqrt{0.03u_e Re_x^{-0.2}} \tag{5.8}$$

This results in the boundary layer delay being of the form,

$$\tau_{bl}(x) = \frac{2.18Re_x^{-0.1}x}{u} \tag{5.9}$$

Note that this is the turbulent boundary layer delay for an incompressible flow over a flat plate. As seen from the results, the dependence on the local Reynolds number is rather weak. Therefore, for the case of hybrids, this delay can be approximated by a constant and described just as a function of x and port velocity u, [5-5]

$$\tau_{bl}(x) = \frac{2.05\,x}{u} \tag{5.10}$$

This boundary layer delay should be a function of both axial location and time. As the flow field changes temporally, the Reynolds number and the port velocity also change and which as a natural corollary also changes the local boundary layer delay. However, as first order approximation, the temporal changes to the boundary layer are not considered in our model and steady state values are used to determine the Eqn. 5.10. Fig. 5.7 shows the boundary layer delay profile along the port length for the case of Test 1 of Table 5.1.

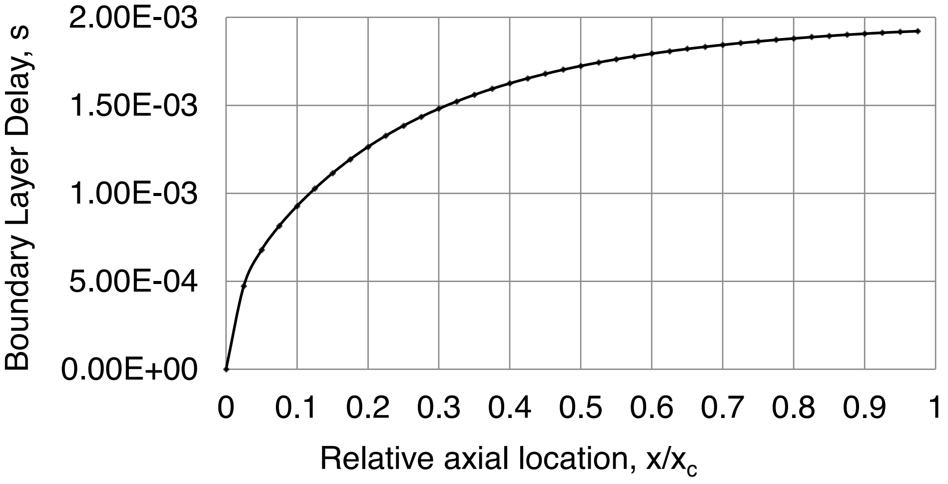

Fig. 5.7 Boundary Layer Delay along Port Length

In addition, as discussed in Chapter-3, the value of C_f/C_{f0} can be predicted by Eqn. 4.3.6, which is a power law fit to the original expression in Eqn. 3.7. However, since at small values of B_a, the power law fit can give unphysical values of greater than, in our calculation, the maximum value is explicitly imposed as not greater than 1.

5.2.4 Results Obtained on Modeling Boundary Layer Delay

As expected from the analysis in Chapter-3, it is found that upon modelling this boundary layer delay experienced by the wall heat flux to the changes to the regression rate, the system is found to be unstable. It is expected that the coupling of the boundary layer oscillator and thermal oscillator in the low-frequency region results in the system being unstable.

Since, the system is intrinsically unstable, the initial source of perturbations may be the intrinsically perturbations (below the residual limit of 1E-06) present in the numerical model. Before a discussion of the results, we also define the non-dimensional parameter, η

$$\eta_* = \frac{* t}{* \,(steady\ state)} - 1 \tag{5.11}$$

Where * can be any parameter in consideration.

Fig. 5.8.b shows a representative temporal plot of non-dimensionalized pressure, η_p monitored at $x = xc/2$ (centre of the combustion chamber). A linear region having increasing amplitude of pressure is seen at the beginning as shown in Fig. 5.8.a). It then transitions into a non-linear region, as the non-linear effects begin to dominate, resulting in a limit-cycle.

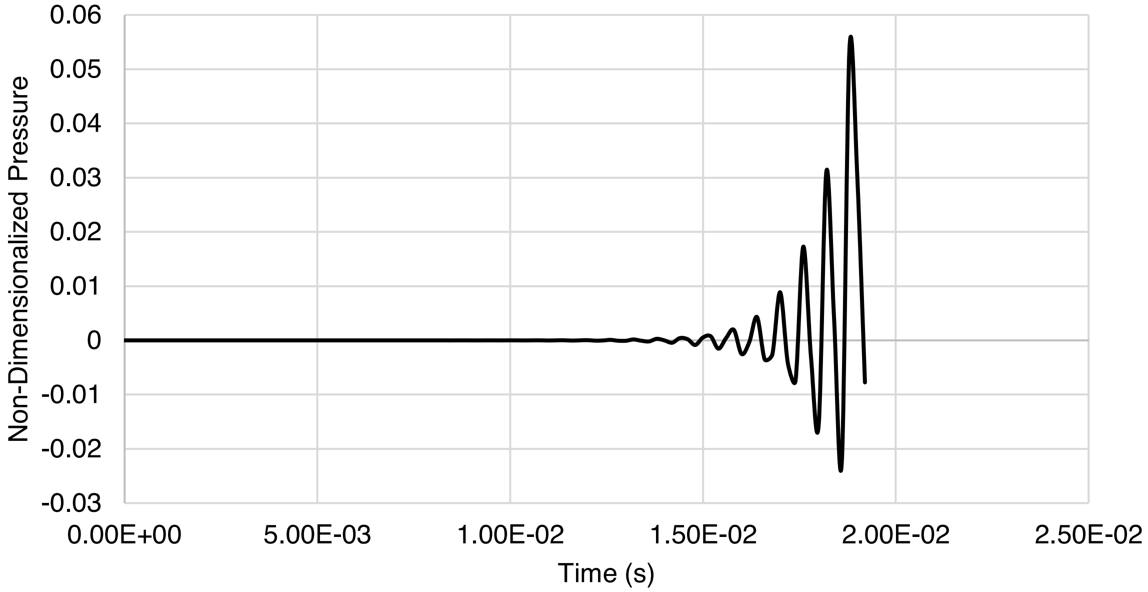

Fig. 5.8.a Linear region to non-linear transition

Limit cycle is a classic non-linear behaviour denoted by the condition when the total energy added to the system and the energy spent by the system (in this case – by exiting through the supersonic nozzle) is equal.

For example, with an analogy to the Lienard-type non-linear equation of the type in Eqn. 3.23,

$$x(t) + A\ (\text{-B+C}x^2 - D(x))x(t) + Ex(t) = 0$$

Depending on the value of parameters B, C, D in the damping term - A (B-Cx^2 + $D(x)$), the system can have either positive or negative damping. If the net damping is negative initially due to the terms -B and -D(x) being dominant, then the system would be unstable resulting in oscillating increase in x. However, with increasing value of x, the value of the positive damping term, Cx2 increases until the net damping becomes zero – resulting in the establishment of a limit cycle. As a direct expression for hybrid rocket in the form above is not available, a direct explanation cannot be not provided. However, it is well known that the rocket system would have damping due to the thermal damping and supersonic exhaust nozzle damping and therefore it is expected that the system should have a limit cycle.

Alternately, the presence of limit cycle in a combustion instability process can also be explained by the presence of only a finite energy that can be delivered to the system through the combustion process because of the limitations of the chemical energy present in the fuel-oxidizer combination.

A positive DC shift in the mean value of pressure amplitude is also seen. DC shift is as a result of the increase in the mean energy added to the system. In this case, the pressure oscillations' increase in amplitude results in the additional energy of the system resulting in the DC shift. Typically, in solids, DC shift has been attributed due to the velocity coupling between the pressure oscillations and the burning surface. A similar mechanism in hybrids is thought of the reason for this non-linear effect.

The initial overshoot in the result is due to the characteristic thermal overshoot. This phenomenon is due to the sudden adaptation of the temperature profile within a very small zone close to the regressing surface in contrast to the much slower thermal relaxation of the entire solid grain (as shown in Fig. 5.5). The total amplitude of the pressure oscillations is greater than 5% and therefore this unstable behaviour can be termed as 'combustion instability'.

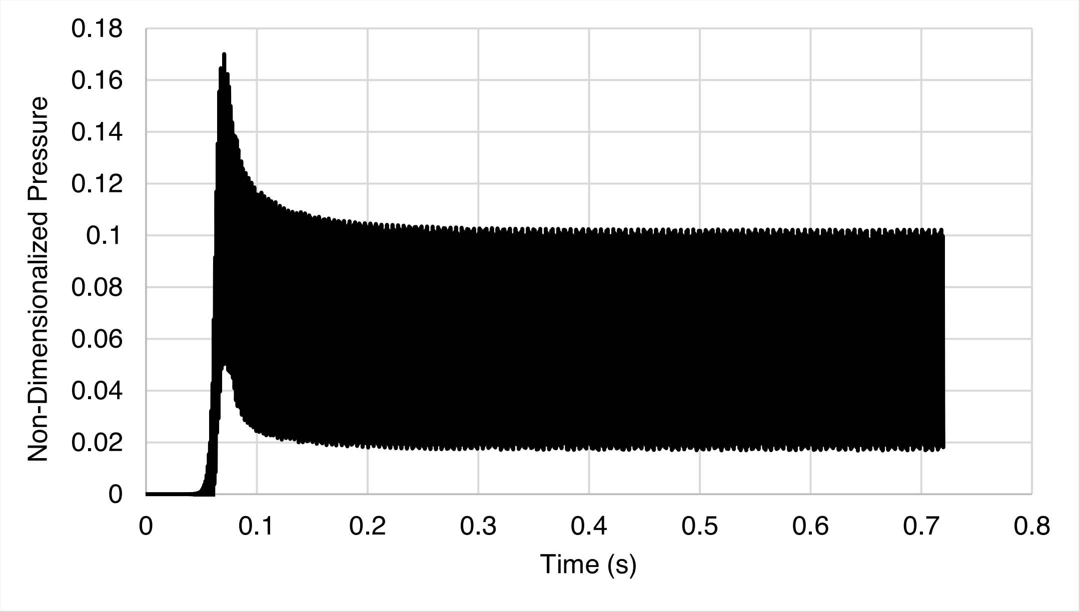

Fig. 5.8.b Temporal variation of Non-Dimensionalized Pressure

The pressure oscillations are largely due to the acoustics and the regression rate oscillations are due to the combination of the boundary layer-thermal oscillators This clearly shows that as a result of the presence of boundary layer delay, and as shown in Chapter 3, the system can be said to have a negative damping, that excites all the natural modes present in the system.

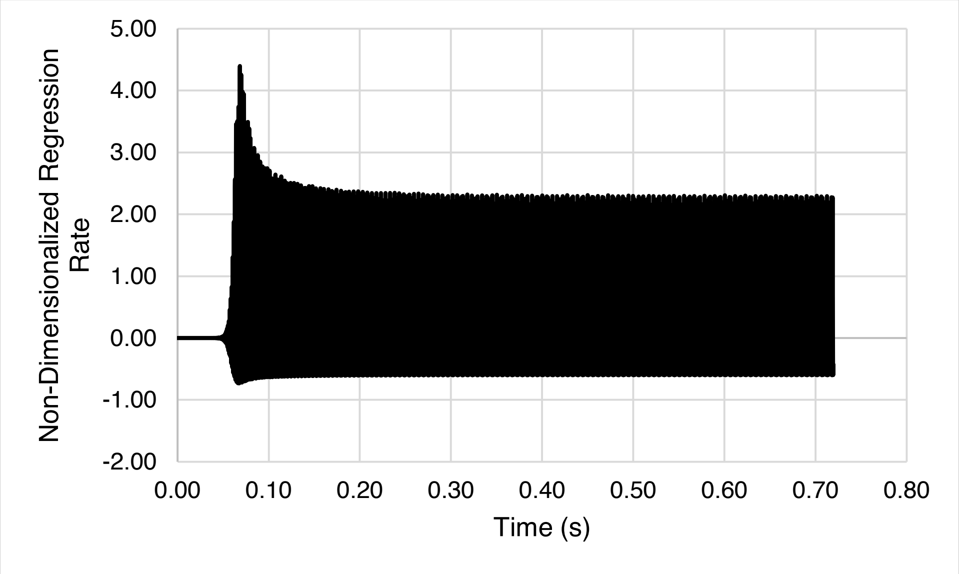

Fig. 5.9 Temporal variation of Non-Dimensionalized Regression Rate Variation

Fig. 5.9 shows a representative temporal plot of non-dimensionalized regression rate, η_{reg} monitored at the same point. Qualitatively, it shows similar results to the pressure perturbations. A linear-like region is seen first, which then develops into a non-linear limit cycle.

In order to study the results more quantitatively, the FFT of the oscillations in the limit cycle region is taken and studied for all cases in our study. The sampling period for the analysis is taken to be at least ≥ 0.5s, in order to be able to be long enough to capture also the low-frequency oscillating phenomena (which is of interest to us, as the Hybrid ILFI is a low-frequency instability). The sampling rate is 5kHz and therefore the ensuing frequency resolution ins 2.4Hz. Fig. 5.10 shows the FFT of pressure oscillations.

The results of the FFT are tabulated in Table 5.3 below. It is seen that the peaks in the FFT correspond to the intrinsic hybrid boundary layer combustion instability, the formula for which is given in Chapter 2 – Eqn. 2.1. The other peaks correspond to the well-known thermal, 1L acoustic and Helmholtz (chamber bulk) modes of the system. As seen from the results, apart from the primary hybrid oscillation mode, a possible harmonic of the same is also seen. This is thought of as an artefact of using a simple delay mechanism for the boundary layer delay instead of modeling the complex process.

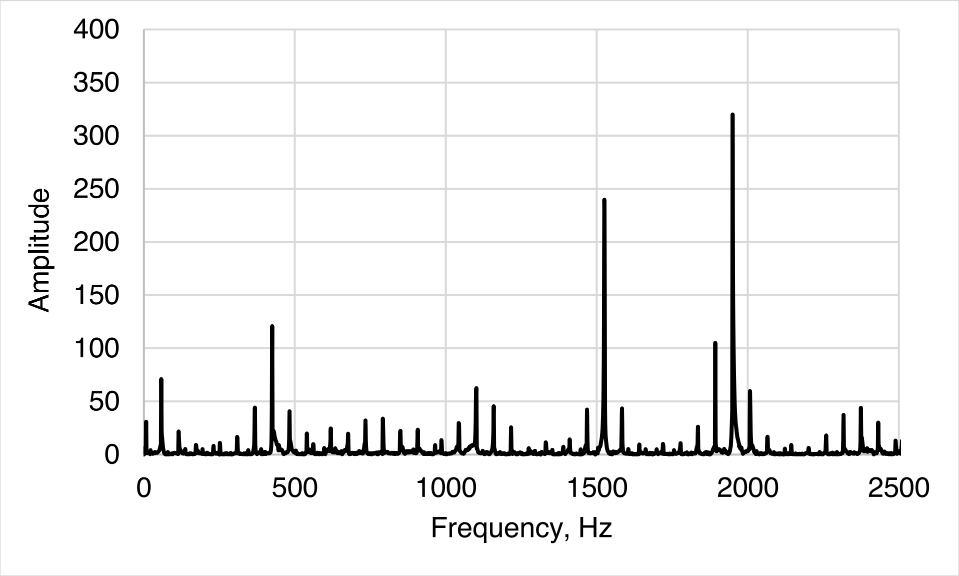

Fig. 5.10 FFT of Pressure Oscillations

Now, the FFT of the regression rate oscillations in the limit cycle for the same case is considered. Similarly, peaks corresponding to the natural modes of the system are found to be excited.

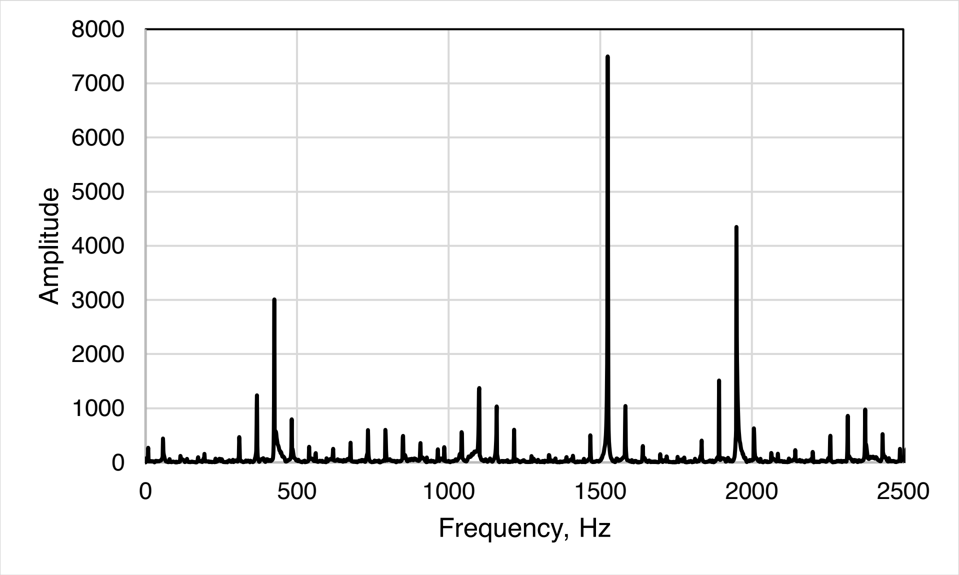

Fig. 5.11 FFT of Regression Rate Oscillations

Table 5.3 List of frequency prediction for different modes present

Natural Modes Present	Depends on	Theoretical Prediction of Frequency	Numerical Result
Solid fuel thermal mode	Thermal diffusivity and regression rate	$f_{thermal} = \frac{1}{\left(\frac{\alpha}{\dot{r}^2}\right)} \sim$ 8 Hz	9 Hz
Hybrid Boundary Layer mode	Boundary layer delay (Here, avg. = 1.26 ms)	$f_{TBL} = \frac{0.48}{\tau_{avg}} \sim$ 379.70 Hz	424.25 Hz
Helmholtz Mode [5-6]	Speed of sound, chamber and nozzle dimensions	$f = \frac{c}{2\pi}\sqrt{\frac{\pi R_t^2}{\vartheta(l+1.6R_t)}} \sim$ 1496.29 Hz	1520.89 Hz
Acoustic 1-L mode	Speed of Sound, Chamber Length (Here, Avg. c ~ 1130.74 m/s) Corrected for DC Shift	$f_{1L} = \frac{c}{2X_c} \sim$ 1837.34 Hz	1949.40 Hz

5.2.5 Spatial Variation Effects

So far, all the comparisons for the transient behaviour has been done only at one axial position in the combustion chamber. It is interesting to study the localized behaviour at various axial positions inside the combustion chamber of the motor. Fig. 5.12 shows the pressure variation over the chamber length of the motor. It is observed that higher order acoustic modes are present with characteristic pressure nodes and anti-nodes.

However, since over a long period of time, the pressure oscillations at any given location averages out, it is necessary to study the oscillations over certain characteristic time scales. Fig. 5.13 shows the variation in pressure amplitude over the characteristic time scale of ≈ 2.4E-03 which is of the time scale of the boundary layer delay in the motor. Higher order acoustic modes present are readily observed. But they are not captured in the FFT because of the sampling frequency of choice.

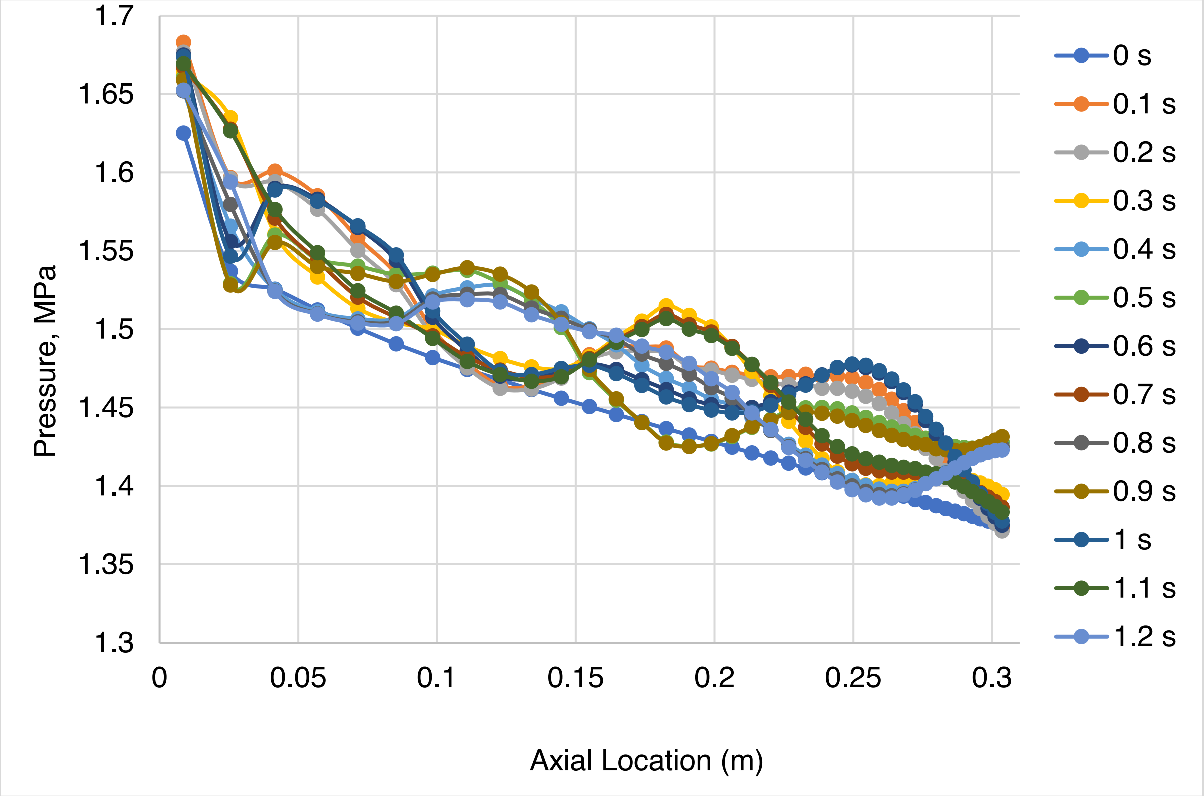

Fig. 5.12 Spatial variation of Pressure at Different Time

If it's necessary to study only the spatial variation of hybrid boundary layer mode, then it is necessary to apply a numerical filtering to the data in order to remove the higher frequency components.

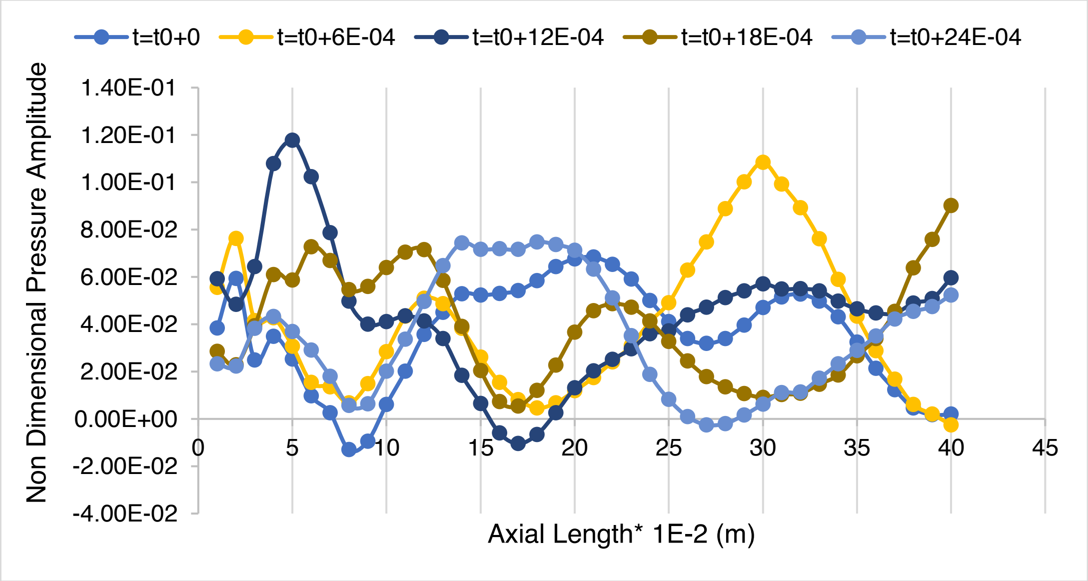

Fig. 5.13 Spatial variation of Non-Dimensionalized Pressure Amplitude

In order to compare the frequencies at different spatial locations in the combustion chamber, FFT is carried out for non-dimensionalized pressure and regression rate data at 3 monitoring points – the head end of the combustion chamber, the middle of the combustion chamber and the end of the combustion chamber. As shown in Fig. 5.15, similar peaks in the FFT were obtained, however with different relative amplitude values. The amplitude values can be seen in Fig. 5.14.

While with different axial locations, different boundary layer delay values are present tending one to think that different frequency of intrinsic hybrid boundary layer mode should be obtained, it is seen from Fig. 5.15, that the system due to being non-linearly coupled together oscillates with a frequency surrounding the average boundary layer delay, at all axial positions.

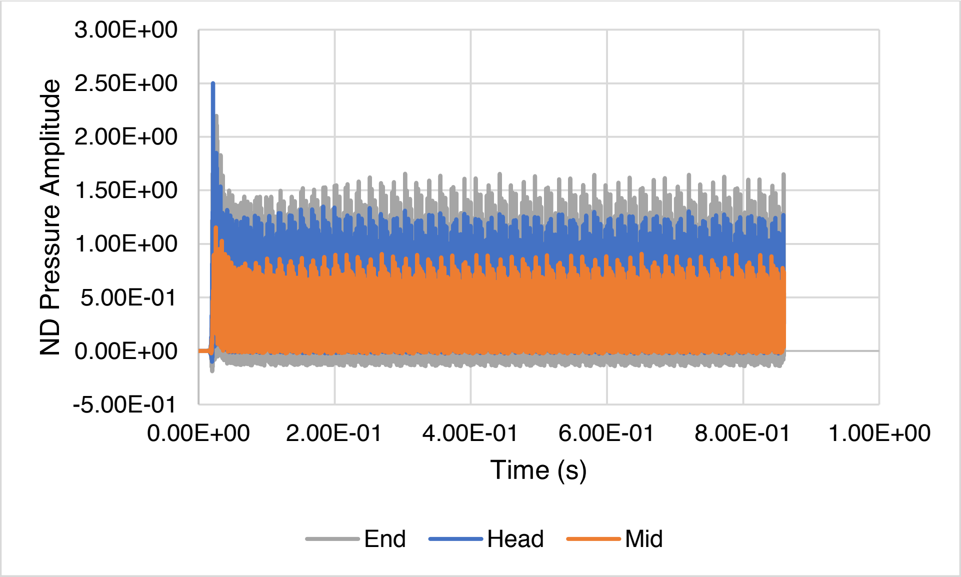

Fig. 5.14 Time varying non-dimensionalized pressure amplitude at 3 different axial locations

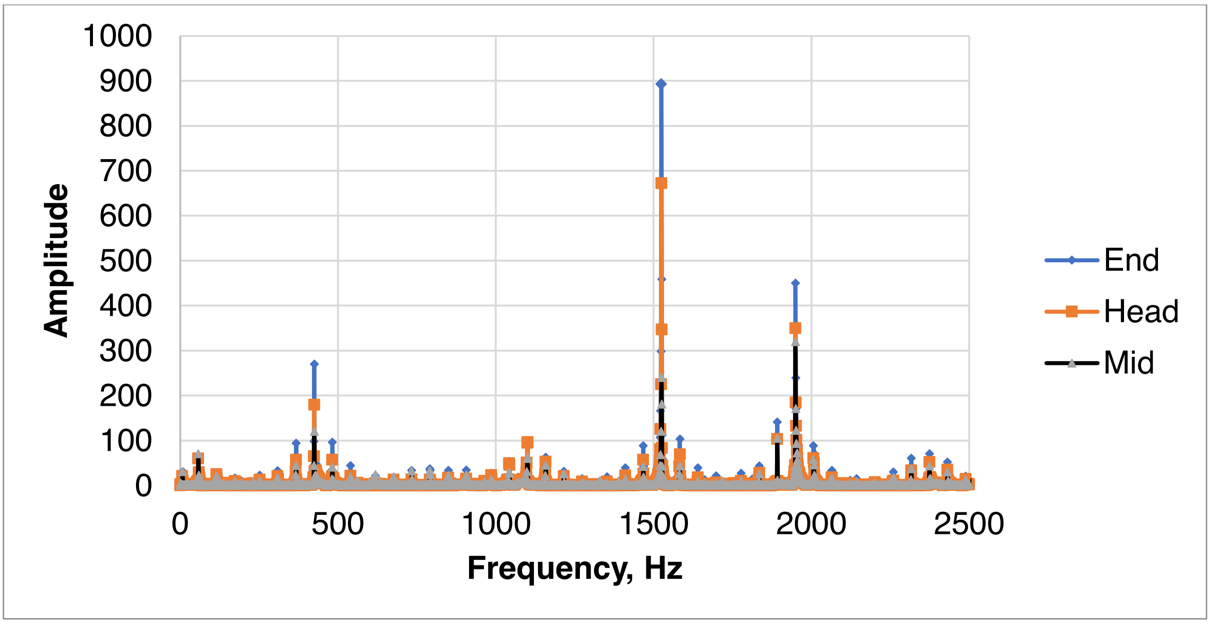

Fig. 5.15 Spatial variation in FFT of Pressure Oscillations

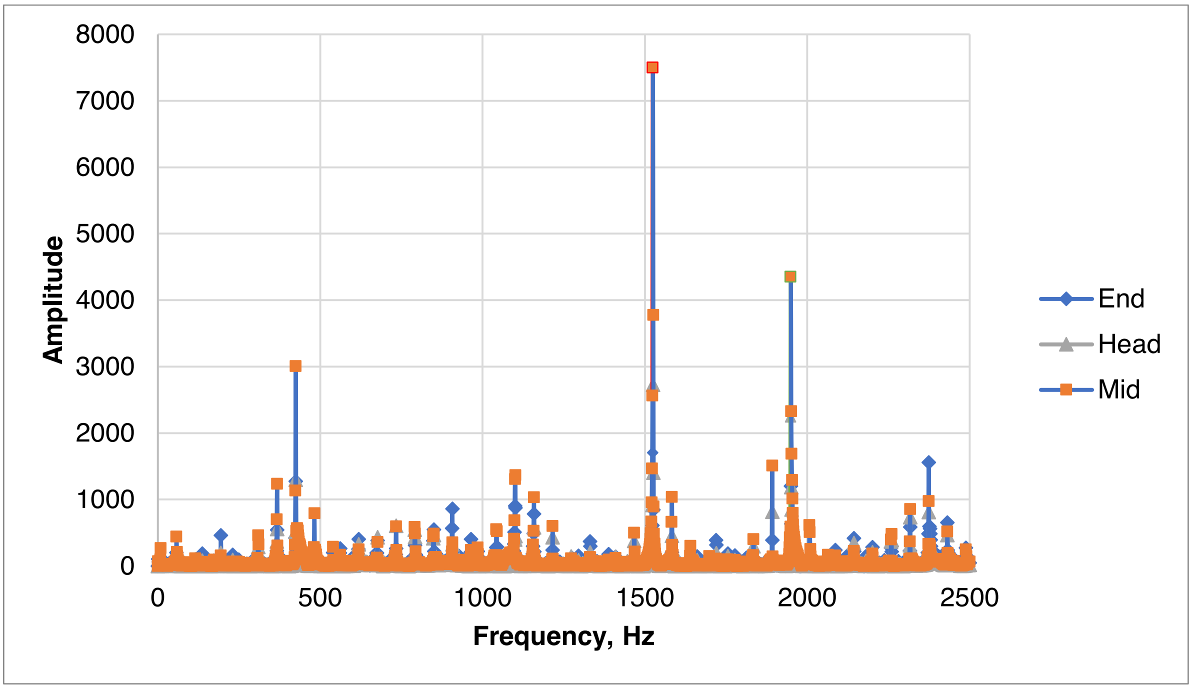

Fig. 5.16 Spatial variation in FFT of Regression Rate Oscillations

5.3 Parametric Analysis

5.3.1 Effect of Boundary Layer Delay

As highlighted in the discussion above, the most important parameter governing the hybrid rocket intrinsic combustion instability (ILFI) is the boundary layer delay. Therefore, it is pertinent to study the effect of this boundary layer delay on the combustion instability characteristics. Understanding this effect, would help to design better rocket motors that can utilize this knowledge to reduce the effects of ILFI. For the parametric analysis, the boundary layer delay value is artificially modified to be 0.05, 0.1, 0.5, 1, 1.5, 2, 2.5, 3 and 3.5 times as that of the system's inherent delay values (T), as expressed by Eqn. 5. 10. This discretization of the magnitude increase between each case was considered to be at least 0.5 times the system's inherent delay in order to better identify the frequency of the primary hybrid oscillation. All other parameters are kept as constant and the simulations are then run.

5.3.1.1. Effect on the Frequency of Oscillations

In order to see the effect of the boundary layer delay values on the frequency of oscillations in the limit cycle, the FFT of the pressure oscillation of the limit cycle amplitude are taken. For the comparison of the FFT, only those simulations in which the limit cycle had been simulated for at least 0.5s were considered in order to ensure that the sampling period was long enough to capture well the low-frequency phenomenon. Fig. 5.17 a, b c and show the FFT of the pressure oscillations (monitored at centre of the combustion chamber) corresponding to the boundary layer delay $\tau_{bl} = 2T, 2.5T$ and $3T$.

The same is compared against theoretical prediction in Table. 5.4. It is seen that with increasing τ_{bl} values, the corresponding frequency of the primary hybrid oscillation frequency also changes. It also holds good agreement with the prediction by theory. Even though some cases have disparity, our current simulation has a variety of boundary layer delay based on the axial locations; therefore, correspondingly, it is possible that more than a single frequency for the hybrid boundary layer mode may be present in the results.

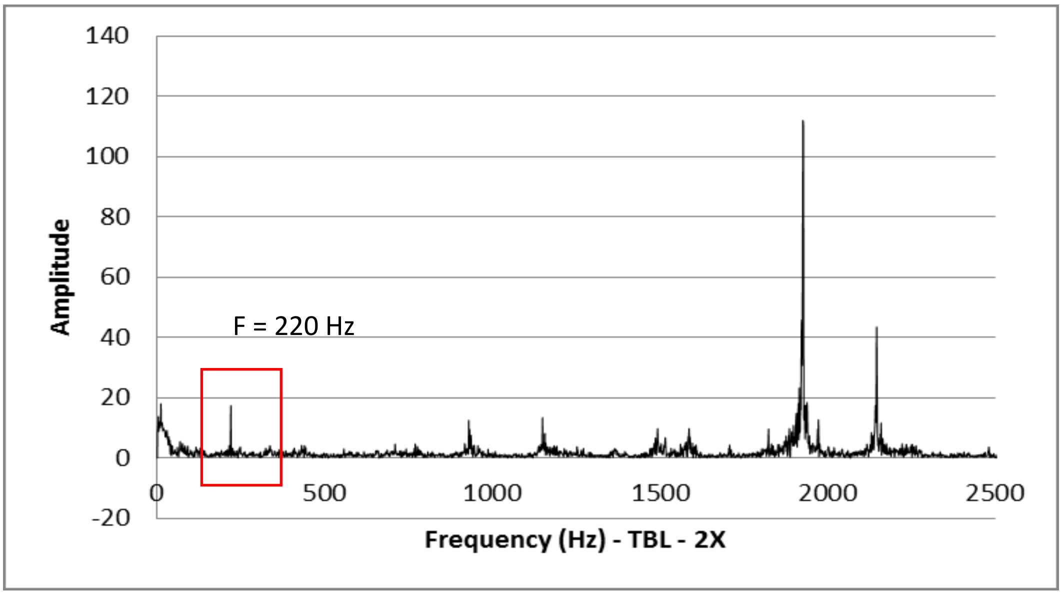

Fig. 5.17.a FFT of Pressure Oscillations for $\tau_{bl}=2T$

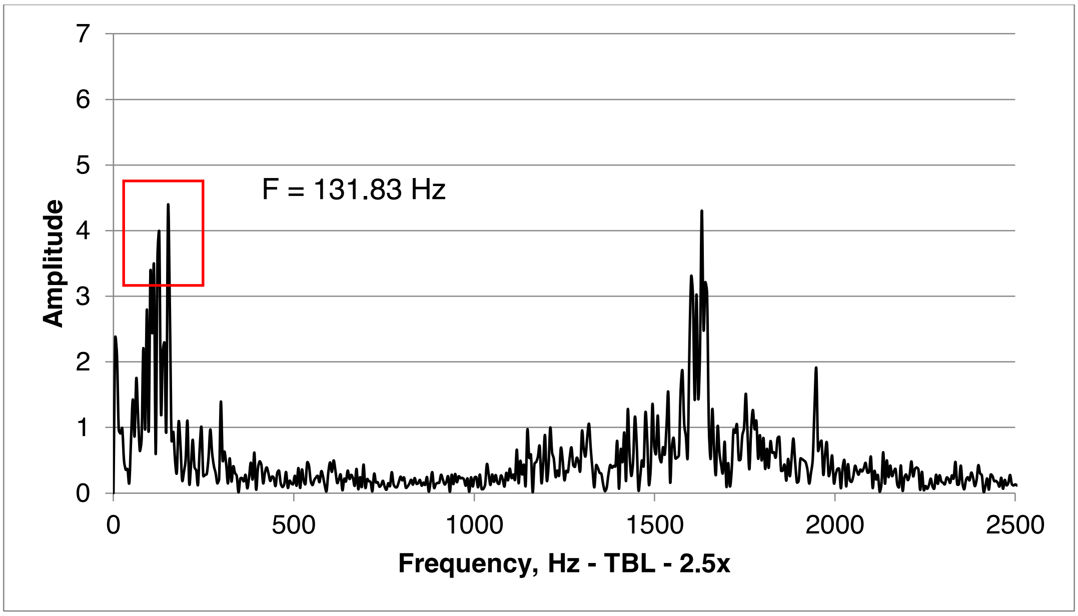

Fig. 5.17.b FFT of Pressure Oscillations for $\tau_{bl}=2.5T$

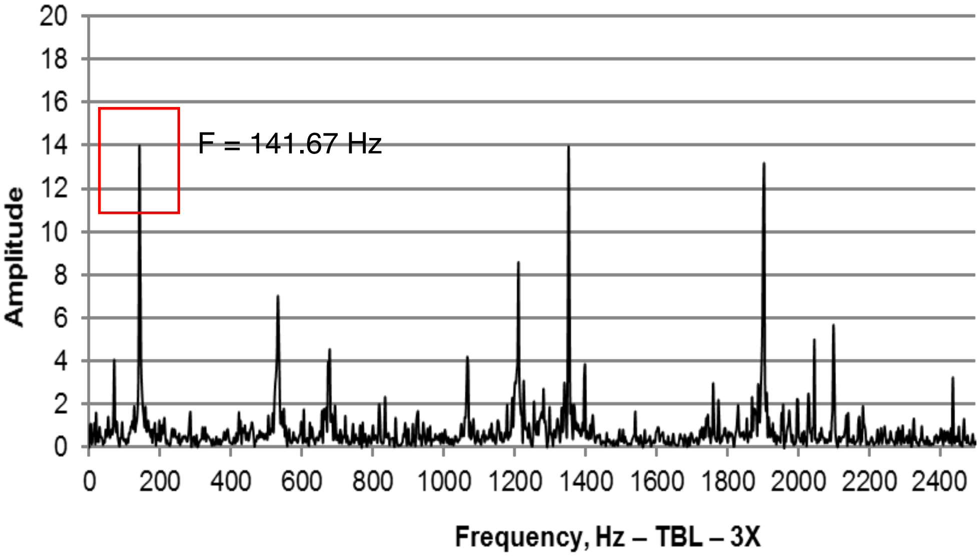

Fig. 5.17.c FFT of Pressure Oscillations for $\tau_{bl}=3T$

Table 5.4 Numerical prediction of frequency of primary hybrid oscillation mode

Parameter, TBL	1 T	2 T	2.5 T	3 T
Numerical simulation frequency prediction, Hz	333.25	219.72	131.83	141.60
Estimated from theory, Hz	379.70	189.85	151.88	126.57
Error in %	-12.23	+15.55	-13.2	+10.61

5.3.1.2 Effect on the Non-Linear Behaviour

From Fig. 5.18, qualitatively, it is observed that with increase in the boundary layer delay, there is an increase in the amplitude and DC shift. In order to measure qualitatively, RMS amplitude and DC Shift % are compared for the limit cycle regions. RMS amplitude is compared instead of the peak to peak amplitude because of the rough nature of oscillations.

The amplitude and the magnitude of DC shift are now compared. Fig. 5.18.a and 5.18.b show the change in the RMS amplitude and magnitude of DC shift for different values of $\tau_{bl.}$ An increase in both the quantities is seen with increasing values of boundary layer delay. A logarithmic correlation (given by the best-fit dotted lines) can be fit to the given number of data points. This increase in the amplitude and DC shift with an increasing boundary layer delay value can in a way be attributed to the increased to the increased value of negative damping present in the system (Refer Section 3.2 and Eqn. 3.2.1).

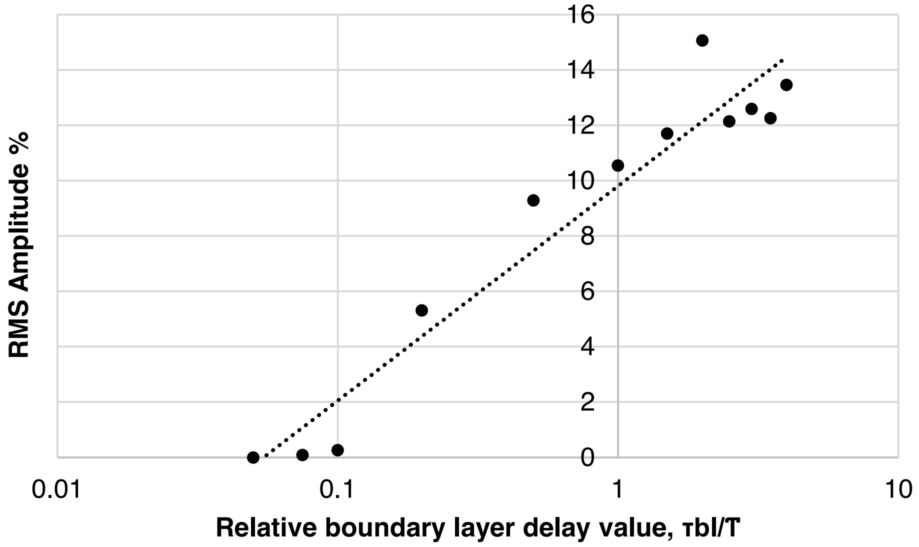

Fig. 5.18.a Dependence of RMS Pressure Amplitude on Boundary Layer Delay

From the trends in the two figures, it is observed that for very small values of boundary layer delay, the system is stable and at some minimum value, the system becomes unstable. The further increase in the boundary layer values seem to have an asymptotic effect on the increase in the amplitude and DC shift magnitudes.

Even if it seems trivial, this result is very useful because it implies that any mechanism that can change the value of the boundary layer delay would directly affect the combustion stability of the system in the trend found previously. For example, it has been shown [5-7] that swirling flow oxidizer injection has a stabilizing effect on hybrid rocket combustion. This can be attributed to the decreased value of boundary layer time scales in swirl flows due to increased diffusion speed.

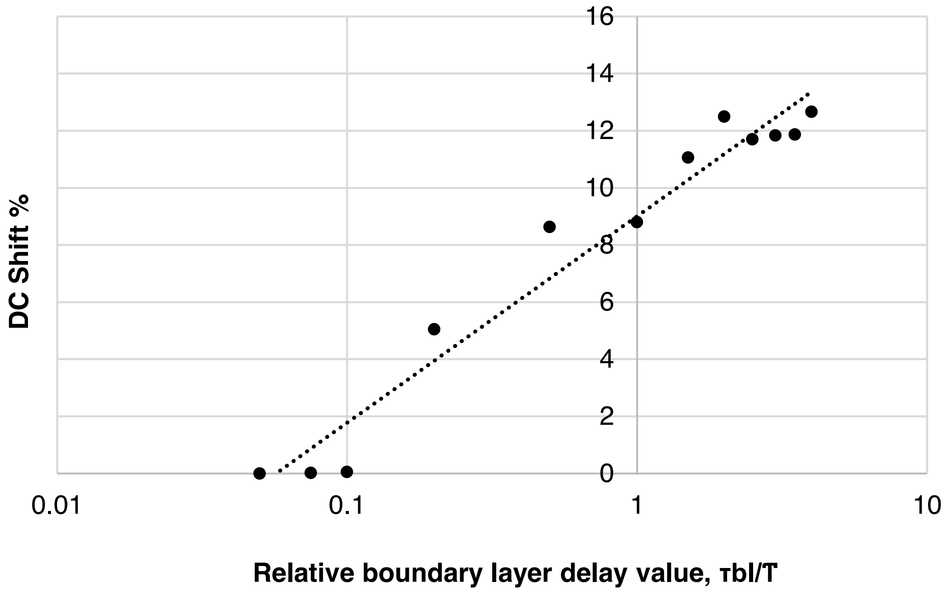

Fig. 5.18.b Dependence of DC Shift on Boundary Layer Delay

5.3.2 Effect of Port Diameter

In our calculations, as noted in Sec. 4.6.2, the port area is fixed throughout the calculation. In order to understand the effect of increase in port diameter, during the run of a rocket motor, here the effect of change in port diameter is considered for the same operational condition (same oxidizer mass flow rate). Fig. 5.19 shows the ND pressure amplitude monitored at the centre of the combustion chamber for different port lengths. It is observed that with increasing port diameter, the amplitude of oscillations increases. This can be easily explained by the fact that with increasing port diameter, the average boundary layer delay increases due to the increased boundary layer thickness. Once again, this result proves the importance of results obtained in the previous section. Any mechanism, change that affects the boundary layer delay values will also affect the stability characteristics of the motor.

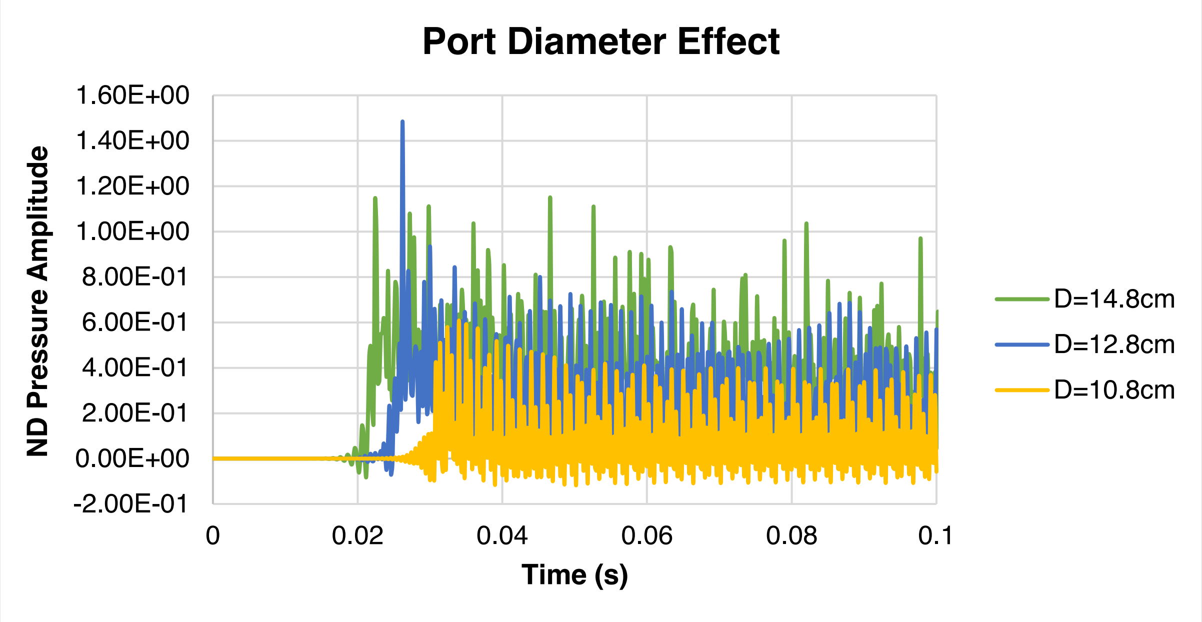

Fig. 5.19 Effect of Port Diameter on the ND Pressure Amplitude

5.3.3 Effect of Power Exponent in Blowing Functional Form

As the next study, the effect of blowing power exponent, k as given in Eqn. 4.3.6 is considered. The equation is written again written below for better understanding. The value of *{q, k}* determine the effect of blowing on the skin coefficient friction and therefore by Reynold's analogy, the convective heat transfer coefficient.

$$\frac{C_f}{C_{f0}} = \frac{C_h}{C_{h0}} = qB_a^{-k}$$

Note that we mentioned that the value of pairs of *{q, k}* is obtained by fitting a power law fit to the original analytical solution of the form Eqn. 3.7. Fig. 5.20 shows the dependence of this choice of pairing for different aerodynamic blowing number B_a. Plotted alongside is the exact analytical form (logarithmic plot) given by Lees. It can clearly be seen that for a same steady state value (represented by a single point in Fig. 5.20), different unsteady characteristics can be obtained with different *q, k* pairings. Therefore, the effect of choice of these pairings for unsteady results needs to be studied.

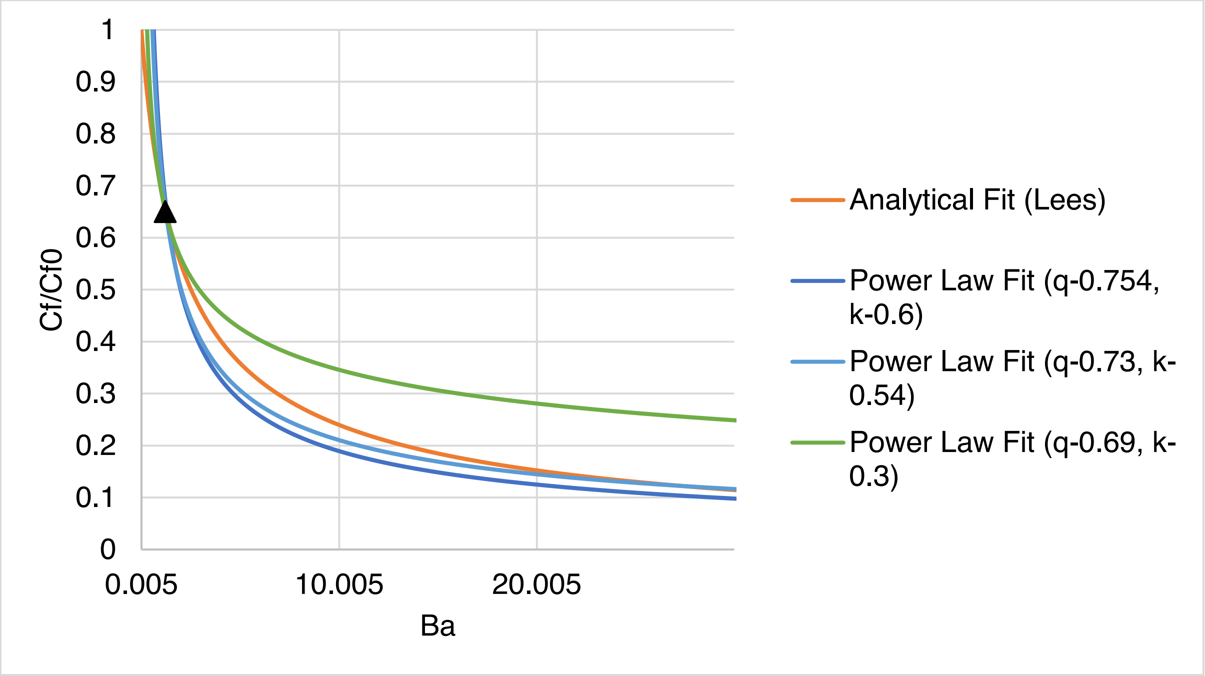

Fig. 5.20 C_f/C_{f0} Dependence on blowing power exponent, k

In order to understand why a change in k can affect the unsteady state, consider the following equation 5.12-5.13. It shows the dependence of change in heat-feedback to changes in regression rate,

$$\delta Q_c = \left(\frac{\partial Q_c}{\partial \dot{r}}\right)\delta r \tag{5.12}$$

Where upon considering a power law functional form for Cf/Cf0 we get,

$$\left(\frac{\partial Q_c}{\partial \dot{r}}\right) = Aq^{-\frac{k}{1-k}}\left(B^{-\frac{k}{1-k}}\ \dot{r}^{\frac{-1-k}{1-k}} - \frac{k}{1-k}\right) \tag{5.13}$$

Upon inspection, Eqn. 5.12 is analogous to the spring mass equation of $F=kx$ where k is a negative quantity. Fig. 5.21 shows the dependence of derivative of convective heat flux on regression rate for different k values. Note that the value of this derivative directly affects the magnitude of negative damping in the system as shown in Eqn. 3.21 and therefore would result in different stability characteristics.

From fig. 5.21, it is observed that the system is very sensitive to the value of the power law exponent k, with higher values of k resulting in higher values of spread.

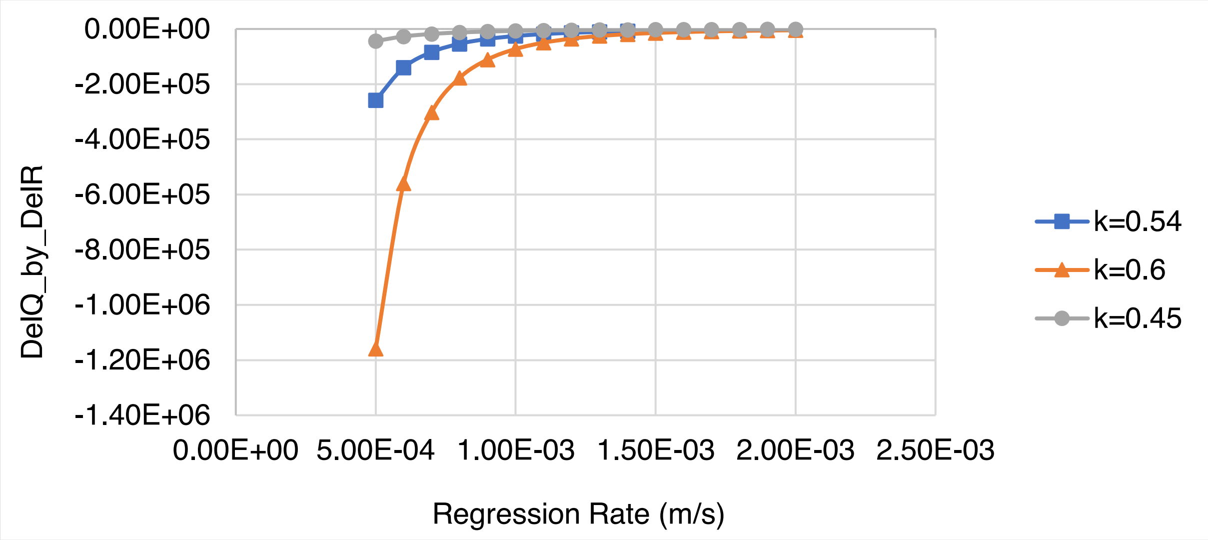

Fig. 5.21 Effect of parameter *k* on the derivative of heat-flux

Numerical results for varying *k,* is shown in Fig. 5.22. It is observed that both the limit cycle amplitude and the DC shift of pressure oscillations are different for different *k* values with increasing *k* values showing increased effects. The rate of growth of oscillations is also increased with increasing values of *k* proving that potentially, the net negative damping is increased for higher values of *k*.

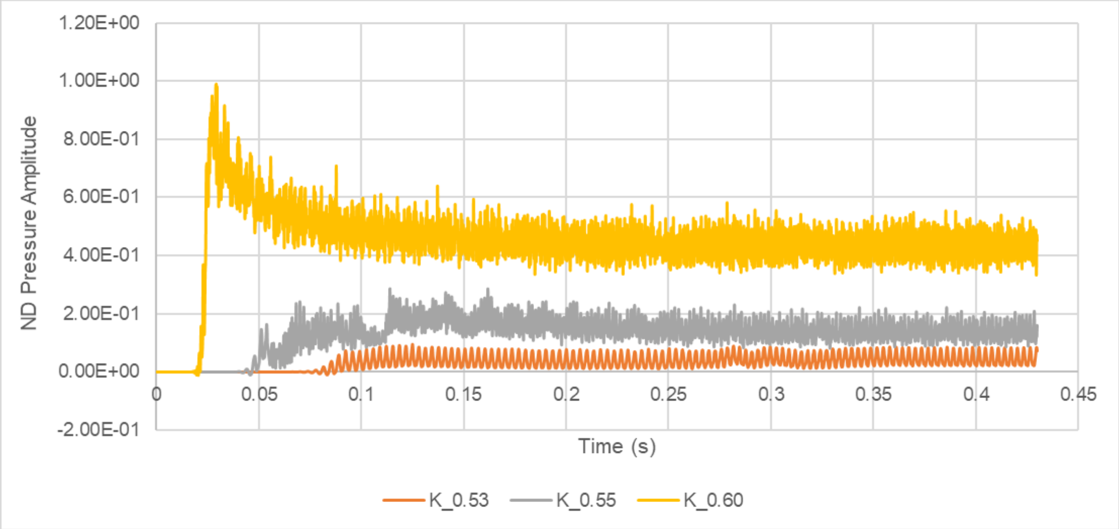

Fig. 5.22 Effect of parameter *k* on the non-linear characteristics

Now, a certain value of *{q, k}* which is physically accurate cannot be known in principle apriori. While, it can be narrowed down based on comparison with experimental data, it renders the prediction capability of the numerical model useless because of its sensitivity. Therefore, it is concluded that using a power law functional form as given in Eqn. 4.3.6 is not good for quantitative comparison of pressure amplitudes with respect to experimental results. Therefore, an improvement is proposed by utilizing the exact analytical functional form (Lees) [5-8] of ratio of skin coefficient frictions as given in Eqn. 3.9 and which is rewritten below as,

$$\frac{C_f}{C_{f0}} = \frac{\ln(1 + B_a)}{B_a}$$

This results in the unsteady convective heat-feedback taking the form as,

$$Q_c(t) = \frac{\dot{r}_{(t-\tau)}\rho_f}{\left(e^{\left(\frac{\dot{r}_{(t-\tau)}\rho_f}{G(t)\frac{C_{f0}}{2}}\right)}\right) - 1} B_t h_v \tag{5.14}$$

Using this modified expression, quantitative comparisons against experimental data for the prediction of pressure amplitude are made.

5.4 Comparison with Experimental Results

The experiments considered are Carmicino's [5-6] lab scale motor firings. Of all the tests, only those are considered where the effect of two dimensional flowfield such as vortex shedding is not dominant as such effects have been claimed to affect the intrinsic combustion instability in hybrids and as such effects cannot be modelled with our existing Q1D model. Additionally, the tests in which no details of the magnitude of pressure amplitude was provided were eliminated. In the experiments, the pressure sensor was mounted in front of the pre-combustion chamber. In our numerical simulation, the pre-combustion chamber and the post combustion chamber are not modelled. Therefore, the measurements at the head end of the motor are taken as the closest to reality and are used for comparisons.

The following is the set of experimental specifications considered,

Table 5.5 Experimental conditions for validation of unsteady analysis

Test Number	Average port internal diameter (mm)	Grain length (mm)	Fuel/Oxidizer	Oxidizer flow rate (kg/s)
11R	52.4	545	HTPB/GOX	0.141
16R	57.8	533	HDPE/GOX	0.118

Since, in our modelling, the change in port area is not considered, the average internal port diameter from the experiment is taken as the initial dimeter in the numerical simulation. For simulations with HTPB fuel, the following are the properties which are taken as given in Table 5.6. Additionally, it is assumed that the pyrolysis product of HTPB fuel is only the monomer 1-3 Butadiene.

Table 5.6. Physical properties of HTPB

Property	**Value**	**Unit**
Thermal conductivity, l_s	0.1506	W/ (m.K)
Density of the solid fuel, ρ_s	920	kg/m^3
Heat of vaporization, h_v	1966.8	kJ/kg
Thermal diffusivity, α_s	1.0×10^{-8}	m^2/s
Activation energy, E_a	203.34	kJ/mole
Pre-exponential factor, A_c	2.63×10^{12}	s^{-1}
Specific heat of the solid, C_p	1631.4	J (kg. K)

The experimental result for the test 11R is as shown in Fig. 5.23. Fig. 5.24 shows the numerical prediction for the same test case. In Fig. 5.23, it is important to note that we can compare only the regime 1st or 3rd with our numerical model as 2nd regime is reported to be as a result of resonance of vortex shedding with the acoustic modes. Due to the limitation of our numerical model in predicting 2-Dimensional flow field effects, such a comparison cannot be made. The author's report that the pressure amplitude in the experiment 11R had a value of 11% in the 1st regime. From Fig. 5.24, it is verified that the numerical result for the same test configuration has a peak to peak amplitude of ~ 11% which is an accurate match with the experiment.

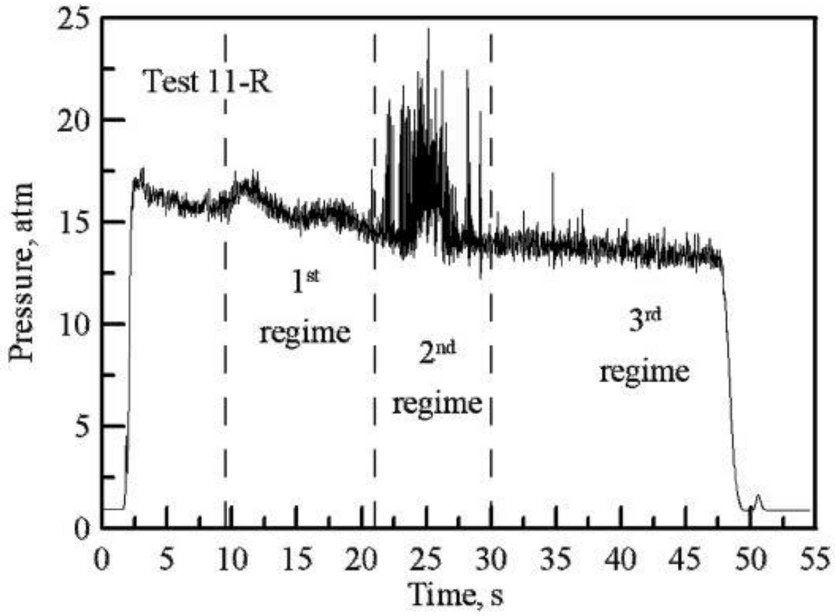

Fig. 5.23 Experimental result of Test 11R [5-6]

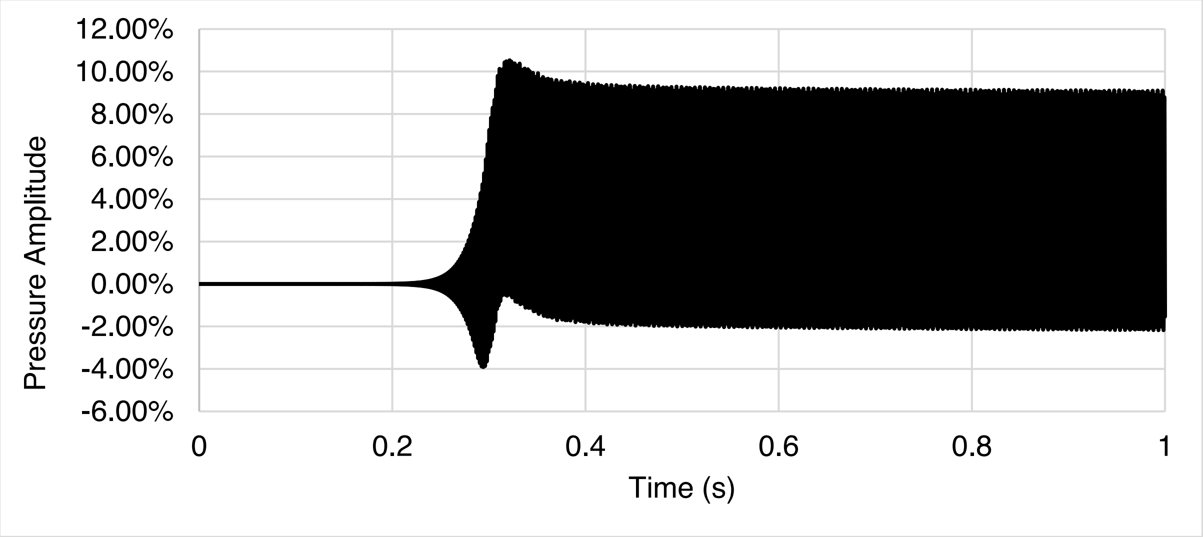

Fig. 5.24 Numerical result for Test 11R

For the next experimental comparison, the experimental condition of Test 16R is numerically simulated. Fig. 5.25 shows the experimental results of Test 16R. Note that no excitation of the combustion instability was reported in Test 16R. This is due to the presence of a diaphragm in the post combustion chamber in the Test 16R setup. This was done to prevent the coupling of vortex shedding and therefore prevent the amplification of combustion instability such as which is seen in the 2nd regime of Test 11R.

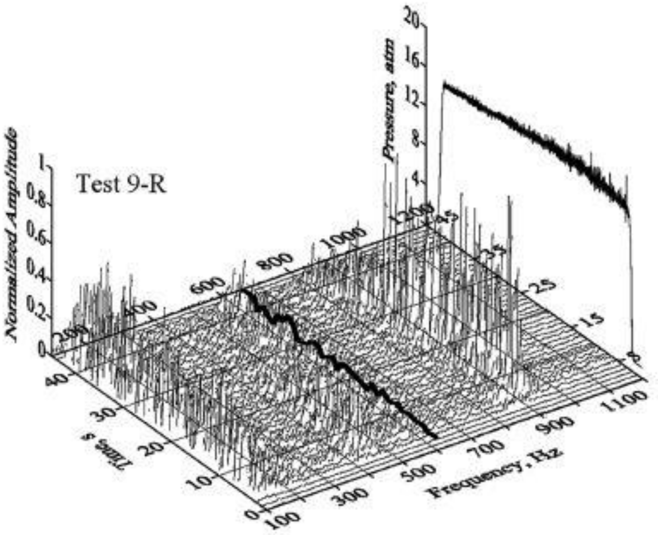

Fig. 5.25 Experimental result of Test 9R [5-6]

The numerical result for Test 9R is shown below in Fig. 5.26. A peak to peak amplitude of 4% is observed in the numerical results. It is less than the 5% limit of pressure amplitude to be called 'combustion instability'. However, since the experiment does not provide the exact value of amplitude, a direct comparison is not made for this case.

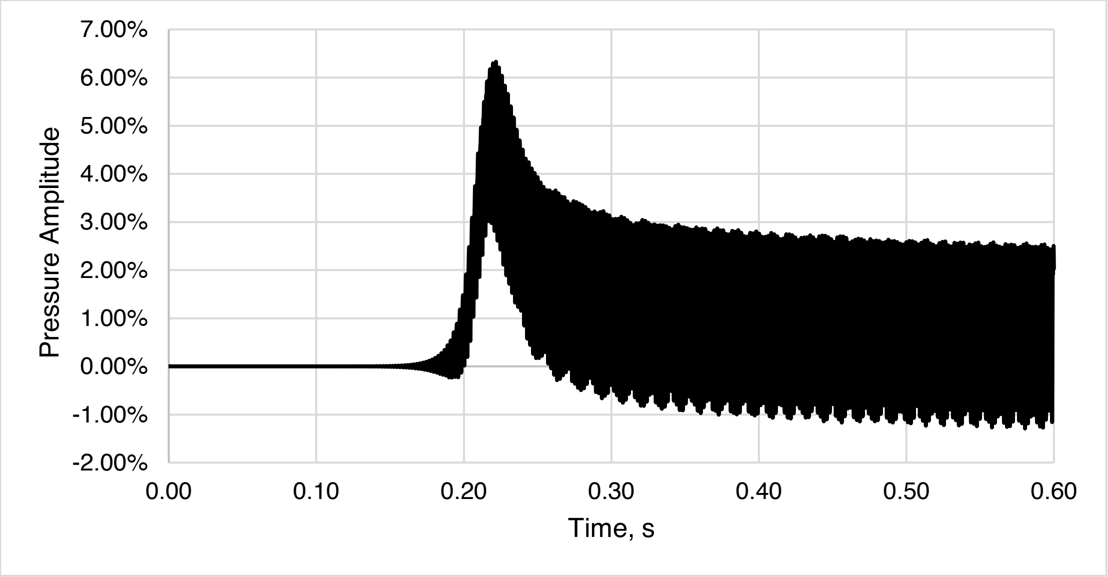

Fig. 5.26 Numerical result of Test 9R

5.5 Conclusion

This chapter summarizes the results obtained with the transient analysis of hybrid rocket combustion using the computational model constructed. It is found that the hybrid rocket combustion modelled is inherently stable in the absence of boundary layer delay. This delay represents the delay experienced by the wall heat flux to the changes in the regression rate due to the delays in the solid fuel thermal conduction. Upon modelling this delay into the unsteady form of convective heat flux, the motor was found to be unstable under all conditions except when the boundary layer delay was negligibly small.

The FFTs of the limit cycle non-dimensionalized pressure amplitude obtained, show that all the natural modes of the system are excited. This is attributed to the negative damping that the system experiences due to the delayed feedback of heat to the regressing solid surface. The FFT of the regression rates also show peaks to that same of the pressure oscillations and this suggests a coupling between the acoustics and the unsteady burning in the combustion chamber. The spatial variation studied shows that multiple higher order acoustic modes are present in the chamber flowfield. The dominant intrinsic hybrid boundary layer mode frequency is found to that corresponding to the spatial average of the boundary layer delays present in the system.

Parametric analyses are conducted by changing the boundary layer delay values. The model can predict the frequency of the primary hybrid oscillation frequency with good accuracy. It is seen that both the RMS amplitude and the magnitude of the DC shift of the limit cycle region increases with increasing boundary layer delay in a logarithmic fashion. However, with increase in the boundary layer delay, there seems to exist, an asymptotic value of amplitude and DC shift. This increase may be attributed to the increased effect of associated negative damping. These results are useful, because they predict that by controlling the boundary layer delay, the characteristic of intrinsic hybrid low-frequency instability can be controlled. For example, it is seen that upon increase in port diameter, the amplitude of pressure oscillations increases.

The limitation of using a power law functional form for the ratio of skin coefficient frictions in the derivation of the unsteady convective heat flux is explained using a sensitivity analysis. An improvement for the same is given and using that experimental comparisons are performed for 2 set of experiment which shows a good match. The novelty of this numerical modelling approach is that by using the unsteady convective heat flux, the details about all the natural modes of the system can be extracted without the necessity of any forcing functions. Within its limitations of Q1D flow field, it is concluded that the model serves as an excellent engineering tool for a motor designer to parametrically study the effect of different motor configurations on the motor stability.

5.6 References for Chapter 5

[5-1] Karabeyoglu, A., Cantwell, B. and Stevens, J., 2005, July. Evaluation of the Homologous Series of Normal Alkanes as Hybrid Rocket Fuels. In 41st AIAA/ASME/SAE/ASEE Joint Propulsion Conference & Exhibit (p. 3908).

[5-2] Marxman, G.A., Wooldridge, C.E. and Muzzy, R.J., 1964. Fundamentals of hybrid boundary-layer combustion. In Progress in Astronautics and Rocketry (Vol. 15, pp. 485-522). Elsevier.

[5-3] Shimada, T., Hanzawa, M., Morita, T., Kato, T., Yoshikawa, T. and Wada, Y., 2008. Stability analysis of solid rocket motor combustion by computational fluid dynamics. AIAA journal, 46(4), pp.947-957.

[5-4] L. Rayleigh. The Explanation of Certain Acoustic Phenomena. Nature, July 18:319–321, 1878.

[5-5] Karabeyoglu, A., 2007. Combustion instability and transient behavior in hybrid rocket motors. Progress in Astronautics and Aeronautics, 218, p.351.

[5-6] Carmicino, C., 2009. Acoustics, vortex shedding, and low-frequency dynamics interaction in an unstable hybrid rocket. Journal of Propulsion and Power, 25(6), pp.1322-1335.

[5-7] Kim, J., Moon, Y.J., Lee, C. and Lee, C., 2017. Transition of Combustion Instability by Swirl Injection in Hybrid Rocket. 7th EUCASS, pp.2017-616.table

[5-8] Lees, L., 1958, March. Convective heat transfer with mass addition and chemical reactions. In *Combustion and Propulsion, Third AGARD Colloquium* (pp. 451-498). Pergamon Press, New York.

CHAPTER – 6

CONCLUSION

6.1 Conclusion of the Thesis

One of the major and long-chronicled problems in hybrids is the combustion instability. This phenomenon which has been widely reported over a wide range of motor specifications is a type of low-frequency non-acoustic combustion instability found to be unique and intrinsic to hybrid rocket motors. The frequency range of the pressure fluctuations is typically on the lower end of the frequency spectrum. Even though the phenomenon of combustion instability in hybrids has been investigated in the past, to our knowledge, till date there is no model that can predict all the characteristics of the instability including the frequency of oscillations, the characteristics of the non-linear region such as limit cycle amplitude and DC shift. It is also not clear under what conditions; a rocket motor is prone to the instability. The aim of this thesis is to try to address these problems and develop a model that can be used by a potential rocket designer to design a rocket motor that is not susceptible to combustion instability.

In Chapter 3, the concept of delayed feedback to a simple oscillator resulting in the formation of the so called 'negative' damping is derived. It is also shown that by adding a simple delay to the feedback of the system, an otherwise stable system can be made unstable. An attempt is made to draw a correlation to the hybrid rocket motor by derivation of the non-linear second order differential equation for the oscillatory regression rate in hybrids. However, the complete derivation is limited by the non-availability of closed forms of solutions for transient problem of thermal conduction on a moving regressing surface. It is concluded that an approached based on numerical modeling of all the actual physics inside the combustion chamber using a computational fluid dynamics is the best approach.

In Chapter 4, the methodology of the construction of the computational model is explained. The model consists of four sub models: 1. Quasi-1D gas dynamics model based on Euler equations, 2. Chemical model using CEA, 3. An analytical heat feedback model and 4. A thermal conduction model inside the solid fuel. This model can simulate all the internal ballistics of the hybrid rocket motor during any transient simulation.

In Chapter 5, validation of the numerical model for the prediction of steady state regression rate is carried out by comparison against existing experimental data. Upon modeling of the boundary layer delay, the modelled rocket motor was found to be unstable. The boundary layer delay represents the delay experienced by the convective heat flux in the boundary layer to the changes in the mass flux and the regression rate. The FFT of the limit cycle amplitude shows peaks corresponding to all the natural modes present in the system, highlighting that all the oscillators present naturally in the system are excited. The frequencies of the regression rate oscillations also show the same peaks as that of the pressure oscillations showing that there is a coupling between the acoustics and the unsteady burning in the combustion chamber of the motor. The effect of finite time needed for the unburnt fuel to move from the regressing surface to the flame region is also additionally modelled as a time delay to the heat of combustion. It is seen that this modelling has the effect like an external forcing of the system resulting in increased DC shift and amplitude of oscillations.

Parametric studies with different boundary layer delays showcased that with increasing delay values, the system is found to be more unstable. However, there exists a minimum delay value for the system below which, the system is always stable. This is very important to understand because if a hybrid rocket can be modelled incorporating any process that can reduce this boundary layer delay (for e.g. swirling oxidizer injection) can result in a stable motor.

This research is the first of its kind to investigate the intrinsic combustion instabilities using computational fluid dynamics in hybrid rocket motors. Through our results, it is possible to explain the phenomenon of instabilities due to negative damping present in the system due to delayed feedback of heat flux from the flame to changes in the oxidizer mass flux and the regression rates. The computational model developed can successfully capture both the linear and the non-linear characteristics of the phenomenon.

The novelty of this numerical modelling approach is that by using the proposed unsteady convective heat flux, the normal unsteady characteristics of the combustion as seen in experiments such as limit cycle amplitudes can be obtained. Also, the details about all the natural modes of the system can be extracted without the necessity of any external forcing. Therefore, the numerical model serves as a powerful tool to model and study the unsteady combustion in hybrid rocket motors. Within its limitations of Q1D flow field, the model additionally serves as an excellent engineering tool for a motor designer to parametrically study the effect of different motor configurations on the motor stability characteristics and to potentially design motors not susceptible to this intrinsic phenomenon.

6.2 Future Extensions of Work

In Chapter 3, it is highlighted that the derivation of the oscillatory regression rate equation is not completed due to the unavailability of a model that can accurately describe the unsteady transient characteristic of the thermal gradient at the solid surface. However, this problem can be tackled by application of the Z-N theory used in solid rocket combustion stability research.

In Chapter 4, during the numerical modelling of the solid fuel, the melt layer is infinitely thin as the first order of approximation. However, modelling the melt layer explicitly along with modelling of the solid kinetics processes and the associated characteristic time such as time for fuel degradation would be an excellent addition to this research.

In Chapter 5, during the modeling of the boundary layer delay along the port length, it is assumed that the delay values do not change temporally. However, this is not the case and the temporal evolution of boundary layer delay should also be considered for a higher order approximation of the effect.

THE END